Fluorescence fluctuation-based analysis of the amyloid-β monomer

Inaugural-Dissertation

zur Erlangung des Doktorgrades
der Mathematisch-Naturwissenschaftlichen Fakultät
der Heinrich-Heine-Universität Düsseldorf

vorgelegt von

Mario Schneider

aus Mönchengladbach

Düsseldorf, Dezember 2015

aus dem Institut für Physikalische Biologie
der Heinrich-Heine-Universität Düsseldorf

Gedruckt mit der Genehmigung der
Mathematisch-Naturwissenschaftlichen Fakultät der
Heinrich-Heine-Universität Düsseldorf

Referent: Prof. Dr. Dieter Willbold
Koreferent: Prof. Dr. Jörg Fitter
Tag der mündlichen Prüfung: 09.02.2016

Dedicated to my wife Sarah and my son Felix.

Contents

1 Introduction **1**

2 Theory **3**

2.1 Fluorescence 4
2.1.1 Fundamentals of fluorescence 4
2.1.2 Fluorescence lifetime 5
2.1.3 Fluorescence anisotropy 6
2.1.4 Fluorescence fluctuation spectroscopy 9
2.2 Accessible volume simulation 26
2.3 Bayesian data analysis 27
2.3.1 Bayesian model inference 27
2.3.2 Laplace approximation of the evidence 28
2.4 Biochemical principles 30
2.4.1 Alzheimer's disease 30
2.4.2 Amyloid-β peptide 30
2.4.3 Protein denaturation 32
2.4.4 Two-state unfolding of proteins 33

3 Materials **36**

3.1 Buffers 37
3.2 Chemicals 37
3.3 Instruments 38
3.4 Software 38

4 Methods **40**

4.1 Recombinant expression of an $A\beta_{42}$ cysteine variant 41
4.1.1 The expression system 41
4.1.2 Choosing an appropriate cysteine mutation site 42
4.1.3 $C(0)A\beta_{42}$ purification using chromatographic methods 42
4.2 Dye labeling of $C(0)A\beta_{42}$ with Alexa Fluor 488 45
4.3 Viscosity and density measurements 47
4.4 Time-resolved fluorescence measurements 49
4.5 Atomic force microscopy measurements 49
4.6 1fFCS unfolding measurements 50
4.7 2fFCS unfolding measurements 51
4.8 Simulation of single-molecule fluorescence experiments 53
4.9 Development of a Bayesian burst identification method 57
4.9.1 Likelihood function for microtimes 58
4.9.2 Likelihood function for interphoton times 59

4.9.3 Performance evaluation 63

5 Bayesian burst identification 65
5.1 Reliability of the simulations 66
5.1.1 Influence of the simulation box size 66
5.1.2 Comparison of simulation and experiment 67
5.2 Performance of the Bayesian burst identification method 68
5.2.1 Analysis of simulated data 68
5.2.2 Analysis of experimental data 69

6 Aβ_{42} monomer unfolding 73
6.1 Characterisation of AF488-C(0)Aβ_{42} 74
6.1.1 Aggregation propensity 74
6.1.2 Behaviour of the fluorescent dye bound to C(0)Aβ_{42} 75
6.2 Adsorption artifacts in FFS 81
6.3 Refractive index mismatch in 1fFCS measurements 83
6.4 Aβ_{42} is monomeric under FCS measurement conditions 87
6.5 AF488-C(0)Aβ_{42} monomer unfolding with GdnHCl 88

7 Conclusion and outlook 94
7.1 Aβ_{42} monomer unfolding 94
7.2 Bayesian burst identification 95

8 Summary 96

9 Zusammenfassung 98

10 Danksagung 100

Bibliography 102

A Appendix 108

1

Introduction

About 46 million people worldwide suffer from dementia [1]. About two-third of them suffer from Alzheimer's disease (AD) [2]. AD is a neurodegenerative disease whose progression is accompanied by several symptoms including loss of memory, loss of language capability or loss of motor skills. This can mainly be attributed to the degradation of brain material. The exact mechanism of the development of AD still has to be explored. Nowadays, it is widely accepted that the amyloid beta peptide (Aβ) is the main actor in the formation of AD. Aβ is a cleavage product of the amyloid precursor protein. Depending on the exact cleavage site, different isoforms evolve. In this work, we studied $A\beta_{42}$, an isoform with 42 amino acids. Due to their toxicity, research has mainly focused on aggregates of the $A\beta_{42}$ and correspondingly there is only little known about $A\beta_{42}$ monomers. This can mainly be attributed to the high aggregation propensity of the $A\beta_{42}$ monomer which also makes studies on monomers challenging. Common techniques like NMR or X-ray diffraction usually fail to elucidate the monomer structure in purely aqueous solution. Structural information of monomeric $A\beta_{42}$ is only obtainable in pure hexafluoroisopropanol [3] or in aqueous solutions of hexafluoroisopropanol [4] or trifluoroethanol [5]. However, these conditions are far from being physiological. It is suggested that Aβ monomers might exist in different conformations [6] and that they adopt β-sheet conformation prior to aggregation [7]. However, there is no substantial experimental evidence due to the previously stated difficulties in working with Aβ. Understanding possible structural conversions of Aβ monomers is of high importance since it might help to elucidate structural elements which make the monomer more prone to aggregation and thus more prone to form (toxic) oligomers.
In this work, we implement and apply fluorescence fluctuation spectroscopy (FFS), especially fluorescence correlation spectroscopy (FCS), in order to get insights into unfolding mechanisms of monomeric $A\beta_{42}$. FFS is well-suited to study $A\beta_{42}$ monomers since measurements are typically performed at nanomolar concentrations. These concentrations not only favour Aβ monomers, but are close to *in vivo* concentrations of Aβ [8].

In addition, a new and improved method for fluorescence burst identification will be presented. Fluorescence bursts arise in single-molecule fluorescence (sm fluorescence) measurements when a single fluorescent molecule traverses a tiny observation volume

of high laser intensity and subsequently emits bunches of photons. This occurs manifold in a sm fluorescence experiment. Usually, a subsequent burst selection is intended to extract those data subsets that belong to fluorescence counts and to reject background counts. Analysis of fluorescence bursts can give valuable insights on heterogeneities and dynamics of fluorescently labeled proteins or nucleic acids [9]. Several burst identification procedures are described in the literature [10–15]. However, most of them perform the burst identification on intensity information, and in part with a questionable threshold on the intensity trace. Only recently a burst identification method was published based on fluorescence lifetime information [15, 16] and applying Bayesian data analysis. Nevertheless, in this work the idea of Bayesian burst identification will be extended in a sense of using both types of information, intensity and lifetime information.

2

Theory

Contents

2.1 Fluorescence 4

2.1.1 Fundamentals of fluorescence 4

2.1.2 Fluorescence lifetime 5

2.1.3 Fluorescence anisotropy 6

2.1.4 Fluorescence fluctuation spectroscopy 9

2.2 Accessible volume simulation 26

2.3 Bayesian data analysis 27

2.3.1 Bayesian model inference 27

2.3.2 Laplace approximation of the evidence 28

2.4 Biochemical principles 30

2.4.1 Alzheimer's disease 30

2.4.2 Amyloid-β peptide 30

2.4.3 Protein denaturation 32

2.4.4 Two-state unfolding of proteins 33

2.1 Fluorescence

2.1.1 Fundamentals of fluorescence

When a molecule absorbs a photon of wavelength λ_{abs}, it is excited from its electronic ground state S_0 to a higher excited state $S_1, \ldots, S_n$. The energy difference ΔE between these states, and thus the energy of the preceding photon, is related to the wavelength by the following equation:

$$\Delta E = \frac{hc}{\lambda} \tag{2.1}$$

Herein h is the Planck constant and c denotes the speed of light. The molecule rapidly looses energy through internal conversion (within picoseconds) and finally ends up in the first-excited state S_1. From here the energy can either further dissipate through internal conversion (IC), intersystem-crossing (ISC) or through emission of a photon with wavelength λ_{em}. This is referred to as fluorescence emission. Compared to the wavelength of excitation λ_{exc}, λ_{em} is usually shifted towards higher wavelengths $\Delta\lambda = \lambda_{\text{em}} - \lambda_{\text{exc}} > 0$ (Stokes-shift, see figure 2.1 A). Resting times in the triplet state are usually on the order of microseconds, making the molecule unavailable for re-excitation during that time.
An important parameter in this context is the fluorescence quantum yield (ϕ_F). It corresponds to the probability of receiving a fluorescence photon given an excitation has occurred. It is defined in the following way:

$$\phi_F = \frac{\#\text{ of emitted photons}}{\#\text{ of absorbed photons}} = \frac{k_F}{k_F + k_{ISC} + k_{IC}} \tag{2.2}$$

Herein k_F, k_{ISC} and k_{IC} denote the transition rates in the Jablonski scheme (figure 2.1 B). ϕ_F is a very important parameter when selecting a dye for fluorescence applications. For excellent dyes, the quantum yield often exceeds 90 %. In equation 2.2 the factor $\tau_F = \frac{1}{k_F + k_{isc} + k_{ic}}$ is known as the fluorescence lifetime. It can be interpreted as the average time an experimenter has to wait to receive a fluorescence photon after the molecule has been excited. More about fluorescence lifetime is presented in section 2.1.2.

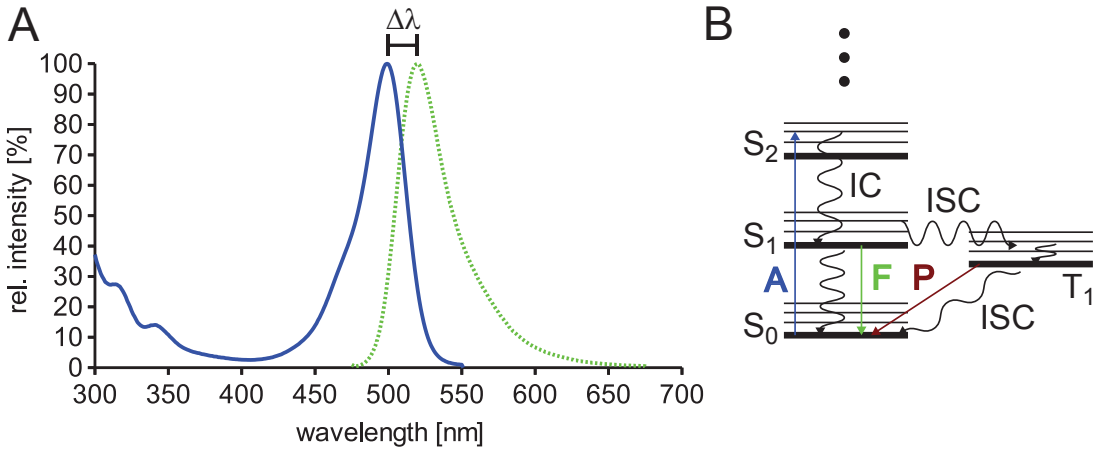

Figure 2.1: (**A**) Excitation (blue line) and emission spectrum (green dotted line) of Alexa Fluor 488. Generally, the emission maximum is shifted towards higher wavelength compared to the excitation maximum (Stokes shift). (**B**) Jablonski diagram showing possible transitions from excited singlet states (S_1 to S_n) to the singlet ground state (S_0). The thick lines denote the electronic energy levels of the molecule. The thinner ones denote vibrational levels. The molecule absorbs (blue arrow, A) a photon of an appropriate wavelength and transits to an excited singlet state. Through internal conversion (IC) it relaxes quickly to the first excited singlet state. Furthermore, it can occupy a triplet state T_1 through intersystem crossing (ISC) or loose the energy via internal conversion or fluorescence (green arrow, F). If the molecule is in the triplet state, it can relax to the ground state via ISC or via emitting a phosphorescence photon (red arrow, P).

2.1.2 Fluorescence lifetime

For the moment, it will be assumed that an ensemble of fluorescent molecules of type A is excited by an infinitely short pulse of light. At time zero A_0^* denotes the number of molecules which are excited. To derive a general expression for the number of excited molecules at time t we have to solve the differential equation:

$$\frac{dA^*(t)}{dt} = -\left(k_F + k_{isc} + k_{ic}\right) A^*(t) \tag{2.3}$$

By integration one obtains:

$$\begin{aligned} A^*(t) =& A_0^* \exp\left(-\left(k_F + k_{isc} + k_{ic}\right) t\right) \\ =& A_0^* \exp\left(-\frac{t}{\tau_F}\right) \end{aligned} \tag{2.4}$$

$\tau_F = \frac{1}{k_F+k_{isc}+k_{ic}}$ is the lifetime of the excited state. It is not to be confused with the so-called natural lifetime $\tau_N = \frac{1}{k_F}$. It can theoretically be calculated by the Strickler-Berg relation [17]. In order to transform equation 2.4 into an intensity $I^*(t)$, it is multiplied by the rate at which fluorescence emission occurs, namely k_F. As a result, the following equation is obtained:

$$I^*(t) = k_F A_0^* \exp\left(-\frac{t}{\tau_F}\right) \tag{2.5}$$

The proportionality factor depends on experimental conditions such as detection efficiency, collection efficiency, etc. Gathering these parameters in a factor I_0, equation 2.5 can be written as:

$$I(t) = I_0 \exp\left(-\frac{t}{\tau_F}\right) \tag{2.6}$$

Equation 2.6 is an example of a monoexponential fluorescence lifetime decay model. Very often the fluorescence decay has to be described by multiexponential decays. This is especially true for protein bound fluorophores. Thus, equation 2.6 can be generalised to:

$$I(t) = \sum_{i=1}^{M} a_i \exp\left(-\frac{t}{\tau_{F,i}}\right) \quad \text{with} \sum_{i=1}^{M} a_i = 1 \tag{2.7}$$

Since the laser pulse has a finite width and the detection system has a temporal jitter, the final decay model (2.7) needs to be convolved by the instrument response function (IRF). This leads to the following equation:

$$I(t) = \mathrm{IRF}(t) \otimes \sum_{i=1}^{M} a_i \exp\left(-\frac{t}{\tau_{F,i}}\right) \quad \text{with} \sum_{i=1}^{M} a_i = 1 \tag{2.8}$$

Equation 2.8 is a general model function which is fitted to an experimental intensity decay by a maximum-likelihood estimator (MLE) or a nonlinear least-square procedure. For low photon counts, the MLE gives more reliable lifetime estimates [18].

2.1.3 Fluorescence anisotropy

Fluorescence anisotropy measurements analyse polarised emission light from fluorescent molecules. The orientation of the emission is defined relative to the orientation of the polarised excitation light. $I_\parallel$ and $I_\perp$ denote emission intensities which are parallel and

perpendicular to the polarisation of the incoming light, respectively. The definition of fluorescence anisotropy r is given as follows:

$$r = \frac{I_{\parallel} - I_{\perp}}{I_{\parallel} + 2I_{\perp}} \tag{2.9}$$

The probability that a fluorophore absorbs (polarised) light depends on the orientation of its absorption transition moment relative to the direction of the electrical field vector of the excitation light (say both enclose an angle θ). If both vectors are colinear ($\theta = 0$), the absorption probability is at a maximum. However, if both vectors are oriented perpendicularly to each other ($\theta = \pi/2$), the absorption probability drops to zero. In general, there are many fluorophores randomly distributed in an isotropic solution. Thus, there is a distribution of excited fluorophores which is equal to [19]:

$$p(\theta) = \cos^2(\theta)\sin(\theta) \tag{2.10}$$

Herein θ denotes the angle between the absorption transition moment and the z-axis, which is the axis of the incident (polarised) excitation light. This mechanism is called photoselection. From simple considerations (see e.g. [17]) one can also derive an expression for $I_{\parallel}$ and $I_{\perp}$ in terms of θ:

$$I_{\parallel} = \int_0^{\pi/2} p(\theta)\cos^2(\theta)d\theta \tag{2.11}$$

and

$$I_{\perp} = \frac{1}{2}\int_0^{\pi/2} p(\theta)\sin^2(\theta)d\theta \tag{2.12}$$

Substituting equation 2.10 into the latter two equations returns:

$$I_{\parallel} = \int_0^{\pi/2} p(\theta)\cos^2(\theta)d\theta = \frac{1}{5} \tag{2.13}$$

and

$$I_{\perp} = \frac{1}{2}\int_0^{\pi/2} p(\theta)\sin^2(\theta)d\theta = \frac{1}{15} \tag{2.14}$$

Using these equations in the equation for the definition of the fluorescence anisotropy (equation 2.9), finally yields the following equation:

$$r = \frac{2}{5} = 0.4 \tag{2.15}$$

Equations 2.11 to 2.15 are only valid in case of a parallel absorption and emission moment. If this condition is not fulfilled and the transition moments enclose an angle α, then the anisotropy has to be corrected for this effect (see equation 2.16).

$$r = \frac{2}{5}\left[\frac{3\cos^2(\alpha) - 1}{2}\right] \tag{2.16}$$

r in equation 2.16 is often referred to as fundamental anisotropy. However, in the following I will use r_0 instead of r to denote the fudamental anisotropy. For many dyes α is quite close 0 and thus their r_0 close to 0.4. r_0 can, for example, be determined in highly viscous solutions at low temperatures, where rotational motion is negligible. Rotation and other processes can lead to fluorescence depolarisation. To follow these processes, time-resolved fluorescence anisotropy $r = r(t)$ measurements can be applied. In order to obtain the anisotropy decay $r(t)$, the intensity decays for the parallel $I_\parallel(t)$ and perpendicular $I_\perp(t)$ polarisation are needed. In general, these decays are multi-exponential due to an "overlay" of the fluorescence lifetime decay $I(t)$, with the fluorescence anisotropy decay $r(t)$ (equation 2.17 and 2.18).

$$I_\parallel(t) = \frac{1}{3}I(t)\left[1 + 2r(t)\right] \tag{2.17}$$

$$I_\perp(t) = \frac{1}{3}I(t)\left[1 - r(t)\right] \tag{2.18}$$

$I(t)$ and $r(t)$ themselves might be multiexponential (see section 2.1.2 for $I(t)$). Applying equations 2.17 and 2.18 we can redefine the anisotropy equation 2.9:

$$r(t) = \frac{I_\parallel(t) - I_\perp(t)}{I_\parallel(t) + 2I_\perp(t)} \tag{2.19}$$

Generally, $r(t)$ is assumed to be multiexponential:

$$r(t) = r_0 \sum_{i=1}^{M} a_i \exp\left(-\frac{t}{\rho_i}\right) \quad \text{with} \sum_{i=1}^{M} a_i = 1 \tag{2.20}$$

where ρ_i denotes a rotational correlation time and a_i the amplitude of the exponential term. Usually, there are several ways of how to analyse experimental time-resolved fluorescence anisotropy data:

1. The experimental decay $r(t)$ is calculated from the measured decays $I_{\parallel}(t)$ and $I_{\perp}(t)$ via equation 2.9 and is fitted to the model in equation 2.20.
2. Measured decays $I_{\parallel}(t)$ and $I_{\perp}(t)$ are fitted in a global manner.
3. The experimental sum and the difference in equation 2.19 are fitted in a global manner.

Option 3 was used to obtain the rotational correlation times and amplitudes of the anisotropy decays in this work.

2.1.4 Fluorescence fluctuation spectroscopy

In fluorescence fluctuation spectroscopy (FFS), fluorescent particles diffuse in and out of a tiny observation volume (on the order of 1 fl) which gives rise to fluctuations in the fluorescence signal (see figure 2.2).

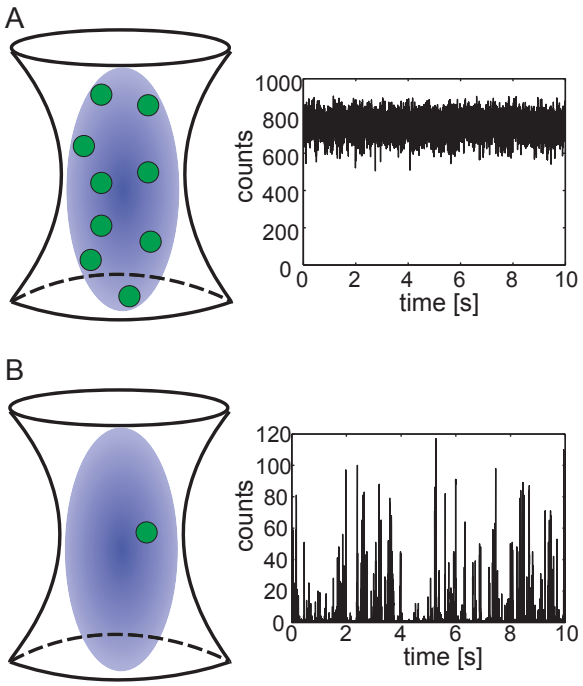

Figure 2.2: Fluorescent particles traverse the observation volume and give rise to fluorescence intensity fluctuations. A big number of particles in the observation volume gives rise to low intensity fluctuation amplitudes (**A**). A small number of molecules in the observation gives rise to high intensity fluctuation amplitudes (**B**).

A prerequisite for FFS is to have a concentration of fluorescent particles which is low enough to observe the fluctuations in the fluorescence intensity signal. If concentrations are too high the relative change of fluorescence intensity (fluctuation amplitude) is marginal. However, in the concentration regime in which only single molecules traverse the observation volume, the fluctuation amplitudes reach maximum values. Typical concentrations for FFS experiments are in the lower nanomolar range. Bright particles give rise to many photons during a transit while dim particles only emit a few photons. Thus, the fluorescence intensity signal contains information about the concentration, diffusion and photophysical properties of the fluorescent particles. In the following sections, a few methods will be described which are able to extract this information from the fluorescence intensity signal and which were applied in this work.

2.1.4.1 Number and brightness analysis

To understand the basic idea behind the number and brightness (N&B) analysis method we take a closer look at figure 2.3. The left-hand side of (A) and (B) shows two kinds of particles of different brightness. There are many dim particles in (A) and few bright particles in (B). As can be seen on the right-hand side, the average intensity is the same in both cases. However, the fluctuation amplitudes (deviation from the average intensity) differ. The bigger fluctuation amplitudes in (B) can, to some extent, be attributed to the much higher particle number fluctuations. The magnitude of fluctuations can be described by the variance σ^2 of the intensity trace I:

$$\begin{aligned} \sigma^2 &= \frac{\sum_i \left(I_i - \langle I \rangle\right)^2}{M} \\ &= \frac{\sum_i \left(\delta I_i\right)^2}{M} \\ &= \langle \delta I_i \cdot \delta I_i \rangle \end{aligned} \tag{2.21}$$

Herein M denotes the total number of bins in the intensity trace. The last row of equation 2.21 plays a key role in fluorescence correlation spectroscopy (see section 2.1.4.3, especially equations 2.56 and 2.57 [1]). With these equations in mind and some futher algebra, it can be shown that:

$$\sigma^2 = \frac{\langle I \rangle^2}{N} \tag{2.22}$$

where N and $\langle I \rangle$ denote the average number of molecules in the observation volume

[1] Therein I_i is denoted with $I(t)$; equation 2.21 is a special case of equation 2.57 for $\tau = 0$

and average intensity, respectively. The average intensity itself is a function of the average number of molecules and their brightness Q, i.e. the number of photons per molecule for a given time interval.

$$\begin{aligned} \langle I \rangle &= \frac{\sum\limits_i I_i}{M} \\ &= QN \end{aligned} \tag{2.23}$$

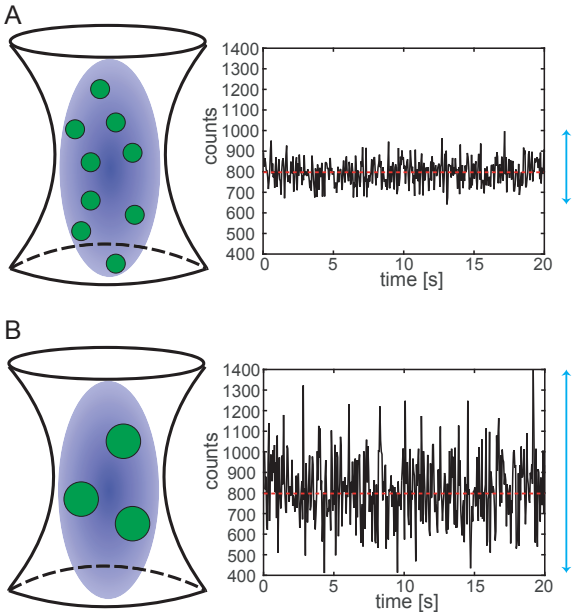

Figure 2.3: Many dim molecules present in the observation volume lead to tiny fluctuation amplitudes around the average intensity (--) (**A**). A few bright molecules present in the observation volume lead to big fluctuation amplitudes (B). Although the average intensity is the same in both cases, the distribution of fluctuation amplitudes (↕) is much bigger in (**B**). The N&B method uses the information about the average intensity and the variance in the fluctuation amplitudes to extract the number and brightness of molecules present in the observation volume.

Thus, calculating the first ($\langle I \rangle$) and second moment (σ^2) of an intensity trace gives information about the average number of molecules in the observation volume and their brightness:

$$N = \frac{\langle I \rangle^2}{\sigma^2} \qquad\qquad Q = \frac{\sigma^2}{\langle I \rangle} \tag{2.24}$$

Accounting for detector shot noise and background

Not only particle number fluctuations but also detector shot noise contributes to the overall variance σ^2. If it is assumed that the number of photon counts at the detector is Poissonian distributed, then the variance σ^2_{det} contributed by the detector is given by:

$$\sigma^2_{det} = \langle I \rangle = QN \tag{2.25}$$

This is due to the fact that the variance is equal to the mean for a Poissonian distribution. Thus, we end up with the following expression for the overall variance σ^2:

$$\begin{aligned} \sigma^2 &= \sigma^2_D + \sigma^2_{det} \\ &= (Q+1)\langle I \rangle \end{aligned} \tag{2.26}$$

where σ^2_D is the variance due to particle number fluctuations. Using equation 2.26 we can correct N and Q from equation 2.24 [20]:

$$N = \frac{\langle I \rangle^2}{\sigma^2 - \langle I \rangle} \qquad Q = \frac{\sigma^2 - \langle I \rangle}{\langle I \rangle} \tag{2.27}$$

To correct for background contributions (e.g. dark counts, scatter or fluorescence) whose mean intensity is given by $\langle I_{Bg} \rangle$, $\langle I \rangle$ can be rewritten (see equation 2.28, and reference [21])

$$N = \frac{\left(\langle I \rangle - \langle I_{Bg} \rangle\right)^2}{\sigma^2 - \langle I \rangle} \qquad Q = \frac{\sigma^2 - \langle I \rangle}{\langle I \rangle - \langle I_{Bg} \rangle} \tag{2.28}$$

In general Q is normalised onto the bin-time T, which is used to generate the intensity trace:

$$\varepsilon = \frac{Q}{T} \tag{2.29}$$

ε is often referred to as the molecular brightness. It plays a key role in photon counting histogram analysis (see section 2.1.4.2).

Bin-time correction

Generally, neither N nor ε is independent of the bin-time T. As the bin-time increases, N increases and ε decreases. In order to correct for this binning effect, a binning function $B_2(T)$ is given as follows [22]:

$$B_2(T) = 2\int_0^T G(\widehat{\tau})(T-\widehat{\tau})d\widehat{\tau} \tag{2.30}$$

Herein $\widehat{\tau} = \tau/\tau_{\text{diff}}$ denotes the scaled correlation time and $G(\widehat{\tau})$ denotes the correlation function (see e.g. equation 2.65). To obtain bin-time independent parameter estimates, one finally has to multiply (divide) N (ε) with (by) the bin-time correction factor. The same applies to N and ε estimates from photon counting histogram analysis (section 2.1.4.2).

2.1.4.2 Photon Counting Histogram (PCH)

Assume a fluorescent particle is immobilised at a position r_1. In this case, the detector only receives photons from this position. Under the assumption that photophysical processes (e.g. excitation and emission cycles) are much faster than the time between two different photons, the emitted intensity is constant $I(t) = \overline{W}$. Then the number of photon counts k for a given sampling interval T at the detector follows a Poisson distribution:

$$p(k) = \text{Poi}(k, \overline{W}) = \frac{\left(\eta_D \overline{W}\right)^k \exp\left(-\eta_D \overline{W}\right)}{k!} \tag{2.31}$$

Herein η_D denotes the detection efficiency of the detector. In case the fluorescent particles are not immobilised, the intensity at the detector is not constant. It rather fluctuates due to Brownian motion [2]. This leads to an additional broadening of the resulting distribution (super-Poissonian). The corresponding equation was given by Mandel [23]:

$$p(k) = \int_0^\infty \text{Poi}(k, I(t))p(I(t))dI(t) = \int_0^\infty \frac{(\eta_D I(t))^k \exp\left(-\eta_D I(t)\right)}{k!} p(I(t))dI(t) \tag{2.32}$$

[2] PCH measurements are usually performed with low laser intensity to avoid triplet processes since these are another source of fluctuations

The explicit dependence of $p(k)$ on the sampling interval T is skipped here but has to be kept in mind. In case T approaches infinity, the fluctuations average out ($p(I(t)) \rightarrow \delta(W - \overline{W})$ and the resulting distribution $p(k)$ becomes a Poisson distribution (see equation 2.31). Thus, T has to be chosen short enough to track the intensity fluctuations. However, if T is too short, the PCH becomes count limited and reliable parameter estimates cannot be obtained.
In the following, it will be shown how to relate Mandel's formula to the average number of molecules in the observation volume and brightness. A particles' fluorescence intensity, reaching the detector, is proportional to the laser excitation profile. For one-photon excitation this can be approximated by a three-dimensional Gaussian:

$$\mathrm{PSF(r)} = \frac{I(x,y,z)}{I_0} = \exp\left(-2\frac{x^2+y^2}{\omega_{xy}^2} - 2\frac{z^2}{\omega_z^2}\right) \tag{2.33}$$

Equation 2.33 is the so-called point spread function, i.e. the (normalised) laser intensity profile. ω_{xy} and ω_z denote a lateral and axial radius of the laser beam, respectively. The fluorescence intensity $I(t)$ reaching the detector is proportional to the excitation intensity:

$$I(t) = \varepsilon \mathrm{PSF}(r) \tag{2.34}$$

The proportionality constant ε denotes the brightness of the molecule. It is proportional to the excitation intensity I_0 at the center of the PSF:

$$\varepsilon = I_0 \Phi \tag{2.35}$$

where Φ is a parameter incorporating the excitation probability of the molecule, its fluorescence quantum yield and instrument-related parameters such as the quantum yield of the detector (η_D, see equation 2.31 and 2.32). Mathematically, equation 2.34 is the transformation of a random variable r, which creates a new random variable $I(t)$. The function performing this transformation is given on the right-hand side. To obtain the probability distribution function (pdf) of $I(T)$ ($p(I(t))$) one can make use of the transformation property of random variables. Generally, if two random variables X and Y are connected via a transformation $Y = T(X)$ and the pdf of X is $p_X(x)$, it can be shown that the pdf of Y, $p_Y(y)$, can be obtained as [24]:

$$p_Y(y) = \int p_X(x)\delta(T(x) - y)dx \tag{2.36}$$

If we identify y with $I(t)$, x with r and $T(x)$ with $\varepsilon \mathrm{PSF}(r)$, then we can rewrite equation 2.36:

$$p(I(t)) = \int p(r)\delta(\varepsilon \mathrm{PSF}(r) - I(t))dr \tag{2.37}$$

$p(r)$ is the probability to find the molecule at a position r. If the molecule is confined within some volume V, the probability to find the molecule at a specific position is equal to $p(r) = \frac{1}{V}$. Using the $p(I(t))$ of equation 2.37 in Mandel's formula (equation 2.32) we obtain:

$$\begin{aligned} p(k|\varepsilon) &= \frac{1}{V}\int_0^\infty \frac{(I(t))^k \exp(-I(t))}{k!} \int_V p(r)\delta(\varepsilon \mathrm{PSF}(r) - I(t))dI(t)dr \\ &= \frac{1}{V}\int_0^\infty \int_V \frac{(I(t))^k \exp(-I(t))}{k!} p(r)\delta(\varepsilon \mathrm{PSF}(r) - I(t))dI(t)dr \\ &= \frac{1}{V}\int_V \frac{\left(\varepsilon \exp\left(-2\frac{x^2+y^2}{\omega_{xy}^2} - 2\frac{z^2}{\omega_z^2}\right)\right)^k \exp\left(-\varepsilon \exp\left(-2\frac{x^2+y^2}{\omega_{xy}^2} - 2\frac{z^2}{\omega_z^2}\right)\right)}{k!} dr \\ &= \frac{1}{V}\int_V \mathrm{Poi}(k, \varepsilon \mathrm{PSF}(r))dr \end{aligned} \tag{2.38}$$

Here, the detection efficiency η_D from equation 2.32 is incorporated into the brightness ε. Furthermore, we made use of the fact, that the order of integration of the double integral in the second row of equation 2.38 is interchangeable. The last row of equation 2.38 can further be evaluated analytically which finally gives the photon counting histogram (PCH) for a single molecule $p^{(1)}(k)$ in terms of an incomplete gamma function $\gamma(k, \varepsilon)$:

$$p^{(1)}(k|\varepsilon) = \frac{\pi\omega_{xy}^2\omega_z^2}{Vk!} \int_0^\infty \gamma(k, \varepsilon \exp\left(-2x^2\right))dx, \text{ for } k > 0 \tag{2.39}$$

In case of N fluorescent molecules of the same kind being present in the solution, the intensity $I(t)$ is the sum of intensities of all the N molecules. This means that $I(t)$ is the sum of n random variables each having a distribution as given in equation 2.39. Therefore the probability distribution of N molecules giving exactly k photon counts is given by the convolution of N times the single particle PCH:

$$p^{(N)}(k|\varepsilon) = \left[\bigotimes_{i=1}^{N} p^{(1)}\right](k) \tag{2.40}$$

In general, the number of molecules in the observation volume changes due to Brownian motion. They are not confined within a given volume V as assumed before. The

distribution of the number of molecules in the observation volume is governed by a Poisson distribution with mean $\langle N \rangle$:

$$p(N|\langle N \rangle) = \frac{\langle N \rangle^N \exp\left(-\langle N \rangle\right)}{N!} \tag{2.41}$$

Thus the final photon counting histogram $P(k|\varepsilon, \langle N \rangle)$ for one species of molecules is a weighted average of the N-particle PCH with the number occupation distribution (equation 2.41):

$$P(k|\varepsilon, \langle N \rangle) = \sum_{N=0}^{\infty} p^{(N)}(k|\varepsilon) p(N|\langle N \rangle) dN \tag{2.42}$$

The PCH model for an open system does not depend on the reference volume V (see reference [25] for a detailed proof). In accordance with the convention used in fluorescence correlation spectroscopy (FCS, see section 2.1.4.3), the reference volume is chosen to be the volume of the point-spread function (PSF). Thus, $\langle N \rangle$ is also related to this volume and should return the same value as FCS analysis. In this case the Gaussian observation volume can be expressed in terms of the of first- (I_1) and second integral (I_2) of the PSF:

$$V_{\mathrm{3DG}} = \frac{I_1^2}{I_2} = \pi^{\frac{3}{2}} \omega_{xy} \omega_z \tag{2.43}$$

Herein I_1 and I_2 are given by the following expressions:

$$I_1 = \int_V \mathrm{PSF}(r) dr \qquad I_2 = \int_V \mathrm{PSF}^2(r) dr \tag{2.44}$$

To obtain the PCH for 2 species with ε_1, $\langle N_1 \rangle$ and ε_2, $\langle N_2 \rangle$, respectively, the corresponding one species PCHs (equation 2.42) have to be convolved:

$$P(k|\varepsilon_1, \varepsilon_2, \langle N_1 \rangle, \langle N_2 \rangle) = P(k|\varepsilon_1, \langle N_1 \rangle) \otimes P(k|\varepsilon_2, \langle N_2 \rangle) \tag{2.45}$$

Gaussian approximation correction

Huang *et al.* showed that the 3D-Gaussian approximation (equation 2.33) is rather inadequate to describe the PSF for one-photon excitation [26, 27]. They derived a semi-empirical correction procedure which takes into account out-of-focus emission. They used electromagnetic diffraction theory in order to calculate the actual observation volume profile and compared it to its 3D-Gaussian approximation. Furthermore they calculated the j-th integral (for $j = 1..7$, see also equation 2.38 and 2.43) of both the

calculated and Gaussian observation volume profiles (f_j and $f_{3\mathrm{DG},j}$, respectively) and found that especially for $j = 1$ both differed tremendously. Lets define the relative difference between f_j and $f_{3\mathrm{DG},j}$:

$$F_j = \frac{f_j - f_{3\mathrm{DG},j}}{f_{3\mathrm{DG},j}} \tag{2.46}$$

These correction factors are further used in the equation for the reference volume:

$$V = \frac{I_1^2}{I_2} = \frac{(1+F_1)^2}{1+F_2} V_{3\mathrm{DG}} \tag{2.47}$$

In order to incorporate this into the PCH model function, the exponential term in the second to last row of equation 2.38 is expanded into a Taylor-series:

$$\begin{aligned} p(k|\varepsilon) &= \frac{1}{V} \int_V \frac{\left(\varepsilon \exp\left(-2\frac{x^2+y^2}{\omega_{xy}^2} - 2\frac{z^2}{\omega_z^2}\right)\right)^k \exp\left(-\varepsilon \exp\left(-2\frac{x^2+y^2}{\omega_{xy}^2} - 2\frac{z^2}{\omega_z^2}\right)\right)}{k!} dr \\ &= \frac{\varepsilon^k}{Vk!} \int_V \mathrm{PSF}(r)^k \exp\left(-\varepsilon \mathrm{PSF}(r)\right) \\ &= \frac{\varepsilon^k}{Vk!} \int_V \mathrm{PSF(r)}^k \sum_{j=0}^{\infty} \frac{(\varepsilon \mathrm{PSF}(r))^j}{j!} dr \\ &= \frac{1+F_2}{(1+F_1)^2 V_{3\mathrm{DG}} k!} \sum_{j=k}^{\infty} \frac{(-1)^{j-k}}{(j-k)!} \varepsilon^j I_j \end{aligned} \tag{2.48}$$

Herein I_j denotes the j-th PSF integral, i.e. $I_j = \int_V \mathrm{PSF}^j(r) dr$ To express the corrected PCH in terms of the PCH derived for the 3D-Gaussian one can first express the 3D-Gaussian PCH as follows:

$$p_{3\mathrm{DG}}(k|\varepsilon) = \frac{1}{V_{3\mathrm{DG}} k!} \sum_{j=k}^{\infty} \frac{(-1)^{j-k}}{(j-k)!} \varepsilon^j I_{3\mathrm{DG},j} \tag{2.49}$$

Then the following expression gives the corrected PCH model:

$$p(k|\varepsilon) = \frac{1+F_2}{(1+F_1)^2} \left(p_{3\mathrm{DG}} + \frac{1}{k!} \sum_{j=k}^{\infty} \frac{(-1)^{j-k}}{(j-k)!(2j)^{\frac{3}{2}}} \varepsilon^j F_j \right) \tag{2.50}$$

As a first-order correction, all F_j-values with $j > 1$ equate to zero, which means that it is assumed that the higher-order integrals of the PSF are equal for the 3D-Gaussian case and the calculated case. This reduces equation 2.50 to:

$$p(k|\varepsilon) = \begin{cases} \frac{1}{(1+F_1)^2}\left(p_{3\mathrm{DG}} + \frac{\varepsilon F_1}{\sqrt{8}}\right), & \text{for } k = 1 \\ \frac{1}{(1+F_1)^2} p_{3\mathrm{DG}}, & \text{for } k > 1 \end{cases} \tag{2.51}$$

In this work only a first-order correction was applied (see figure 2.4).

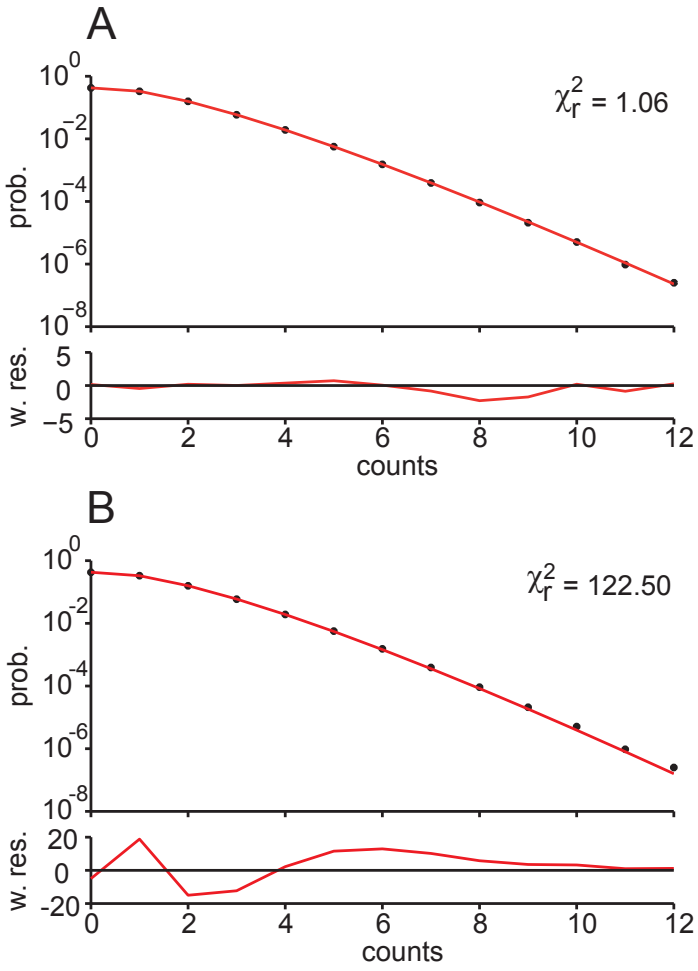

Figure 2.4: Photon counting histogram of Alexa Fluor 488 maleimide in water fitted with first-order out-of-focus correction (**A**) and without first-order out-of-focus correction (**B**). The reduced chi-squared values (χ^2_r) and weighted residuals (w. res.) show that the conventional PCH model (equation 2.42) derived for the 3D-Gaussian approximation to the observation is insufficient.

From a practical point of view, PCH analysis is usually limited to a maximum of two species, which already requires good data quality and incoporation of background information. The fitting is done with a downhill simplex minimising the reduced χ-squared value (χ^2_r) between experimental PCH $\tilde{P}(k)$ and model PCH $P(k|\varepsilon, \langle N \rangle)$:

$$\chi_r^2 = \frac{\sum_{k=k_{\min}}^{k_{\max}} \left[M \frac{\tilde{P}(k) - P(k|\varepsilon, \langle N \rangle)}{s} \right]^2}{k_{\max} - k_{\min} - n_{\text{par}}} \tag{2.52}$$

Herein M is the total number of counts, $k_{\min}$ and $k_{\max}$ are the minimum and maximum counts, respectively. s denotes the standard deviation and n_{par} the number of fit parameters.

Since PCH analysis is done on intensity fluctuation data for a given (short) time interval T, it lacks information about diffusion. In the following section, it will be shown how to relate PCH analysis to the well-known fluorescence correlation spectroscopy (FCS). As in the case of the N&B method one can correct for the bin-time effect. For more details see section 2.1.4.1.

2.1.4.3 Fluorescence Correlation Spectroscopy (FCS)

Assume a fluorescent molecule is found at position r_1. Then the probability to receive k_1 photons counts from that molecule is given by a Poisson distribution $p^{(1)}(k_1|\varepsilon, r_1) = \text{Poi}(k_1, \varepsilon \text{PSF}(r_1))$ as in the case of an immobilized molecule (see equation 2.31). The probability to diffuse from position r_1 to position r_2 within a time interval $\tau = t_2 - t_1$ is given by the solution of the diffusion equation and results in the Green function:

$$p(r_2|r_1, \tau) = \frac{1}{(4\pi D\tau)^{\frac{3}{2}}} \exp\left(-\frac{(r_1 - r_2)^2}{4D\tau} \right) \tag{2.53}$$

Furthermore, the probability to receive k_2 photon counts from position r_2 again is given by a Poisson distribution $p^{(1)}(k_2|\varepsilon, r_2) = \text{Poi}(k_2, \varepsilon \text{PSF}(r_2))$. Taken together, the joint probability to receive k_1 photon counts from position r_1, diffuse to position r_2 within time τ and receive k_2 photon counts from this position is then given by [28, 29]:

$$p(k_1, k_2|\tau, \varepsilon) = \int_{\mathbb{R}^3} \int_{\mathbb{R}^3} p(r_2|r_1, \tau) p(r_1) \text{Poi}(k_1, \varepsilon \text{PSF}(r_1)) \text{Poi}(k_2, \varepsilon \text{PSF}(r_2)) dr_1 dr_2 \tag{2.54}$$

The formal definintion of an expectation value of the product of two random variables, k_1 and k_2, finally shows the equality of the intensity- and photon count correlation function $\langle I(t)I(t+\tau)\rangle$, $\langle k(t)k(t+\tau)\rangle$, respectively (see also [29]):

$$\begin{aligned}\langle k(t)k(t+\tau)\rangle &= \sum_{k_1=0}^{\infty}\sum_{k_2=0}^{\infty} k_1 k_2 p(k_1,k_2|\tau,\varepsilon) \\ &= \int_{\mathbb{R}^3}\int_{\mathbb{R}^3} p(r_1)I(r_1)p(r_2|r_1,\tau)I(r_2)dr_1dr_2 \\ &= \langle I(t)I(t+\tau)\rangle\end{aligned} \tag{2.55}$$

Here the fact that $\sum_{k_i=0}^{\infty} k_i \mathrm{Poi}(k_i, \varepsilon\mathrm{PSF}(r_i)) = \langle k_i\rangle$ was used [25]. In addition the ergodic theorem was assumed to be valid which states that the time-average is equal to the ensemble average.
In the following an analytical expression for the second row in equation 2.55 will be derived.
In general, the time-dependent intensity $I(t)$ can be described in terms of intensity fluctuations $\delta I(t)$ around an average intensity $\langle I\rangle$, namely $I(t) = \langle I\rangle + \delta I(t)$. If this is inserted into the last row of equation 2.55, then the following expressions are equal:

$$\begin{aligned}\langle I(t)I(t+\tau)\rangle &= \langle (\langle I\rangle + \delta I(t))\,(\langle I\rangle + \delta I(t+\tau))\rangle \\ &= \langle I(t)\rangle^2 + \langle I(t)\rangle \underbrace{\langle \delta I(t) + \delta I(t+\tau)\rangle}_{=0} + \langle \delta I(t)\delta I(t+\tau)\rangle \\ &= \langle I(t)\rangle^2 + \langle \delta I(t)\delta I(t+\tau)\rangle\end{aligned} \tag{2.56}$$

Dividing both sides of equation 2.56 by the average intensity squared ($\langle I(t)\rangle^2$) gives the (normalised) autocorrelation:

$$G(\tau) = \frac{\langle I(t)I(t+\tau)\rangle}{\langle I(t)\rangle^2} = 1 + \frac{\langle \delta I(t)\delta I(t+\tau)\rangle}{\langle I(t)\rangle^2} \tag{2.57}$$

However, the cross-correlation is correspondingly given by:

$$G_{1,2}(\tau) = 1 + \frac{\langle \delta I_1(t)\delta I_2(t+\tau)\rangle}{\langle I_1(t)\rangle\langle I_2(t)\rangle} \tag{2.58}$$

Herein $I_1(t)$ and $I_2(t)$ denote intensities from detector 1 and detector 2. The average intensity $\langle I(t)\rangle$ in equation 2.57 can be calculated by integrating equation 2.34 over the r-space:

$$\langle I(t)\rangle_t = \langle I(r)\rangle_r = \int_{\mathbb{R}^3} \varepsilon\mathrm{PSF}(r)dr \tag{2.59}$$

Here again the ergodic theorem was applied. Using this and equation 2.56 in the definition of the autocorrelation function (equation 2.57) finally gives:

$$\begin{aligned} G(\tau) &= \frac{\frac{1}{V}\varepsilon^2 \int\limits_{\mathbb{R}^3}\int\limits_{\mathbb{R}^3} \mathrm{PSF}(r_1)\frac{1}{(4\pi D\tau)^{\frac{3}{2}}}\exp\left(-\frac{(r_1-r_2)^2}{4D\tau}\right)\mathrm{PSF}(r_2)dr_1dr_2}{\frac{1}{V^2}N\varepsilon^2\left[\int\limits_{\mathbb{R}^3}\mathrm{PSF}(r)dr\right]^2} \\ &= \frac{\int\limits_{\mathbb{R}^3}\int\limits_{\mathbb{R}^3} \mathrm{PSF}(r_1)\frac{1}{(4\pi D\tau)^{\frac{3}{2}}}\exp\left(-\frac{(r_1-r_2)^2}{4D\tau}\right)\mathrm{PSF}(r_2)dr_1dr_2}{\frac{N}{V}\left[\int\limits_{\mathbb{R}^3}\mathrm{PSF}(r)dr\right]^2} \end{aligned} \tag{2.60}$$

Herein we set $p(r) = 1/V$ and $p(r_2|r_1,\tau)$ equal to Green's function of diffusion (see also section 2.1.4.2). The number N of fluorescent molecules in the sample divided by the sample volume V is equal to the concentration $c = \frac{N}{V} = \frac{N_{\mathrm{PSF}}}{V_{\mathrm{PSF}}}$ and equal to the number of molecules N_{PSF} in a subvolume V_{PSF} divided by this volume. $V_{\mathrm{PSF}} = \int_{\mathbb{R}^3}\mathrm{PSF}(r)dr$ is often referred to as confocal volume.

1-focus FCS

Performing the integral in the denominator of equation 2.60 gives the volume of the point spread function squared, which in case of a 3D-Gaussian PSF is given by $\left[\int\limits_{\mathbb{R}^3}\mathrm{PSF}(r)dr\right]^2 = \left[\pi^{3/2}\omega_{xy}^2\omega_z 8^{-1/2}\right]^2$ which, as a result, gives the following expression for $G(\tau)$:

$$G(\tau) = \frac{\gamma}{cV_{\mathrm{PSF}}}\int\limits_{\mathbb{R}^3}\int\limits_{\mathbb{R}^3}\mathrm{PSF}(r_1)\frac{1}{(4\pi D\tau)^{\frac{3}{2}}}\exp\left(-\frac{(r_1-r_2)^2}{4D\tau}\right)\mathrm{PSF}(r_2)dr_1dr_2 \tag{2.61}$$

In order to be consistent with most FCS literature [19] we use the effective volume V_{eff} instead of the confocal volume V_{PSF}. This leads to the fact that one can skip the so-called gamma factor $\gamma = 8^{-1/2}$. Performing the double integral in equation 2.61 for a 3D-Gaussian observation volume profile can be done analytically [30] and finally leads to the expression for the correlation function for one diffusing species:

$$G(\tau) = \frac{1}{N_{\mathrm{eff}}}\left(1+\frac{4D\tau}{\omega_{xy}^2}\right)^{-1}\left(1+\frac{4D\tau}{\omega_z^2}\right)^{-1/2} \tag{2.62}$$

Herein N_{eff} denotes the average number of particles in the effective volume. Equation 2.62 is used to estimate the parameters ω_{xy} and ω_z in a calibration experiment. For that purpose, one performs a FCS measurement with a dye of known diffusion coefficient and fixes the D in equation 2.62 whereas ω_{xy}, ω_z and N_{eff} are variable fit parameters.

The correlation function $G(\tau)$ is often expressed in terms of the diffusion time τ_{diff} using the follwing expression:

$$D = \frac{\omega_{xy}^2}{4\tau_{\text{diff}}} \tag{2.63}$$

Thus, equation 2.62 can be rewritten as follows:

$$G(\tau) = \frac{1}{N_{\text{eff}}} \left(1 + \frac{\tau}{\tau_{\text{diff}}}\right)^{-1} \left(1 + \frac{\tau}{k^2 \tau_{\text{diff}}}\right)^{-1/2} \tag{2.64}$$

Herein $k = \omega_z/\omega_{xy}$ is defined as the ratio of the axial to lateral beam waist of the 3D-Gaussian PSF (see equation 2.33). Another source of intensity fluctuations is

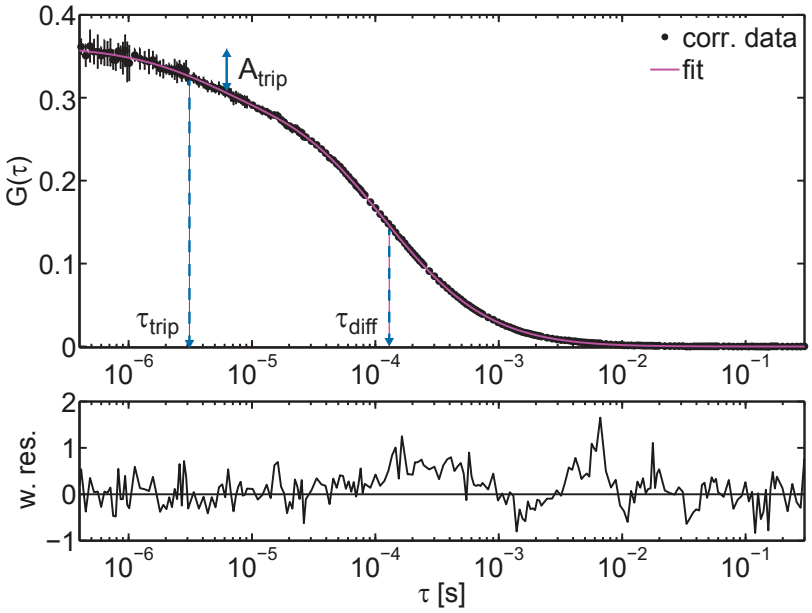

Figure 2.5: Correlation curve of a measurement of AF488-C(0)Aβ_{42} monomers in 10 mM phosphate buffer (pH 7.4). The raw data was divided into 10 equal subsections which were correlated separately and then averaged (black dots, •). The errorbars at each data point represent the standard deviation from the 10 correlation curves. The appropriate fit (to equation 2.65) is shown in magenta in the same plot. Weighted residuals are shown in black in the lower panel.

triplet state dynamics, with typical decay times of a few microseconds. To account for these, one can simply add an expression including the amplitude A_{trip} and the triplet decay time τ_{trip} as follows:

$$G(\tau) = \frac{1}{N_{\text{eff}}} \left[\left(1 + \frac{\tau}{\tau_{\text{diff}}}\right)^{-1} \left(1 + \frac{\tau}{k^2 \tau_{\text{diff}}}\right)^{-1/2} + \frac{A_{\text{trip}} \exp\left(-\frac{\tau}{\tau_{\text{trip}}}\right)}{1 - A_{\text{trip}}} \right] \tag{2.65}$$

An example of a correlation curve with the corresponding fit to equation 2.65 is shown in figure 2.5. This figure has a semilogarithmic τ-axis which is common practice in FCS since correlations exist over several orders of magnitude. Correspondingly, the algorithm which is used to generate the correlation curves is based on a quasi-logarithmic τ scale. This so-called multi-tau algorithm [31] was implemented in MATLAB.

Dual-focus FCS (2fFCS)

2fFCS is based on two overlapping laser foci separated by a fixed shift distance δ. This distance, once determined, is a very robust parameter and does not change with refractive index, cover slide thickness, laser intensity, etc. [32]. In order to incorporate the shift distance δ into the correlation model function, a modified PSF was developed by Dertinger *et al.* [33]. Based on a Gaussian-Lorentzian PSF each observation volume can be described by:

$$\mathrm{PSF}(r) = \frac{\kappa(z)}{\omega(z)^2} \exp\left(-\frac{2}{\omega(z)^2}\left[\left(x \pm \frac{\delta}{2}\right)^2 + y^2\right]\right) \tag{2.66}$$

with

$$\omega(z) = \omega_0 \left(1 + \left(\frac{\lambda_{\mathrm{ex}} z}{\pi \omega_0^2 n}\right)^2\right)^{1/2} \tag{2.67}$$

and

$$\kappa(z) = 1 - \exp\left(-\frac{2a^2}{R^2(z)}\right) \tag{2.68}$$

Therein λ_{ex} denotes the excitation wavelength of the laser. n denotes the refractive index of the immersion medium. ω_0 is the radial beam waist. a is the radius of the pinhole divided by the magnification [34]. $R(z)$ is given as follows:

$$R(z) = R_0 \left(1 + \left(\frac{\lambda_{\mathrm{em}} z}{\pi R_0^2 n}\right)^2\right)^{1/2} \tag{2.69}$$

Therein λ_{em} denotes the wavelength of maximum fluorescence emission. R_0 in equation 2.69 and ω_0 in equation 2.67 are unknown model parameters which are fitted during the analysis. Using this PSF (equation 2.66) in equation 2.60 one finally obtains the following correlation function for diffusion:

$$G(\tau|\delta) = \frac{\varepsilon_1\varepsilon_2}{4c}\sqrt{\frac{\pi}{D\tau}}\int_{-\infty}^{\infty}\int_{-\infty}^{\infty}\frac{\kappa(z_1)\kappa(z_2)}{8D\tau+\omega(z_1)^2+\omega(z_2)^2}\cdot \exp\left(-\frac{(z_2-z_1)^2\,2\delta^2}{4D\tau(8D\tau+\omega(z_1)^2+\omega(z_2)^2)}\right)dz_2dz_1 \tag{2.70}$$

The integrations are not tractable analytically and have to be done numerically. Two different brightness values are used in equation 2.70 to account for different detection efficiencies for each observation volume. When δ is set to zero, equation 2.70 describes the diffusion fit model for the autocorrelation curves. When it is fixed to the known shift distance it describes the diffusion fit model for the cross-correlation curve for both observation volumes. Thus, in comparison to 1fFCS, 2fFCS can fit four correlation curves in a global manner, namely two autocorrelation curves and two cross-correlation curves (see figure 2.6).

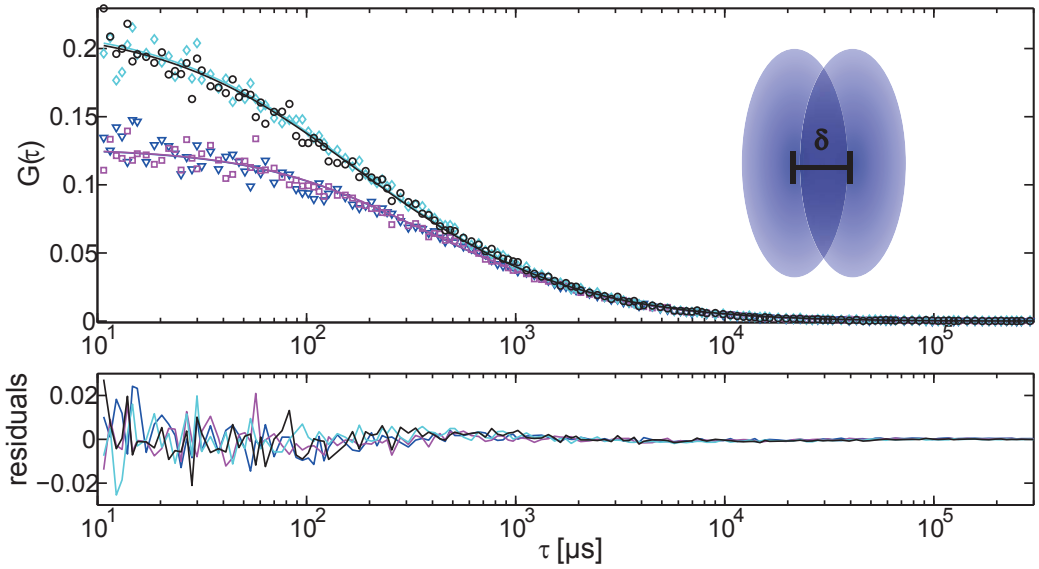

Figure 2.6: Auto- and cross-correlation curves obtained in dual-focus FCS. The inset shows two overlapping observation volumes separated by a (known) distance δ. Two autocorrelation curves are obtained when correlating photons originating from each of the observation volumes separately (▽, □). Two cross-correlation curves are obtained by correlating photons from one observation volume with photons from the other observation volume and *vice versa* (○, ◇).

In contrast to 1fFCS, the diffusion coefficient obtained from 2fFCS is an absolute quantity since no calibration is necessary.

Hydrodynamic parameters from FCS analysis

The diffusion coefficient D is usually the parameter of interest when performing FCS analysis. For a given viscosity and temperature of the solution, D is related to the Stokes radius R_H[3] by the Stokes-Einstein equation:

$$D = \frac{k_B T}{6\pi\eta R_H} \tag{2.71}$$

Herein k_B denotes the Boltzmann constant, T and η are the absolute temperature and viscosity of the solution, respectively. R_H is defined as the radius of a sphere with the same diffusion properties as the molecule under investigation. The assumption of a spherical molecule shape will be violated in almost any case of experimental interest. Many molecules can rather be approximated by a spheroid with symmetry axis (a) and transverse axis (b) (e.g. Lysozyme, see [35]). However, if a molecule is spheroidal, the apparent hydrodynamic radius R_{app} (relative to the solid sphere) will depend on the axis ratio $p = a/b$. The relationship between R_{app} and p is given by Perrin's equation [36] which is depicted in figure 2.7. It shall be noted, that Perrin's equation solely considers geometrical aspects without taking into account the hydration shell. Nevertheless, figure 2.7 can be used to assess the effect of a non-spherical molecule geometry. In the range of $0.5 < p < 2$ the apparent hydrodynamic radius does not even change by 5 %. As a result, approximating the shape as spherical is still a reasonable assumption within this p-range.

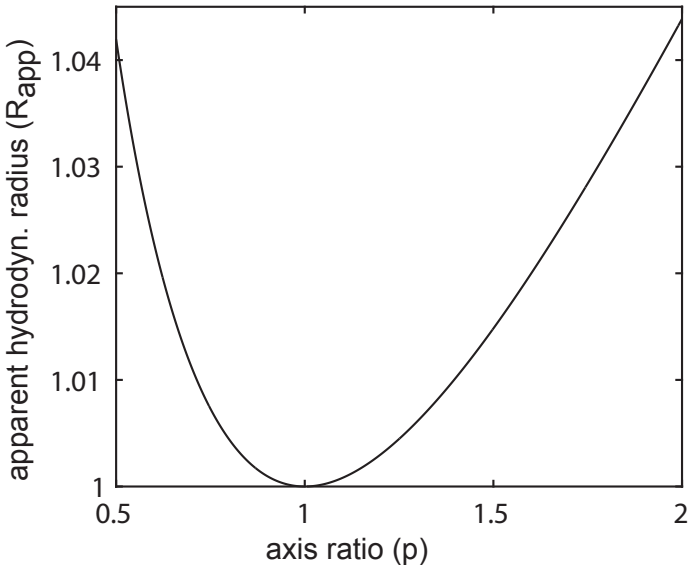

Figure 2.7: Apparent hydrodynamic radius R_{app} as a function of the axis ratio p. the solid black line was calculated according to Perrin's equation [36]

[3] In the course of this thesis, I will often denote this as hydrodynamic radius.

2.2 Accessible volume simulation

An accessible volume (AV) simulation performs a geometric search of all possible positions of a dye attached to a macromolecule. Herein, the dye is approximated by a sphere of radius R and a flexible linkage, which is assumed to be covalently bound to the macromolecule at a specific attachment point. The linker is parametrised by its width w_{linker} and length L_{linker}. During the simulation, all positions which cause a steric clash (when the Van Der Waals volumes overlap) of either the dye or the linker with the macromolecule are rejected. In general, a typical dye has quite different spatial dimensions in the x-, y-, z-direction. To take this into account, three independent AV simulations are performed each with a different dye radius R_i (see figure 2.8). The corresponding volumes are finally superimposed. Since the AV method is solely based on a geometric search algorithm and does not take into account any kind of interaction between the dye-linker and macromolecule (in contrast to MD simulations), it performs whithin a few seconds. For more details I refer to the following informative papers [37–39]. All positions which are accessible to the dye can be visualised by a so-called dye-cloud.

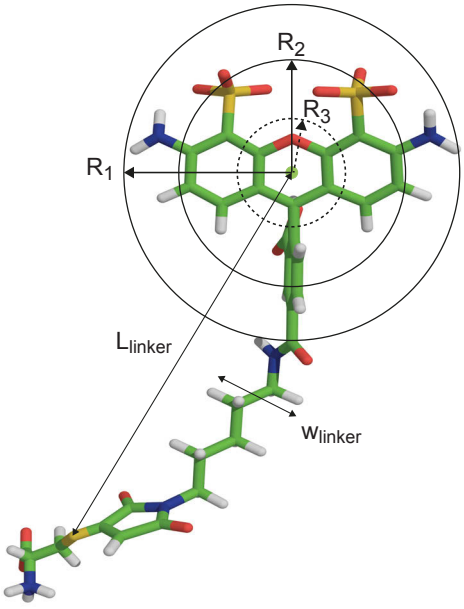

Figure 2.8: Dye parameters for the accessible volume (AV) simulation. The fluorophore structure is approximated by a sphere of radius R_i. The dye is coupled to the protein via a flexible linker of effective length L_{linker} and width w_{linker}. In order to take into account the different dimensions of the dye, a threefold simulation with three different dye radii $R_1, \ldots, R_3$ is performed. The resulting accessible volumes are subsequently superimposed (for details refer to [37]).

2.3 Bayesian data analysis

2.3.1 Bayesian model inference

Bayesian data analysis is based on Bayes theorem:

$$p(\theta|D,I) = \frac{p(D|\theta,I)p(\theta|I)}{p(D|I)} \tag{2.72}$$

Herein D denotes the data that is received from an experiment, θ denotes the hypothesis under which the data is assumed to have arisen. Some background information I is almost always implicitly given to the experimenter. $p(D|\theta,I)$ is referred to as the likelihood. $p(\theta|I)$ and $p(D|I)$ denote the prior and evidence, respectively. Equation 2.72 transforms the likelihood, i.e. the probability of the data given the hypothesis, into a function of the hypothesis (poterior probability) given the data (see figure 2.9[4].). The vertical bars in equation 2.72 indicate conditional dependencies of the

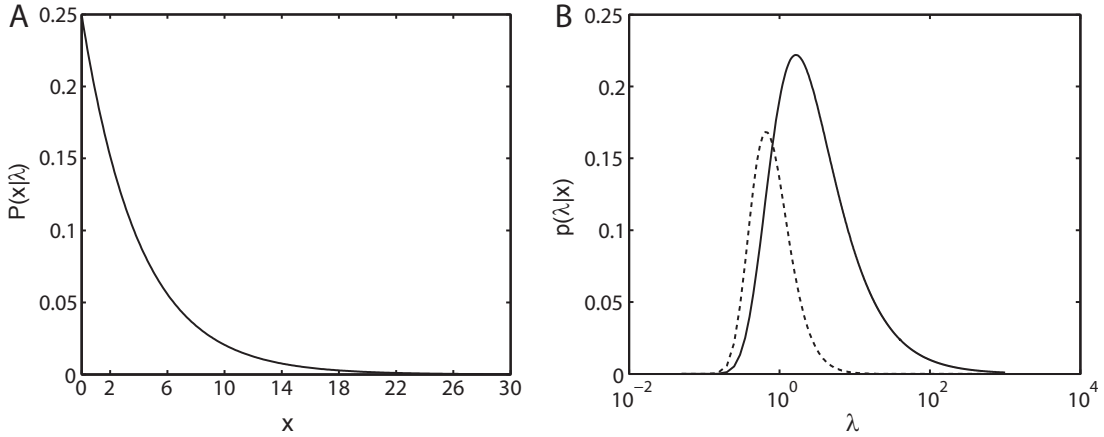

Figure 2.9: (**A**) Exponential likelihood function $p(x|\lambda) = 1/\lambda \exp(-x/\lambda)$ for a given hypothesis as a function of the sample space x. (**B**) However, $p(x|\lambda) = 1/\lambda \exp(-x/\lambda)$ can also be read as a function of λ for given datasets $\{x_i\}_{i=1}^M$. Here, two different datasets: $\{x_1, x_2, x_3\}$ (dashed line) and $\{x_1\}$ (solid line) were used to plot the likelihood as a function of λ ($p(\lambda|\{x_i\}_{i=1}^M) = \prod_{i=1}^M p(\lambda|x_i)$). If this function is normalised (as in this figure), it corresponds to the posterior probability (given a constant prior). It is important to note that the likelihood becomes tighter the more data points (x_i) are available.

corresponding probabilities. In this work, Bayesian model inference is applied in order

[4]This example is from [40]

to compare different models M with each other. Applying Bayes theorem we can calculate the probability of a model M given a subset of data D according to equation 2.73:

$$p(M|D) = \frac{p(D|M,I)p(M|I)}{p(D|I)} \tag{2.73}$$

where $p(M|I)$ and $p(M|D,I)$ denote the prior and posterior probability, respectively. $p(D|M,I)$ denotes the marginal likelihood of the data. It is calculated by averaging the (parameter) likelihood $p(D|\theta,M,I)$ over all model parameters θ weighted by their prior probability $p(\theta|M,I)$:

$$p(D|M,I) = \int\limits_{\text{all }\theta} p(D|\theta,M,I)p(\theta|M,I)d\theta \tag{2.74}$$

$p(D|I)$ in equation 2.73 is called the evidence of the data and is calculated by summing the marginal likelihoods over all possible models, i.e. $p(D|I) = \sum_{j=1}^{m} p(D|M_j,I)p(M_j|I)$. In order to infer one of two competing models (M_1 and M_2) which most plausibly describe the data, the posterior ratio (posterior odds) can be used:

$$\frac{p(M_1|D,I)}{p(M_2|D,I)} = \frac{p(D|M_1,I)p(M_1|I)}{p(D|M_2,I)p(M_2,I)} \tag{2.75}$$

If equal model priors $p(M_1) = p(M_2) = 0.5$ are applied, then model comparison breaks down to comparing the corresponding marginal likelihoods $P(D|M_1,I) = \int_{\theta_1} p(D|\theta_1,M_1)p(\theta_1|M_1)d\theta_1$ and $P(D|M_2,I) = \int_{\theta_2} p(D|\theta_2,M_2,I)p(\theta_2|M_2)d\theta_2$. Depending on the number of parameters θ, these integrals can become high-dimensional. However, a Laplace approximation was applied to deal with this problem (see section 2.3.2).

2.3.2 Laplace approximation of the evidence

If the likelihood function $p(D|\theta,M,I)$ (equation 2.74) is not given in an explicit form or/and the parameter space is high dimensional, the evidence has to be calculated numerically. There exist various methods to deal with the integral in equation 2.74 ranging from (analytical) approximations to Monte-Carlo methods. However, since Monte-Carlo methods are very time-consuming, we chose the Laplace approximation as the method of choice to calculate the marginal likelihood. In order to apply Laplace's

approximation to equation 2.74, it is assumed that the likelihood function $p(D|\theta, M, I)$ is highly peaked around its maximum $\hat{\theta}$ and that the prior is very flat (almost constant) over the parameter space. Then the peak might be approximated by a Gaussian function [41]:

$$p(D|\theta, M, I) = p(D|\hat{\theta}, M, I) \exp\left(-\frac{(\theta - \hat{\theta})^2}{2\delta\theta^2}\right) \tag{2.76}$$

Herein $p(D|\hat{\theta}, M, I)$ denotes the maximum of the likelihood. $\delta\theta$ is the standard deviation of the Gaussian which is usually a function of the number of elements in the data vector D (see also figure 2.9). It is equal to the uncertainty of the parameter estimate $\hat{\theta}$. If we further assume that the prior is constant ($\neq 0$) within the range $\theta_{\min} \leq \theta \leq \theta_{\max}$ and zero otherwise, we can simplify equation 2.74 to:

$$\begin{aligned} p(D|M, I) =& \frac{p(D|\hat{\theta}, M, I)}{\theta_{\max} - \theta_{\min}} \int_{\theta_{\min}}^{\theta_{\max}} \exp\left(-\frac{(\theta - \hat{\theta})^2}{2\delta\theta^2}\right) d\theta \\ =& \frac{p(D|\hat{\theta}, M, I)\sqrt{2\pi}\delta\theta}{\theta_{\max} - \theta_{\min}} \end{aligned} \tag{2.77}$$

Equation 2.77 calculates the marginal likelihood for a one-dimensional parameter space. However, it can be generalised to a multidimensional parameter space (using a more general prior $p(\theta|M, I)$) [40]:

$$p(D|M, I) = p(D|\hat{\theta}, M, I)p(\theta|M, I)\det{}^{-1/2}\left(\frac{\mathbf{A}}{2\pi}\right) \tag{2.78}$$

Herein $\mathbf{A}$ denotes a $n \times n$ Hessian matrix with $\dim(A) = \dim(\theta)$. Equation 2.78 plays an important role for our development of a Bayesian burst identification method (see section 4.9).

2.4 Biochemical principles

2.4.1 Alzheimer's disease

About 46 million people worldwide suffer from dementia [1], most of them suffer from Alzheimer's disease (AD) [2]. Alois Alzheimer, a german psychiatrist, published a paper about "an unusual illness of the cerebral cortex" (free engl. translation, see [42]) in 1907. This is why he is attributed to have discovered the disease and why it is called Alzheimer's disease today. Alzheimer discovered *post-mortem* that his patients' brain was atrophic, i.e. that brain material was degraded. This continuous degradation of brain material (compare figure 2.10 A and B) is why AD patients suffer from loss of memory, loss of language ability and a deterioration of fine motor skills. In his paper, Alzheimer additionally describes the existence of fibrillar tangles inside of a cell and on its surface (figure 2.10 C). Intracellular tangles are usually composed of hyperphosphorylated tau protein, whereas extracellular tangles are mostly composed of amyloid fibrils. These are the two main histopathological criteria for the recognition of AD [43]. In 1984 Glenner and Wong discovered that the major component of amyloid fibrils is a low-molecular-weight peptide of about 4 kDa [44]. This peptide is now referred to as amyloid-β peptide (Aβ).

2.4.2 Amyloid-β peptide

Aβ is derived from the membrane-anchored amyloid precursor protein (APP) (see figure 2.10 D and [45]). $\beta-$secretase catalyses the cleavage of APP at the N-terminal part of the Aβ sequence whereas γ-secretase catalyses the subsequent cleavage of APP at the C-terminal part of the Aβ sequence. Depending on the exact cleavage site, the Aβ peptide evolves in different isoforms ranging from 38 to 43 amino acids [46]. The two most predominant ones are $A\beta_{40}$ and $A\beta_{42}$, respectively. Although the amount of $A\beta_{42}$ is only 10 % of the amount of $A\beta_{40}$, the former one is the more toxic species [6]. Furthermore, $A\beta_{42}$ has a higher aggregation propensity compared to $A\beta_{40}$.
There exist several hypotheses about the development of AD. However, the amyloid cascade hypothesis is one of the most accepted ones. It describes the evolution of Aβ oligomers and fibrils as an aggregation process of the peptides with each other. Initially, it was believed that the fibrils and fibrillar tangles cause the decline of neurons [47] whereas today it is mostly believed that oligomers are the predominant toxic species.

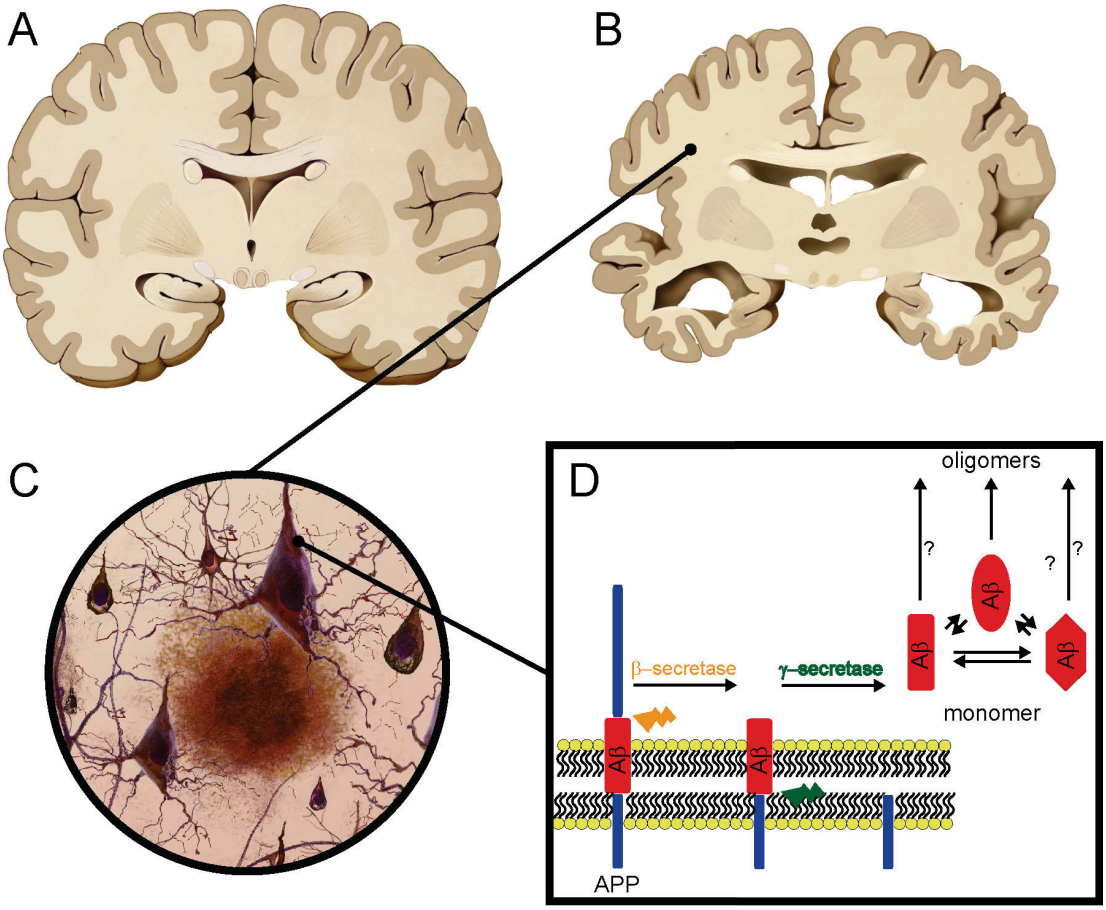

Figure 2.10: (**A**) Schematic representation of a healthy brain. (**B**) Schematic representation of a brain with advanced Alzheimer's disease. (**C**) Fibrillar tangles (brown) outside of neurons in an AD brain are mainly composed of Aβ. (**D**) The Aβ peptide is derived from the membrane-anchored amyloid precursor protein (APP). Upon subsequent cleavage by β- and γ-secretase, the Aβ is released into the extracellular space. Monomeric Aβ might exist in different conformations whose tendency to form oligomers might differ substantially. (**A**,**B**,**C**) adapted from www.nia.nih.gov.

2.4.3 Protein denaturation

According to Tanford the term denaturation can be defined as a "major change from the original native structure, without alteration of the amino acid sequence, i.e. without severance of any of the primary chemical bonds which join one amino acid to another." [48]. Thus, any condition which induces a major conformational change of the native structure can be considered to be a denaturing condition. This can include changes in pH, ionic strength, temperature or the additions of chaotropic substances. Here the term denaturant is used for any substance or condition which promotes protein denaturation. Denaturations can be reversible or irreversible. This, mostly depends on the conditions that are applied to denature a protein. For example, denaturation of RNase T1 with 6 M GdnHCl is reversible but not if it is thermally denatured [49]. However, it has been demonstrated that temperature denaturation often does not lead to a complete denaturation. This among other things, is one reason why we chose chemical denaturation of $A\beta_{42}$ with GdnHCl.
The thermodynamic stability of a protein conformation is determined by its free energy ΔG. From basic thermodynamics the change of free energy ΔG is related to the change of entropy ΔS and to the change of enthalpy ΔH upon transition from the folded to the unfolded state by the following equation:

$$\Delta G = \Delta H - T\Delta S \tag{2.79}$$

In general, the entropy of the folded conformation of a protein is much smaller than for its denatured conformation. This fact is partially compensated by a decrease in enthalpy through pairing of amino acid side chains in the folded state. In the unfolded state, even hydrophobic amino acids are exposed to the solvent. Since water molecules are not able to form hydrogen bonds with these residues, they strengthen their hydrogen network with neighbouring water molecules. This effect is often referred to as *hydrophobic effect*. It leads to a decrease in entropy and enthalpy of the water molecules. Similarly, the hydrophilic backbone of the protein is more exposed to the solvent in the denatured state. The backbone can accept or donate hydrogen bonds and share with water molecules. This leads to a decrease in entropy of the solvent. Conversely, the folding process releases water molecules which leads to an increase in the entropy of water. This compensates for the loss of conformational entropy of the protein. There is an ongoing debate about how denaturants affect proteins. On the one hand, they could change the solvent properties and, on the other hand, they could interact with the protein itself. Nevertheless, in the following it will be assumed that the protein/peptide can exist in a native conformation N which is distinct from its denatured or unfolded conformation U. The denatured conformation can be induced

by denaturants which, especially for small proteins, often leads to a two-state unfolding process [49].

2.4.4 Two-state unfolding of proteins

The "chemical" equation which describes the unfolding process is given as follows:

$$\mathrm{N} \underset{k_N}{\overset{k_U}{\rightleftharpoons}} \mathrm{U} \tag{2.80}$$

One has to choose an appropriate technique to follow structural conversions from N to U. Here, it will be assumed that the measurement variable S (not to be confused with entropy), obtained from the corresponding technique, is a linear combination of the signal of the native and the unfolded conformation respectively.

$$S = \alpha_N S_N + \alpha_U S_U = \alpha_N S_N + (1 - \alpha_N) S_U \tag{2.81}$$

Herein $f_N = \frac{[N]}{[N]+[U]}$ and $f_U = \frac{[U]}{[N]+[U]}$ denote the fractions of the native and unfolded conformation, respectively. With some basic arithmetics it can be shown, that the equilibrium constant K of the reaction in equation 2.80 is given by:

$$K = \frac{[U]}{[N]} = \frac{\alpha_U}{\alpha_N} = \frac{1 - \alpha_N}{\alpha_N} \tag{2.82}$$

Solving equation 2.82 for α_N we obtain:

$$\alpha_N = \frac{1}{1 + K} \tag{2.83}$$

K is related to ΔG, the difference of the Gibbs free energies of the unfolded and folded state (see figure 2.11), by the following equation:

$$K = \exp\left(-\frac{\Delta G}{RT}\right) \tag{2.84}$$

Thus, $\alpha_U = 1 - \alpha_N$ is found to be:

$$\alpha_U = \frac{\exp\left(-\frac{\Delta G}{RT}\right)}{1 + \exp\left(-\frac{\Delta G}{RT}\right)} \tag{2.85}$$

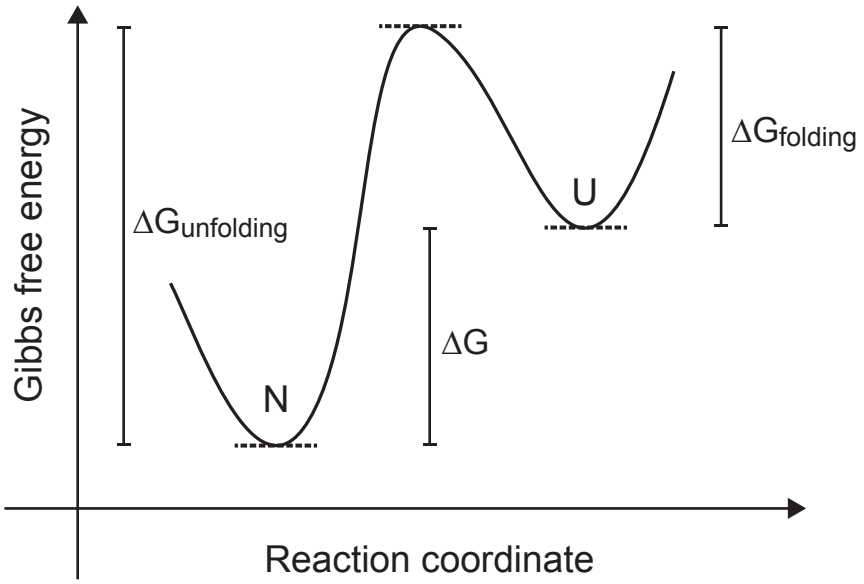

Figure 2.11: Schematic representation of an energy diagram of a two-state unfolding transition of a protein. The Gibbs free energy ΔG denotes the difference between the Gibbs free energy of unfolding and the Gibbs free energy of folding: $\Delta G = \Delta G_{\text{unfolding}} - \Delta G_{\text{folding}}$.

Using equations 2.84 and 2.85 in equation 2.81 we finally obtain:

$$S = \frac{S_N + S_U \exp\left(-\frac{\Delta G}{RT}\right)}{1 + \exp\left(-\frac{\Delta G}{RT}\right)} \tag{2.86}$$

2.4.4.1 GdnHCl unfolding

In this work we applied chemical denaturation of $A\beta_{42}$ with guanidine hydrochloride (GdnHCl). The logarithm of K ($\ln K$) is linearly dependent on the denaturant concentration in the transition region of the unfolding curve. If it is assumed that this dependency can be extrapolated to zero denaturant concentration, one obtains the linear-extrapolation model (LEM, see [50]). Thus, it is reasonable to assume that the free energy ΔG of the system depends linearly on the denaturant concentration $[D]$. According to this model, ΔG can be written as follows:

$$\Delta G = \Delta G^{H_2O} - m[D] \tag{2.87}$$

In equation 2.87, ΔG^{H_2O} denotes the free energy in the absence of denaturant. m is a measure of cooperativity of the transition. Using equation 2.87 in equation 2.86 leads to the model which was used to fit the unfolding curves:

$$S = \frac{S_N + S_U \exp\left(-\frac{\Delta G^{H_2O} - m[D]}{RT}\right)}{1 + \exp\left(-\frac{\Delta G^{H_2O} - m[D]}{RT}\right)} \tag{2.88}$$

m is proportional to the change in the solvent accessible surface area $\Delta SASA$ when going from the native to the denatured conformation. The solvent accessible surface area of an atom is typically defined in terms of the Van der Waals radius of the atom and the radius of the solvent molecule [51]. The empirical relation between m and $\Delta SASA$ is reported in Myers *et al.* [52] and is shown in equation 2.89.

$$m = (958 \pm 270) + (0.23 \pm 0.02)\Delta SASA \tag{2.89}$$

I reanalysed the data from Myers *et al.* [52] in order to obtain the corresponding errors of the fit parameters (given in equation 2.89). However, there is a slight deviation in the intercept, namely 958 in contrast to their value of 953. But this is of minor importance due to its big error.

3

Materials

Contents

3.1 Buffers **37**

3.2 Chemicals **37**

3.3 Instruments **38**

3.4 Software **38**

3.1 Buffers

Sodium phosphate buffer (1 M stock solution) pH 7.4

0.06 M $NaH_2PO_4 \cdot H_2O$
0.94 $Na_2HPO_4 \cdot 2H_2O$
Remark: I use NaPi as a shorthand notation for sodium phosphate buffer

6 M guanidine hydrochloride in 125 mM sodium phosphate buffer pH 7.4

125 mM NaPi via dilution from 1 M NaPi stock solution
6 M guanidine hydrochloride via dilution from 8 M guanidine hydrochloride stock solution

3.2 Chemicals

Water from a Merck Milli-Q water purification system
Di-Sodium hydrogen phosphate dihydrate p.a., AppliChem
Sodium dihydrogen phosphate monohydrate p.a., AppliChem
Hexafluoroisopropanol (HFIP) $\leq$ 99.8 %, Sigma Aldrich
Imidazole, Sigma Aldrich
2-propanol p.a., VWR
Phosphoric acid 85 % p.a., AppliChem
Trifluoroacetic acid 99 %, Sigma Aldrich
Tris(2-carboxyethyl)phosphin-hydrochloride (TCEP), Sigma Aldrich
Acetonitrile HiPerSolv Chromanorm, HPLC grade, VWR
Sodium hydroxide pellets *leq* 97.0 %, Sigma Aldrich
8 M Guanidine-HCl solution, Thermo Scientific
Alexa Fluor 488 maleimide, Life technologies
Alexa Fluor 488 TFP ester, Life technologies
Oregon Green 488 carboxylic acid, Life technologies
AF488-C(0)Aβ_{42} (Lot 3008845), Bachem (was used for a few experiments)
Uvasol N,N-Dimethylformamide for Spectroscopy, VWR
active carbon, VWR

3.3 Instruments

Fluorimeter FP-6500, Jasco
Spectrophotometer V-650, Jasco
SpeedVac (AVC 2-18) with cold-trap LT-105, Christ
Hamilton syringes, Hamilton
Reaction tubes LoBind, Eppendorf
Pipettes, Eppendorf
Pipette tips, Eppendorf
Coverslips # 1, Menzel-Gläser (part of Thermo Scinetific)
384 Well Greiner Microplate, Greiner Bio-One
Superdex 75 3.2/300, GE Healthcare
Agilent HPLC 1260 Infinity, Agilent
Agilent HPLC 1100, Agilent
Zorbax-C8 semipreparative column, Agilent
Zorbax-C8 analytical column, Agilent
Hellmanex II, Hellma
Refractometer, Bausch & Lomb
Micro-Ostwald Viscosimeter, Lauda
Micro-Ostwald viscosimeter capillary Type I (filling vol. 2 ml), Lauda
Denisty meter DMA 5000, Anton Paar
JPK NanoWizard II AFM, JPK Instruments AG
MicroTime 200, PicoQuant
Home-built multiparameter single-molecule fluorescence detection setup composed of (only main parts included):
Olympus IX 71 confocal microscope
Water-immersion objective UPlansApo 60x, Olympus
Blue laser diode LDH-P-C-470, PicoQuant
2 avalanche photo diodes MPD PDM, Micro Photon Devices

3.4 Software

MATLAB 2011b, The Mathworks
OriginPro 9.0G, OriginLab
Pymol, DeLano Scientific
FRET Positioning and Screening (FPS) software [37], Lehrstuhl für Molekulare

Physikalische Chemie, Heinrich-Heine-Universität Düsseldorf
a|e - UV-Vis-IR Spectral Software 1.2, FluorTools, www.fluortools.com
PSF Lab, The One Molecule Group (see [53])

4

Methods

Contents

4.1 Recombinant expression of an Aβ_{42} cysteine variant . . . 41

4.1.1 The expression system 41

4.1.2 Choosing an appropriate cysteine mutation site 42

4.1.3 C(0)Aβ_{42} purification using chromatographic methods . . . 42

4.2 Dye labeling of C(0)Aβ_{42} with Alexa Fluor 488 45

4.3 Viscosity and density measurements 47

4.4 Time-resolved fluorescence measurements 49

4.5 Atomic force microscopy measurements 49

4.6 1fFCS unfolding measurements 50

4.7 2fFCS unfolding measurements 51

4.8 Simulation of single-molecule fluorescence experiments . . 53

4.9 Development of a Bayesian burst identification method . 57

4.9.1 Likelihood function for microtimes 58

4.9.2 Likelihood function for interphoton times 59

4.9.3 Performance evaluation 63

4.1 Recombinant expression of an Aβ$_{42}$ cysteine variant

Remark: All of the molecular biological work was done by my previous master student Chris Cadek. Correspondingly, I will only briefly introduce the expression system. For details about the expression procedure, I refer to her work. The purification of the Aβ peptide is described as part of this work.

4.1.1 The expression system

Due to its high toxicity and aggregation propensity, expressing Aβ$_{42}$ remains challenging. Several expression systems for Aβ$_{42}$ are described in the literature which more or less try to circumvent this issue. E.g. Macao *et al.* coexpressed the Aβ$_{42}$ with an affibody ligand [54]. This affibody binds Aβ with nanomolar affinity and consequently prevents its aggregation. However, the main weakness of this method is the existence of an additional N-terminal methionine at the N-terminus. Although Macao *et al.* showed that MAβ and Aβ are structurally almost equivalent, an additional methionine makes the corresponding MAβ$_{42}$ even more susceptible to oxidation or chemical modification [55]. In order to express Aβ$_{42}$ without N-terminal methionine, we adapted an expression system as described in Finder et al. [56] in which Aβ$_{42}$ is part of a fusion protein whose fusion tag can be cleaved off. The fusion tag consists of tandem repeats of the hydrophylic NANP-unit which acts as a solubility tag.

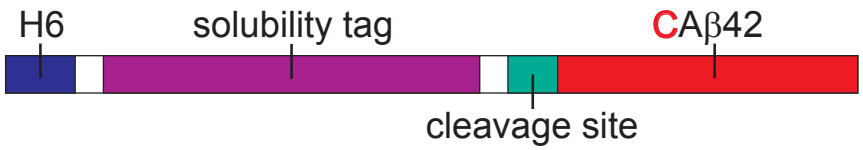

Figure 4.1: Schematic representation of the fusion protein used to express a cysteine variant of Aβ$_{42}$. The fusion protein consists of a terminal hexahistidine tag (blue), a solubility tag NANP$_{19}$ (magenta), a TEV cleavage site and the CAβ$_{42}$ peptide (red). Spacer regions are shown in white.

I received the Ni-NTA pre-purified C(0)Aβ$_{42}$ fusion protein (see figure 4.1) from my previous master student.

4.1.2 Choosing an appropriate cysteine mutation site

If the mutation site, and correspondingly the dye labeling position, is not chosen appropriately then the dye might have a strong influence on the structure of the peptide. Most of the commercially available Aβ_{42} dye-conjugates are labeled N-terminally. Furthermore, N-terminally labeled Aβ_{42} dye conjugates are reported to be able to form fibrils (see e.g. [57] and the discussion therein). Taken together, this indicates that the influence of the dye on the Aβ_{42} structure might be negligible when bound to the N-terminus. Thus, we finally decided to add a cysteine to the N-terminus in order to specifically label this position with Alexa Fluor 488 (AF488) maleimide.

4.1.3 C(0)Aβ_{42} purification using chromatographic methods

The basis of all chromatographic methods is the interaction of analytes in a mobile phase with a stationary phase. The strength of interaction depends on characteristics of the analyte like size (size-exclusion chromatography, SEC), hydrophobicity (reversed-phase high-performance chromatography, rp-HPLC) or affinity (Ni-NTA affinity chromatography). In the following, size-exclusion chromatography and reversed-phase chromatography will be described in more detail.

4.1.3.1 High-performance liquid chromatography (HPLC)

rp-HPLC applies a hydrophobic stationary phase and a more hydrophilic mobile phase. When analytes are applied to the column, two effects dominate the chromatographic process. First, adsorption of analytes occurs at the mobile phase|stationary phase interface. Second, dispersion of analytes occurs between those two phases which can be described by Nernst's law. Each compartment of the column at which a concentration equilibrium occurs between analytes in the mobile and in the stationary phase is called a theoretical plate. The equilibrium constant depends, among other things, on the chemical nature of the analyte, as well as on the chemical nature of the stationary and mobile phase. Thus, it can be influenced by changes in the composition of the mobile phase.
rp-HPLC was applied for further purification of the C(0)Aβ_{42} fusion protein since after Ni-NTA chromatography it was still dissolved in 6 M GdnHCl. GdnHCl had to be removed prior cleavage with a TEV protease. The C(0)Aβ_{42} fusion protein was

purified with an Agilent 1260 HPLC system and a mixture of 29 % AcCN in H_2O + 0.1 % TFA (isocratic conditions) and 80°C column temperature. These conditions were actually applied to all the HPLC separations described in this work. Depending on the type of separation, either analytical or semi-preparative, either an Agilent Zorbax-C8 analytical column was used or an Agilent Zorbax-C8 semi-preparative column. After purifying the C(0)Aβ_{42} fusion protein, the solubility tag was cleaved-off by a TEV protease (0.05 mol TEV per mol fusion protein) in 100 mM Tris-HCl buffer at pH 8 containing 50 mM TCEP. The reaction was performed over night at 4°C. This reaction mixture was then again applied to rp-HPCL (see figure 4.2). The more hydrophylic C(0)Aβ_{42} fusion protein elutes first and the cleaved C(0)Aβ_{42}, which is more hydrophobic, elutes second. The C(0)Aβ_{42} was collected in Greiner

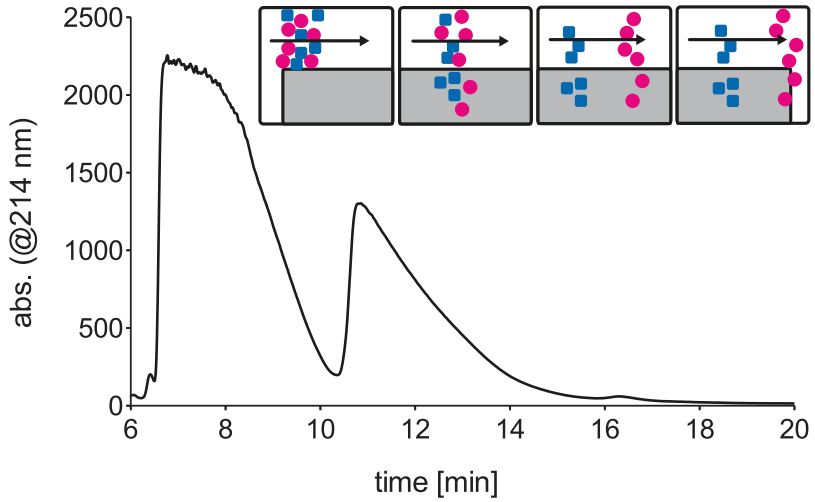

Figure 4.2: HPLC chromatogram of CAβ_{42} (second peak at about 11 minutes) and fusion tagged CAβ_{42} (first peak at about 8 minutes); the inset shortly summarizes the theory behind rp-HPLC. Hydrophobic analyte molecules (■) rather stay in the stationary phase while more hydrophilic analyte molecules (●) stay in the mobile phase and are thus more prone to be carried along.

tubes, subsequently lyophilised and stored at -80°C until further use. We performed MALDI-TOF mass spectrometry to confirm the molar mass of the C(0)Aβ_{42} peptide.

4.1.3.2 Size-exclusion chromatography (SEC)

SEC is a technique which separates molecules according to their frictional coefficient [58]. If the SEC column is calibrated with appropriate proteins whose molecular weight is known and whose shape is similar to the shape of the unknown protein, SEC can be used to determine the molecular weight of that protein. The stationary phase is usually composed of spherical particles which are highly porous. Small particles are

able to enter even small cavities whereas big particles pass the column bed without being retarded and can thus be found in the void volume. Each separation problem needs a corresponding SEC column with the appropriate column bed in order to separate within the molar mass range of interest. In this work, we used a Superdex 75 column (GE Healthcare) which is frequently applied to isolate Aβ$_{42}$ oligomers and/or monomers (see e.g. [59]). An example of a separation of dye-labeled C(0)Aβ$_{42}$ is shown in figure 4.3. The first peak (≈ 10 minutes) elutes in the void volume and can be attributed to oligomers. The second peak (≈ 14.5 minutes) can be attributed to monomeric Aβ$_{42}$. However, according to the column calibration, the second peak would correspond to a molecular weight of about 24 kDa. This discrepancy between the estimated and the nominal molecular weight is a known issue and, for example, discussed in a paper by Walsh *et al.* [59].
All SEC runs were done at a flow rate of 0.1 ml/min and at 4°C column temperature. Typically, we used NaPi buffer (pH 7.4) for elution. The elution buffer was freshly prepared and filtered through a 0.1 μm filter. The column was typically equilibrated with two column volumes (2x2.4 ml) of elution buffer ahead of the sample separation.

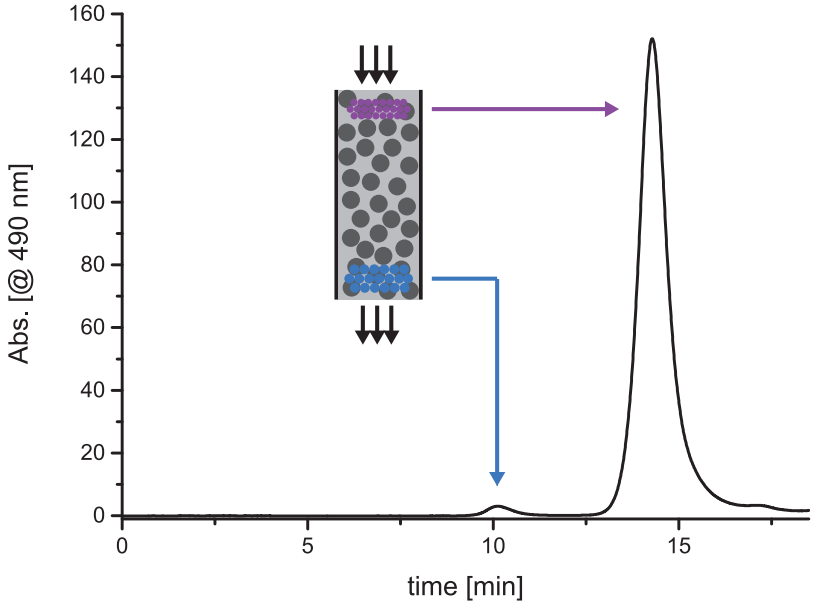

Figure 4.3: SEC chromatogram of AF488-C(0)Aβ$_{42}$. The peaks at about 10 and at 14.5 minutes correspond to oligomeric and monomeric species, respectively

Aβ$_{42}$ monomerisation using SEC

The procedure described above was used to isolate monomeric C(0)Aβ$_{42}$. In order to increase the number of monomers we dissolved lyophilised C(0)Aβ$_{42}$ in 6 M GdnHCl and subsequently applied this solution to the SEC system. A repeated separation of the collected monomer solution leads to a single peak indicating the absence of any detectable oligomers (data not shown). Using GdnHCl to solve the Aβ$_{42}$ lead to a very low residual number of oligomers and to a high amount of monomers (figure 4.3).

Obviously not all oligomers disassembled in high concentrations of GdnHCl which was also confirmed by AFM measurements (see figure 4.4). For the AFM measurement Aβ$_{42}$ oligomers and fibrils were preformed in NaPi buffer and GdnHCl was added to an aliquot after the incubation period (end concentration 5.5 M GdnHCl). The corresponding blank feed did not contain any GdnHCl. Both solutions were further incubated for one more hour and applied to the mica surface (for more details see section 4.5). Figure 4.4 A depicts a representative elevation profile of the sample without GdnHCl. Small oligomers are clearly distinguishable from protofibrils and fibrils. The height of oligomers is typically much smaller than 10 nm. However, fibrils and protofibrils can reach 10 nm height. Small oligomers disaggregate by the addition of GdnHCl while bigger oligomers, protofibrils and fibrils remain (4.4 B). This is in accordance with results reported by Ni *et al.* [60].

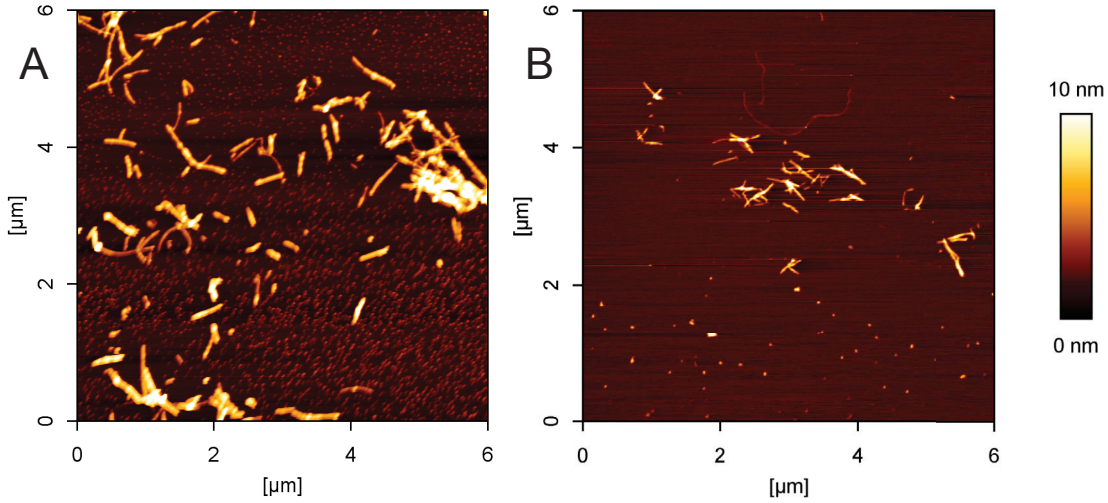

Figure 4.4: Representative AFM images of aggregated Aβ$_{42}$, where GdnHCl is absent in solution (**A**) and where GdnHCl was added to the solution after incubation (**B**).

4.2 Dye labeling of C(0)Aβ$_{42}$ with Alexa Fluor 488

The incorporated cysteine in the C(0)Aβ$_{42}$ sequence was used to specifically attach Alexa Fluor 488 maleimide (Invitrogen) to the N-terminus. The labeling reaction (see figure 4.5) was performed in NaPi containing 6 M guanidine hydrochloride (pH 7.4). The dye was added in fivefold molar excess compared to the C(0)Aβ$_{42}$. In order to keep the thiol groups in a reduced state or to reduce preexisting disulfid-bridged dimers, a tenfold molar excess of Tris(2-carboxyethyl)phosphin (TCEP) was added before the actual reaction. The reaction was performed at room temperature overnight.

Afterwards, the reaction mixture was applied to rp-HPLC to separate AF488-C(0)Aβ$_{42}$ from non-bound dye.

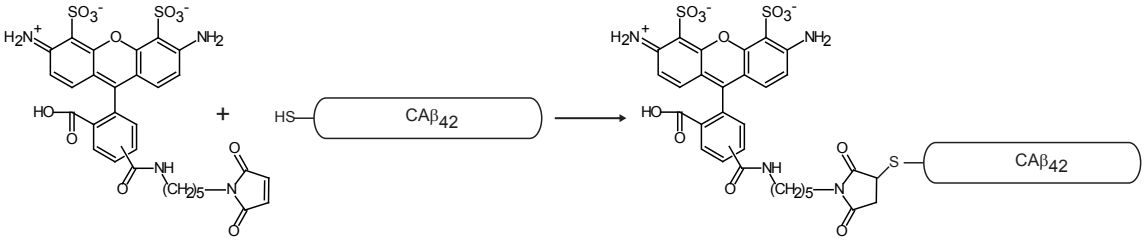

Figure 4.5: Labeling reaction of C(0)Aβ$_{42}$ with Alexa Fluor 488 maleimide

SDS-PAGE and MALDI-TOF MS confirmed the molar mass and purity of the AF488 labeled C(0)Aβ$_{42}$ (see figure 4.6).

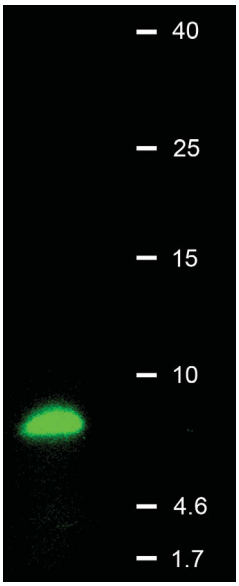

Figure 4.6: SDS-PAGE result of purified and AF488 labeled C(0)Aβ$_{42}$. The existence of a single band points to the high purity and the absence of residual free dye.

The peptide fraction was dried under vacuum and the aliquot was subsequently stored at -80°C until further use.
The coupling efficiency (CE) of AF488 was determined according to equation 4.1 and was found to be almost 100 % (93 %).

$$\mathrm{CE} = \frac{\varepsilon_{280}(\mathrm{Protein}) A_{\max}}{(A_{280} - \mathrm{CF}_{280} A_{\max})\, \varepsilon_{\max}(\mathrm{Dye})} \tag{4.1}$$

4.3 Viscosity and density measurements

Viscosity measurements were performed with an Ostwald capillary viscosimeter. The Hagen-Poiseuille law allows to recover the dynamic viscosity v of the fluid by the following equation:

$$v = \frac{\pi d^4 \Delta p t}{8 V l} \tag{4.2}$$

Herein d denotes the diameter of the capillary, Δp denotes the pressure difference between the upper and lower mark, V denotes the volume of the fluid in between the upper and lower mark. l denotes the length of the capillary. t denotes the time, that the fluid takes to elute the given volume V between the marks. If Δp is only due to height differences it can be equated to $\Delta p = \rho g h$, where ρ is the density of the fluid, g is the acceleration of gravity and h is the height difference between the outlet of the capillary and the middle of the bulb containing the sample volume. Thus the following expression for the kinematic viscosity is obtained:

$$v = \frac{\pi d^4 \rho g h t}{8 V l} \tag{4.3}$$

Equation 4.3 was derived for infinitely long capillaries. Thus, a correction has to be introduced (Hagenbach correction) in order to correct for finite capillary length:

$$v = \frac{\pi d^4 \rho g h t}{8 V l} - \frac{m V}{8 \pi l t} \tag{4.4}$$

Herein m is a dimensionless factor depending on the in- and outlet of the capillary. In order to obtain the kinematic viscosity η, the dynamic viscosity is divided by the density of the fluid $\eta = v/\rho$. All other variables but t in equation 4.3 are constants. They can be combined to a constant K which is specific for a given capillary.

$$\eta = K t \tag{4.5}$$

Thus, in order to obtain η for a given solution, it is simply necessary to measure the time t the solution takes to run through the capillary. Viscosity measurements were performed with 9 different solutions ranging from 0 to 8 M GdnHCl at 23°C. Each solution was measured at least threefold and the corresponding dynamic viscosities were averaged. The data points (see figure 4.7) were fit to equation 4.6.

$$\eta = p_1 + 10^{-3} p_2 c_{\mathrm{GdnHCl}}^{1/2} + 10^{-2} p_3 c_{\mathrm{GdnHCl}} + 10^{-3} p_4 c_{\mathrm{GdnHCl}}^2 + 10^{-3} p_5 c_{\mathrm{GdnHCl}}^3 \qquad (4.6)$$

Equation 4.6 is based on a viscosity model equation in the software Sednterp [61]. All the p_i denote constants which were estimated by non-linear least-square fitting. c_{GdnHCl} is the GdnHCl concentration of the corresponding solution. However, the fit of the experimental data to this model is excellent with an R^2 very close to 1 ($R^2 = 0.9992$). The following parameters were obtained:

Table 4.1: Parameters from the fit of the viscosity data in figure 4.7.

p_1	p_2	p_3	p_4	p_5
1.0103	35.189	0.188	9.429	1.203

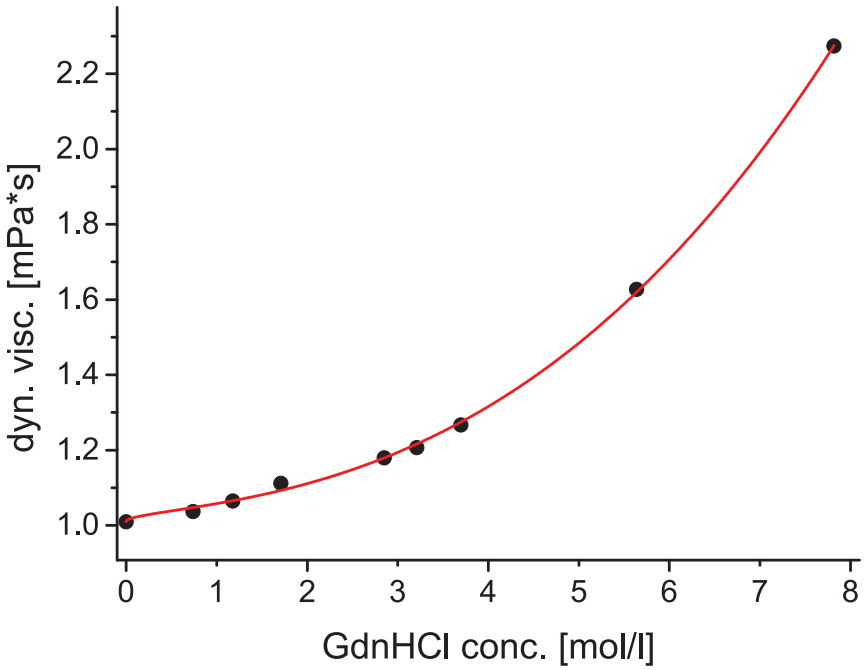

Figure 4.7: Viscosity measurements were performed on 9 different solutions ranging from 0 to 8 M GdnHCl. The data was fitted to an empirical equation 4.6. The viscosities of solutions with GdnHCl concentrations in between the fulcrums were estimated based on this equation.

However, density measurements were performed using a Density meter DMA 5000 (Anton Paar) which is based on the U-tube principle. All density measurements were performed at 23°C.

4.4 Time-resolved fluorescence measurements

Time-resolved fluorescence measurements were performed on a FluoTime 300 fluorescence spectrometer (PicoQuant, Berlin). The spectrometer is equipped with a supercontinuum laser (Solea supercontinuum laser) and a photon counting card (HydraHarp 400, PicoQuant, Berlin). The cuvette holder was tempered to 23°C. The excitation wavelength was set to 485 nm with the excitation bandpass filter set to 1.5 nm. However, the emission bandpass was set to 5.4 nm. For time-resolved fluorescence lifetime measurements, the detection polariser was set to 54.7° (magic angle condition). Under this condition, polarising effects vanish which would otherwise affect the lifetime decay. For time-resolved fluorescence anisotropy measurements, the detection polariser was set to 0° and 90°, respectively. Steady-state anisotropy measurements were performed on the same instrument. The fluorescence decays were subsequently fitted with custom-written MATLAB code. This code was kindly provided by the group of Professor Claus Seidel. The fluorescence lifetime decay was fitted to a biexponential function (see section 2.1.2). For time-resolved fluorescence anisotropy data analysis, the sum and difference curves (see section 2.1.3) were globally fitted, with the lifetimes fixed to the values which had previously been determined in the lifetime analysis.

4.5 Atomic force microscopy measurements

Atomic force microscopy is a powerful technique to perform imaging with high resolution. It is based on the interaction of an ultra-fine tip with atoms of the sample. This tip is part of the cantilever whose bending is monitored with the help of a laser (see figure 4.8). Therefore, the laser is reflected from the surface of the cantilever and subsequently detected by a quadrant detector (array of 4 photodiodes). The bigger the interaction between the tip and the sample surface, the bigger the bending of the cantilever. After calibration, the output signal of the quadrant detector can be used to obtain the vertical deflection of the cantilever (Δz). In this work, we applied AFM measurements were performed in constant force mode (contact mode), i.e. the force between the tip and the sample surface is kept constant while scanning the surface in two dimensions. According to Hooke's law $F = k\Delta z$, where k is the spring constant of the cantilever, this means that the z-direction permanently changes in order to maintain constant force conditions. Thus, it enables to obtain a z-profile over the xy-plane.

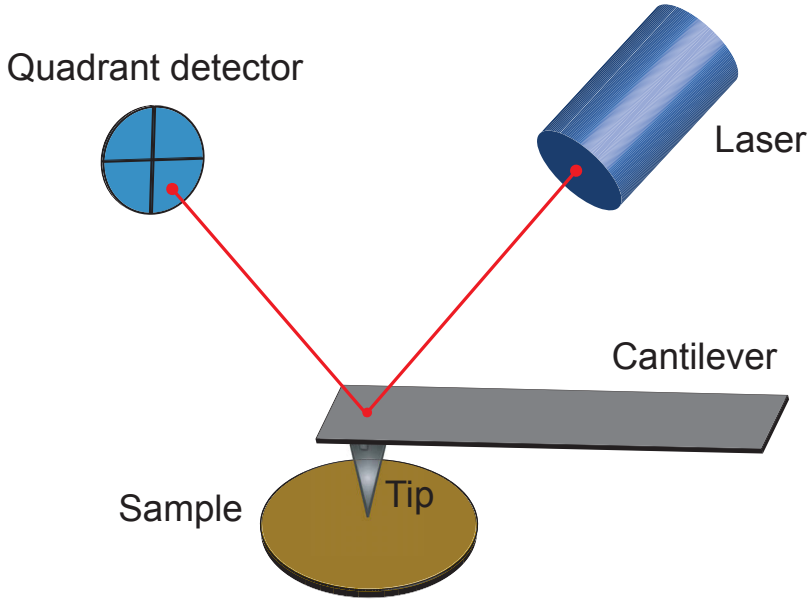

Figure 4.8: Schemtatic representation of an AFM setup. Bending of the cantilever arises due to the interaction of the tip with the sample surface. It is monitored by registering the deflection of a laser beam which is focused onto the cantilever surface and subsequently detected by a quadrant detector.

In this work, a JPK Nanowizard 3 was applied to do the AFM measurements. Samples were incubated on freshly cleaved mica for 30 minutes at 50°C. The mica surface was subsequently rinsed with water (100 μl, 5 times). Generally, a buffer control without the peptide was carried along for all measurments and measured under the same conditions as the actual sample.

4.6 1fFCS unfolding measurements

1fFCS measurements were performed on a home-built confocal fluorescence detection setup (4.9) equipped with a pulsed laser diode (LDH-P-C-470, PicoQuant, Berlin). The laser light is forwarded into the microscope via a polarization maintaining optical fibre and a dichroic mirror (dichroic mirror z470/635, AHF Analysentechnik, Tuebingen). A water immersion objective (UplanApo 60x 1.2 W, Olympus, Melville, NY) focusses the laser beam into the sample solution where fluorescent molecules are excited. Fluorescence light is collected by the same objective in the reverse direction, passing through the dichroic mirror and focussed onto a pinhole of 100 μm diameter using a tube lens. A polarising beam splitter separates photons according to their polarisation. Each beam passes a bandpass filter (BrightLine 520/35, AHF Analysentechnik, Tuebingen) and is subsequently focussed onto a SPAD detector (PDM, MPD, Bolzano). The

detector output signals were fed into a photon counting card (SPC-150, Becker&Hickl, Berlin). For fluorescence correlation spectroscopy (FCS) analysis, the signals from both detectors were cross-correlated to remove detector artifacts such as afterpulsing. FCS measurements were performed in a 389 well-plate (384 Well Greiner Microplate, Greiner Bio-One, Frickenhausen) covered with foil to prevent solvent evaporation. The correction collar was adjusted to gain maximum intensity when measuring a concentrated solution (10 nM) of AF488. A laser power of about 20 μW was chosen to prevent triplet formation and saturation effects. The concentration of AF488C(0)Aβ_{42} was about 3 nmol/l. The correlation and the following fitting was performed using custom software written in MATLAB (The Mathworks, Natick, Massachusetts). A typical 1fFCS measurement contained more than 20 million detection events. This data was subsequently split into subpackages of 2 million events resulting in 10 correlation curves for each GdnHCl concentration. It was subsequently correlated using a custom-written multi-tau algorithm in MATLAB. Each correlation curve was fitted to a single species diffusion model (equation 2.64). For the purpose of calibration, the AF488 diffusion coefficients, needed to be recalculated with regard to the experimental conditions (temperature T and viscosity η).

$$D_T = D_{\text{ref}} \frac{T \eta_{\text{ref}}}{T_{\text{ref}} \eta} \tag{4.7}$$

The reference conditions were $T_{\text{ref}} = 298.15\ K$ and $\eta_{\text{ref}} = 8.90510^{-3}\ mPa \cdot s$, i.e. the conditions at which the diffusion coefficient of AF488 maleimide had previosuly been determined by 2fFCS.

4.7 2fFCS unfolding measurements

2fFCS measurements were performed on a MicroTime 200 (PicoQuant, Berlin) with dual-focus FCS option. Two perpendicular polarised laser beams are fed into a polarisation maintaining fibre and subsequently coupled into the microscope (Olympus IX 71). The setup uses pulsed (triggered) laser diodes in order to assign the emerging photons to their corresponding laser beam. Triggering is performed with laser driver electronics (Sepia II PDL 828, PicoQuant, Berlin). In the microscope, the laser beam is is reflected by a dichroic mirror (z470/532/637rpc, AHF-Analysentechnik, Tuebingen) and forwarded towards a water-immersion objective (UPLSAPO 60xW, 1.2 N.A., Olympus, Melville, NY). A Nomarski prism (U-DICTHC, Olympus, Melville, NY) is placed in front of the objective in order to separate both laser beams according to their polarisation. This leads to two overlapping and laterally shifted laser foci in the focal plane of the objective. The lateral shift is very robust and allows to determine absolute

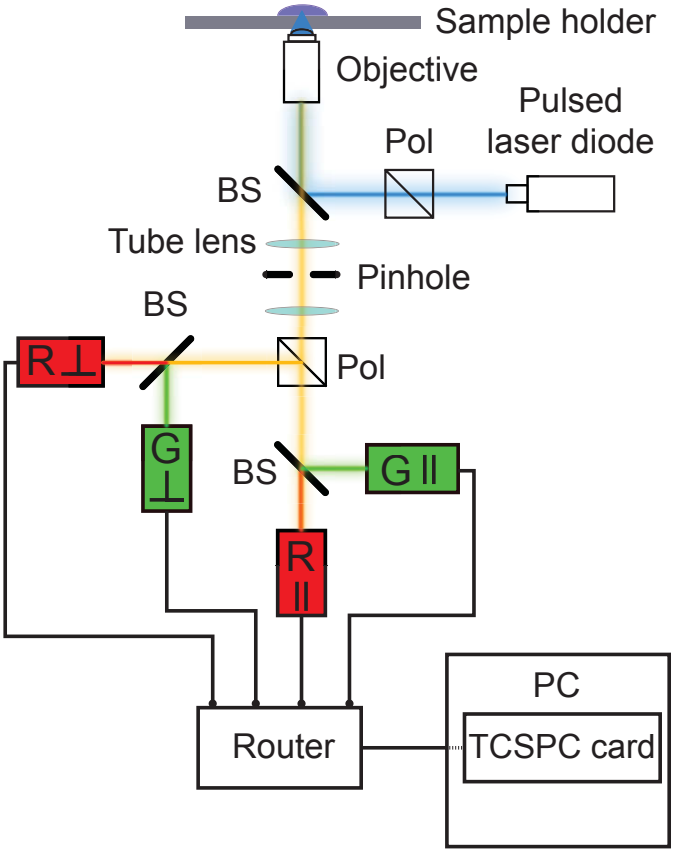

Figure 4.9: Schematic illustration of the single-molecule fluorescence setup used for 1fFCS. Refer to the text for a detailed explanation.

diffusion coefficients [33]. Fluorescence photons are collected by the same objective in the reverse direction. They pass the dichroic mirror and are susbequently focused onto a 75 μm pinhole. Behind the pinhole, photons are equally divided into two beams by a 50 % beam splitter and finally each one is focused onto an avalanche photodiode (Micro Photon Devices, PDM series). Detector output signals are fed into a photon counting card (PicoHarp 300, PicoQuant). For more details about the instrumental setup refer to [62]. The resulting data is correlated and fitted using custom software written in MATLAB. For the correlation, the signals from both detectors are cross-correlated in order to remove detector artifacts such as afterpulsing.

A typical 2fFCS measurement contained more than 20 million detection events. This data was subsequently split into subpackages of 2 million events resulting in 10 correlation curves for each GdnHCl concentration. The resulting correlation curves were fitted to a one-component (see equation 2.70). In this work, 2fFCS measurements were performed in a custom-made sample cell with temperature control. This sample cell was designed in the group of Professor Walter Richtering [63]. The temperature was set to 23°C.

4.8 Simulation of single-molecule fluorescence experiments

This section describes the basics of a procedure on how to simulate single-molecule fluorescence data based on time-correlated single photon counting [64]. These simulations can, for example, be applied in order to test different data analysis strategies. Additionally, comparing experimental results with simulation results can help to identify possible artifacts and their influence on data interpretation.
The data of our TCSPC photon counting card (see figure 4.9) is time-tagged and typically consists of two types of time information, namely micro- and macrotimes (figure 4.10). Microtimes denote the time-lag of an arrival event relative to the proceeding laser pulse. Macrotimes denote the time of an arrival relative to the start of the experiment. While the former can be used to extract fluorescence lifetime information, the latter

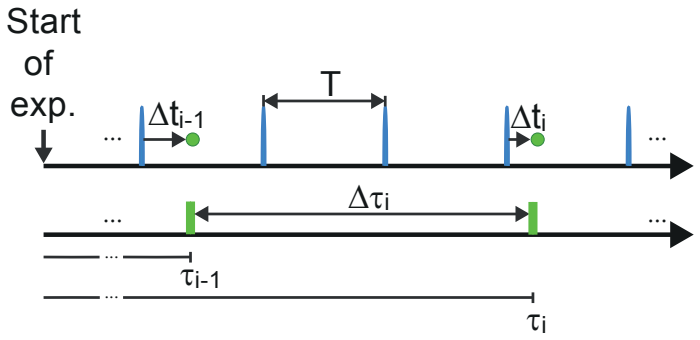

Figure 4.10: Schematic representation of the time-tagged data format as obtained from the photon counting card of our single-molecule fluorescence setup (see figure 4.9). Microtime Δt data contains fluorescence lifetime information. Microtimes are always related to a preceeding laser pulse (blue). However, macrotimes τ monotonically increase from the start of the experiment. The difference of two adjacent macrotimes $\Delta\tau_i - \tau_{i-1}$ denotes the interphoton time.

can be used to extract intensity information. Microtimes can simply be generated by sampling the arrival times Δt from an appropriate distribution. Microtimes for scatter counts, for example, are sampled from the instrument response function (IRF). Those for dark counts are sampled from a uniform distribution. However, fluorescence counts are sampled from a distribution which is given by the convolution of the IRF with the fluorescence decay model, e.g. a monoexponential function (see also section 2.1.2). Simulating macrotimes is more demanding since they need to contain information about diffusional and photophysical processes (such as triplet state). In what follows, we will give a short overview of the simulation system and describe how to simulate macrotimes.
Simulations were done in a box with periodic boundary conditions and whose edge lengths were L_x, L_y, L_z. At time zero N_{box} particles were uniformly distributed over

the box volume $V_{\text{box}} = L_x L_y L_z$. N_{box} is related to the average number of molecules in the effective volume (N_{PSF}, known from fluorescence correlation spectroscopy or photon counting histogram) by the following relation:

$$N_{\text{box}} = \left\lceil \frac{V_{\text{box}}}{V_{\text{PSF}}} N_{\text{PSF}} \right\rceil \tag{4.8}$$

In equation 4.8 $\lceil \dots \rceil$ denotes rounding towards the next integer, V_{PSF} denotes the effective volume. The position r_i for each particle i is given by a three-dimensional vector $r_i = [x_i, y_i, z_i]$. At each time-step Δt a random walk was simulated by adding a normally distributed random number with a mean of zero and a standard deviation equal to $\sqrt{2D\Delta t}$ to r_i. Typically, a time-step of $\Delta t = 10^{-6}$ s was used. The number of photons F_i emitted by a particle i was sampled from a Poisson distribution

$$F_i \sim \text{Poi}(\varepsilon_i \Delta t \text{PSF}(r_i)) \tag{4.9}$$

Herein $\text{PSF}(r_i)$ is given by equation 2.33. ε_i denotes the molecular brightness of particle i. Background counts were also sampled from a Poisson distribution but in contrast to fluorescence photons, background counts do not show any dependence on r. Therefore, they are given by:

$$F_{bg} \sim \text{Poi}(\lambda_{bg} \Delta t) \tag{4.10}$$

Herein λ_{bg} denotes the background countrate (in seconds). The background was simulated as scatter- and dark counts. The j-th macrotime τ_j was generated according to:

$$\tau_j = j \cdot \Delta t \tag{4.11}$$

To include the effect of triplet-state dynamics, i.e. the transition from $S_1 \rightarrow T_1$ and from $T_1 \rightarrow S_1$, a state-vector $\vec{s}$ with entries s_j was generated at each time-step whose number of elements corresponds to the number of particles in the simulation box. The entries of the state vector consist of zeros and ones indicating if the corresponding molecule is available for fluorescence emission ('1') or not ('0'). In other words, an entry in this matrix is zero if the molecule is in the triplet state and one if it is in the first excited singlet state S_1. In order to obtain the mean residence times of the molecules in their corresponding state the following system of differential equations needs to be solved:

$$\begin{bmatrix} \dot{S}_0(t) \\ \dot{S}_1(t) \\ \dot{T}_1(t) \end{bmatrix} = \begin{bmatrix} -k_{exc.} & (k_F + k_{IC}) & k_T \\ k_{exc.} & -(k_F + k_{IC} + k_{ISC}) & 0 \\ 0 & k_{ISC} & -k_T \end{bmatrix} \times \begin{bmatrix} S_0(t) \\ S_1(t) \\ T_1(t) \end{bmatrix} \tag{4.12}$$

with the intitial condition

$$\begin{bmatrix} S_0(t) \\ S_1(t) \\ T_1(t) \end{bmatrix} = \begin{bmatrix} 1 \\ 0 \\ 0 \end{bmatrix} \tag{4.13}$$

The solutions to this differential equation system are given as follows [29]:

$$\begin{aligned} S_0(t) = & \frac{(k_{IC} + k_F)k_T}{k_{exc.}\,(k_{ISC} + k_T) + (k_{IC} + k_F)k_T} + \\ & \frac{k_{exc.}}{k_{exc.} + (k_{IC} + k_F)} \exp\left(-(k_{IC} + k_F + k_{exc.})t\right) + \\ & \frac{k_{exc.}(k_{IC} + k_F)k_{ISC}}{(k_{exc.} + k_{IC} + k_F)\left[k_{exc.}(k_{ISC} + k_T) + (k_{IC} + k_F)k_T\right]} \cdot \\ & \exp\left(-\left[k_T + \frac{k_{exc.}k_{ISC}}{k_{exc.} + k_{IC} + k_F}\right]t\right) \end{aligned} \tag{4.14}$$

$$\begin{aligned} S_1(t) = & \frac{k_{exc.}k_T}{k_{exc.}(k_{ISC} + k_T) + (k_{IC} + k_F)k_T} - \\ & \frac{k_{exc.}}{k_{exc.} + (k_{IC} + k_F)} \exp\left(-(k_{IC} + k_F + k_{exc.})t\right) + \\ & \frac{k_{exc.}^2 k_{ISC}}{(k_{exc.} + k_{IC} + k_F)\left[k_{exc.}(k_{ISC} + k_T) + (k_{IC} + k_F)k_T\right]} \cdot \\ & \exp\left(-\left[k_T + \frac{k_{exc.}k_{ISC}}{k_{exc.} + k_{IC} + k_F}\right]t\right) \end{aligned} \tag{4.15}$$

$$\begin{aligned} T_1(t) = & \frac{k_{exc.}k_{ISC}}{k_{exc.}(k_{ISC} + k_T) + (k_{IC} + k_F)k_T} - \\ & \frac{k_{exc.}k_{ISC}}{k_{exc.}(k_{ISC} + k_T) + k_{IC} + k_F + k_T} \cdot \\ & \exp\left(-\left[k_T + \frac{k_{exc.}k_{ISC}}{k_{exc.} + k_{IC} + k_F}\right]t\right) \end{aligned} \tag{4.16}$$

Equations 4.14 to 4.16 adopt a much more comfortable form if it is taken into account that $k_{exc.}$ is much bigger than all the other rates. Additionally, due to the fact that $k_{exc.}$ is very big (on the order of 10^{15} per second), the second terms in equations 4.14 and 4.15 vanish. Consequently, the last terms in equations 4.14 to 4.16 describe the probability distributions of the times a molecule makes a transition from the corresponding state to one of the others. The residence time of a molecule in state T_1, is exponentially distributed with a mean residence time of $\tau_{T_1} = (k_T + k_{ISC})^{-1}$ [29]. $(k_{ISC} + k_T)^{-1}$ is often referred to as triplet time τ_T (see also section 2.1.4.3). At each time-step Δt the probability that the molecule makes a transition from T_1 to S_0 is given by $P_{T_1 \to S_0} = 1 - \exp(-\Delta t/\tau_{T_1})$. Correspondingly $P_{S_1 \to T_1} = 1 - \exp(-\Delta t/\tau_{S_1})$ is the probability that the molecule makes a transition from S_1 to T_1.
At the beginning of the simulation, a state-vector was generated with, on average, $N_{\text{box}} F_T$ zeros (to indicate molecules in the triplet state) and $1 - N_{\text{box}} F_T$ ones (to indicate molecules in the singulet state S_0). Herein F_T denotes the triplet fraction (see section 2.1.4.3). Subsequently for each molecule i in the triplet state T_1, a random number r_1 (between 0 and 1) is generated. If $r_1 \leq P_{T_1 \to S_0}$, then the molecule would stay in the triplet state and entry i of the state vector was again set to zero. Otherwise it was set to one. Correspondingly, a random number r_2 was assigned to each molecule j which was in the S_0 state. If $r_2 \leq P_{S_1 \to T_1}$, entry j of the state vector was again set to one. Otherwise it was set to zero. As expected, P_{S_1} and P_{T_1} add-up to one. So once the molecule is excited, it must be either found in S_1 or in T_1. The state vector $\vec{s} = [s_1, s_2, \ldots, s_{N_{\text{box}}}]$ is initially populated with zeros and ones according to the probabilities P_{S_1} and P_{T_1}. Using this gives a modified version of equation 4.9:

$$F_i \sim \text{Poi}(s_i \varepsilon_i \Delta t \text{PSF}(r_i)) \tag{4.17}$$

Nevertheless, when including triplet states, the brightness has to be corrected for the triplet fraction F_T:

$$\varepsilon = \varepsilon\,(1 + F_T) \tag{4.18}$$

Simulations were performed with custom software written in MATLAB. Our code made use of MATLAB's parallel computing toolbox to run simulations with different species in parallel and to save computation time.
The reliability of the Brownian dynamics simulations was intensely tested by FCS and PCH analysis of the simulated data. In addition, simulated data was compared to experimental data.

4.9 Development of a Bayesian burst identification method

Performing FFS measurements on highly diluted samples with at maximum one fluorescent molecule in the laser beam at a time, leads to the appearance of bunches of counts in the intensity trace which stand out from the background (see figure 2.2 B). For single-molecule fluorescence spectroscopy, it is of key importance to isolate these fluorescence bursts since they can contain a lot of useful information like diffusion coefficient, brightness and lifetime information. For more details about the analysis of fluorescence photons from bursts I refer to the informative review by Sisamakis *et al.* [9]. Most often fluorescence burst identification is performed using intensity information (see e.g. [10–14]). However, two recently published papers describe a Bayesian burst identification method which is solely based on fluorescence lifetime information [15, 16]. Lifetime information is not always available, especially if the experimental setup lacks TCSPC detection (see e.g. [64]). However, in this section it will be shown how to use both types of information, fluorescence lifetime- and intensity information, to detect fluorescence bursts. Therefore we apply Bayesian model inference (see section 2.3) for given subsets of micro- and interphoton times $D = \{\Delta t_i, \Delta\tau_i\}_{i=1}^{N}$. To decide whether a given subset of data D rather belongs to a fluorescence burst or to background, we use the posterior ratio (see section 2.3):

$$\frac{p(M_{bu}|D)}{p(M_{bg}|D)} = \frac{p(D|M_{bu})p(M_{bu})}{p(D|M_{bg})p(M_{bg})} \tag{4.19}$$

Here I skipped the implicit conditional dependency on background information I (see section 2.3). If equal model priors are applied to the burst and background model, the model comparison breaks down into comparing the marginalised likelihoods $p(D|M_{bu})$ and $p(D|M_{bg})$ (see equation 2.74). It is important to note that in our case, only two different (exclusive) models exist. The data D can either be attributed to a fluorescence burst or to background. To perform the actual burst and background assignment, an appropriate threshold is set to the marginal likelihood ratio $p(D|M_{bu})/p(D|M_{bg})$. This is often referred to as Bayes factor B. If B exceeds this threshold, the corresponding data D is assigned to be part of a fluorecent burst. In this work we used a threshold of 100 [65].

Due to the independence of the N detection events, the overall likelihood function $p(\{\Delta t_i, \Delta\tau_i\}_{i=1}^{N}|\theta, M)$ for a given model M can be expressed as a product of the likelihood function for each event.

$$p(\{\Delta t_i, \Delta\tau_i\}_{i=1}^{N}|\theta, M) = \prod_{i=1}^{N} p(\Delta t_i, \Delta\tau_i|\theta, M) \tag{4.20}$$

Since Δt and $\Delta\tau$ are independent measurement variables, equation 4.20 can be written as follows:

$$p(\{\Delta t_i, \Delta\tau_i\}_{i=1}^N|\theta, M) = \prod_{i=1}^{N} p(\Delta t_i|\theta, M)p(\Delta\tau_i|\theta, M) \tag{4.21}$$

Thus, it is straightforward to calculate the marginal likelihood (see also equation 2.74):

$$\begin{aligned} p(\{t_i, \Delta\tau_i\}_{i=1}^N|M) = \int_{\text{all }\theta} \prod_{i=1}^{N} p(\{t_i\}|\theta, M) \\ \prod_{i=1}^{N} p(\{\Delta\tau_i\}|\theta, M)p(\theta|M)d\theta \end{aligned} \tag{4.22}$$

Hence, appropriate likelihood functions are needed in order to calculate the marginal likelihood and successively calculate the Bayes factor.

4.9.1 Likelihood function for microtimes

Microtimes within a fluorescence burst are assumed to consist of fluorescence photons and a small fraction of scatter (γ_{sc}) and dark counts (γ_{dc}), respectively. Microtimes of fluorescence photons follow a fluorescence decay model (see equation 2.8). However, microtimes of scatter events are distributed according to the (normalised) instrument response function and microtimes of dark count events are distributed according to a uniform distribution. Since microtimes are counted in discrete time channels, the corresponding likelihood function for the burst model is a function of the channel number $j = 1 \ldots M$:

$$\begin{aligned} p(\Delta t_j|\theta_{bu}, M_{bu}) = (1 - (\gamma_{sc} + \gamma_{dc}))\, \frac{p_{dec}(\Delta t_j)}{\sum_{j=1}^{M} p_{dec}(\Delta t_j)} + \\ \gamma_{sc}\frac{\mathrm{IRF}(\Delta t_j)}{\sum_{j=1}^{M} \mathrm{IRF}(\Delta t_j)} + \gamma_{dc}\frac{1}{M} \end{aligned} \tag{4.23}$$

Herein γ_{sc} and γ_{dc} denote the fraction of scatter and dark count events in a burst. $p_{dec}(\Delta t_j)/\sum_{j=1}^{M} p_{dec}(\Delta t_j)$ denotes the probability of finding a fluorescent count in channel j. It is the normalised result of the convolution of the fluorescence decay model with the instrument response function (IRF) (see section 2.1.2 for more details). In this work, we used a monoexponential function as fluorescence decay model, although in some cases a multiexponential function might be more adequate. $\mathrm{IRF}(\Delta t_j)/\sum_{j=1}^{M} \mathrm{IRF}(\Delta t_j)$

and $1/M$ denote the probability of finding a scatter- and dark count in channel j. The likelihood function for the background model is then simply given by equation:

$$p(\Delta t_j|\theta_{bg}, M_{bg}) = (1-\alpha_{dc})\,\frac{\mathrm{IRF}(\Delta t_j)}{\sum_{j=1}^{M}\mathrm{IRF}(\Delta t_j)} + \frac{\alpha_{dc}}{M} \tag{4.24}$$

Herein α_{dc} denotes the fraction of dark counts within a given set of background counts. Correspondingly, $\alpha_{sc} = (1-\alpha_{dc})$ denotes the fraction of scatter. Both are not to be confused with γ_{dc} and γ_{sc}, respectively. Nevertheless, these parameters are connected by the following relation:

$$\alpha_{dc}\gamma_{bg} = \gamma_{dc} \tag{4.25}$$

$$\alpha_{sc}\gamma_{bg} = \gamma_{sc} \tag{4.26}$$

α_{dc} and α_{sc} can be easily obtained by measuring the solvent without a fluorescent sample.

4.9.2 Likelihood function for interphoton times

A probability function for interphoton times was derived by Gopich and Szabo [66]. I will shortly recapitulate their main results concerning the intephoton time distribution. Gopich and Szabo showed that the interphoton time distribution for diffusing fluorophores (with diffusion constant D and brightness ε) can be obtained by solving the following reaction diffusion equation:

$$\frac{\partial g}{\partial t} = D\nabla^2 g - \varepsilon(r)g \tag{4.27}$$

with intitial condition $g(r, t=0) = 1$. After further calculation (see e.g. [66, 67] for details), the interphoton time distribution can be calculated as follows:

$$\phi(\Delta\tau) = \frac{1}{\bar{n}}\left(-\frac{dk(\Delta\tau)}{d\Delta\tau} + ck(\Delta\tau)^2\right)\exp\left(-c\int_0^{\Delta\tau} k(\Delta\tau)dt\right) \tag{4.28}$$

Herein $k(\Delta\tau)$ is related to the solution g of the reaction diffusion equation 4.27 by:

$$k(t) = \int_r \varepsilon(r)g(r,t)dr \tag{4.29}$$

$\bar{n}$ in equation 4.28 denotes the average brightness[1]. c denotes the fluorophore concentration (per observation volume). However, we can rewrite equation 4.28 and obtain:

$$\phi(\Delta\tau) = \frac{1}{c\bar{n}} \left(-c\frac{dk(\Delta\tau)}{d\Delta\tau} + c^2 k(\Delta\tau)^2 \right) \exp\left(-c\int_0^{\Delta\tau} k(\Delta\tau)dt \right) \tag{4.30}$$

We include background (with countrate n_{bg}) as follows:

$$\phi(\Delta\tau) = \frac{1}{c\bar{n} + n_{bg}} \left(-c\frac{dk(\Delta\tau)}{d\Delta\tau} + (ck(\Delta\tau) + n_{bg})^2 \right) \exp\left(-c\int_0^{\Delta\tau} k(\Delta\tau)dt - n_{bg}\Delta\tau \right) \tag{4.31}$$

Equation 4.31 is the interphoton time distribution for one fluorescent species including background contributions. It can be generalised to M different species according to the following equation:

$$\begin{aligned} \phi(\Delta\tau) = & \frac{1}{\sum_{j=1}^{M} c_j\bar{n}_j + n_{bg}} \left(-\sum_{j=1}^{M} c_j \frac{dk_j(\Delta\tau)}{d\Delta\tau} + \left(\sum_{j=1}^{M} c_j k_j(\Delta\tau) + n_{bg} \right)^2 \right) \cdot \\ & \exp\left(-\sum_{j=1}^{M} c_j \int_0^{\Delta\tau} k_j(\Delta\tau)dt - n_{bg}\Delta\tau \right) \end{aligned} \tag{4.32}$$

The reaction-diffusion equation (4.27) can only be solved analytically for a step-volume profile. However, in case of a Gaussian PSF this task has to be done numerically. In this work, we used the discretisation scheme in spherical coordinates proposed in paper [68]. Briefly, the space coordinate r was discretised according to a non-linear discretisation scheme:

$$r(i) = \begin{cases} (i-0.5)\Delta, & i \le N_{in} \\ (i-0.5)\Delta + (R_{out} - N\Delta)\left(\frac{i-N_{in}-0.5}{N_{out}}\right)^2, & N_{in}+1 \le i \le N_{in}+N_{out} \end{cases} \tag{4.33}$$

Herein R_{out} denotes the outer boundary. N_{in} and N_{out} denote the number of grid nodes inside- and outside the observation volume (with radius b), respectively. N is stands for the total number of grid points. Correspondingly, $\Delta = b/N_{in}$ is the step-size inside the observation volume. Applying the discretisation in equation 4.33 to equation 4.27 one gets the following (discretised) reaction diffusion equation:

[1]Brightness is generally defined as the intensity of a molecule at the center of the PSF.

$$\frac{\partial \boldsymbol{g}}{\partial \boldsymbol{t}} = (\boldsymbol{L} - \boldsymbol{\varepsilon})\boldsymbol{g} \tag{4.34}$$

$\boldsymbol{\varepsilon}$ is an $N \times N$ diagonal matrix with elements $\varepsilon(r_i)$ on the diagonal. $\boldsymbol{L}$ is the discretised Laplacian with elements $L_{ii} = -(l_i^+ + l_i^-)$ and $L_{ii\pm1} = l_i^\pm$ for all $1 < i < N$ on the main- and minor diagonal, respectively. However L_{11} and L_{NN} are different, namely $L_{11} = -l_1^+$ and $L_{NN} = -l_N^-$. Herein $l_i^\pm$ is given as follows:

$$l_i^\pm = \frac{4\pi D \left[r(i \pm 0.5)\right]^2}{v_i s(i \pm 0.5)} \tag{4.35}$$

where $s(i) = dr(i)/di$ denotes the step-size of the nodes and v_i denotes the volume of the i-th layer. v_i is given as follows:

$$v_i = 4\pi/3 \left(\left[r(i + 0.5)\right]^3 - \left[r(i - 0.5)\right]^3 \right) \tag{4.36}$$

Using this discretisation scheme one can solve for $k(\Delta\tau)$ (see equation 4.29):

$$k(\Delta\tau) = \mathbf{1}^T \boldsymbol{\varepsilon} \exp\left((\boldsymbol{L} - \boldsymbol{\varepsilon})\Delta\tau\right) \mathbf{1} \tag{4.37}$$

where $\exp\left((\boldsymbol{L} - \boldsymbol{\varepsilon})\Delta\tau\right) \mathbf{1}$ is the (matrix exponential) solution to the discretised reaction diffusion equation (4.34) including the initial condition. The matrix $(\boldsymbol{L} - \boldsymbol{\varepsilon})$ can be diagonalised:

$$(\boldsymbol{L} - \boldsymbol{\varepsilon}) = \boldsymbol{A} \mathrm{diag}\left(-\lambda_j\right) \boldsymbol{A}^{-1} \tag{4.38}$$

where $\mathrm{diag}\left(-\lambda_j\right)$ denotes a diagonal matrix of positive eigenvalues of $(\boldsymbol{L} - \boldsymbol{\varepsilon})$. The columns of $\boldsymbol{A}$ are the corresponding eigenvectors of $\mathrm{diag}\left(-\lambda_j\right)$. If the expression in equation 4.38 is used in equation 4.37 one gets[2]:

$$\begin{aligned} k(\Delta\tau) =& \mathbf{1}^T \boldsymbol{\varepsilon} \boldsymbol{A} \mathrm{diag}\left(\exp\left(-\lambda_j \Delta\tau\right)\right) \mathbf{1} \\ =& \sum_j a_j b_j \exp\left(-\lambda_j \Delta\tau\right) \end{aligned} \tag{4.39}$$

where $a_j = \sum_j \boldsymbol{V}_{ii} \boldsymbol{A}_{ij}$ and $b_j = \sum_j \boldsymbol{A}^{-1}_{ji}$. In order to get $dk(\Delta\tau)/d\Delta\tau$ we simply have to take the derivative of equation 4.39 with respect to $\Delta\tau$ which can be done analytically.

We tested the reliability of the discretisation scheme on simulated data using the

[2]Special thanks to Irina Gopich for pointing out these aspects!

raw interphoton times as input for a maximum likelihood estimator. The estimated values for D, c and ε were in excellent agreement to the simulated ones and thus the corresponding theoretical $\phi(\Delta\tau)$ closely fitted the experimental interphoton time distribution (see figure 4.11). It is interesting to note that this method of fitting the

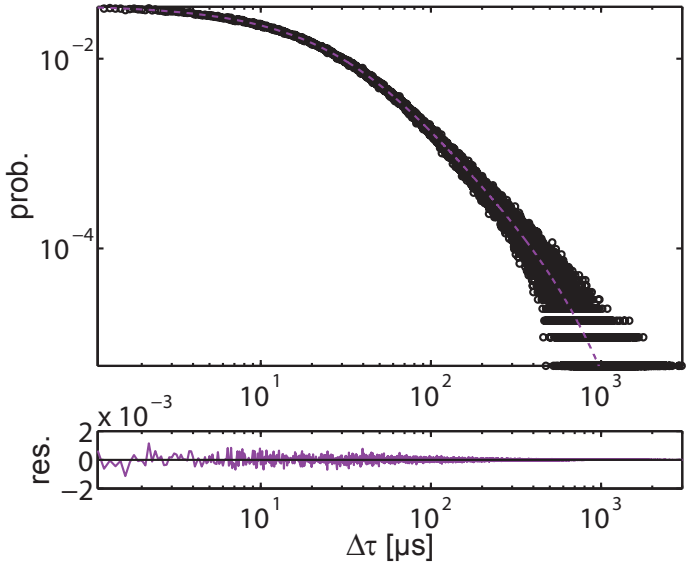

Figure 4.11: Interphoton time distribution from simulated data (∘) with the corresponding theoretical fit (dashed line). The residuals in the lower subplot show that the theoretical fit matches the interphoton time distribution of the simulated data. The following parameters were used in the simulation: $\varepsilon = 50$ kHz, $D = 200\ \mu m^2/s$, $c = 2.81$, $n_{bg} = 0.21$ kHz. The following values were recovered from the fit: $\varepsilon = 50 \pm 0.1$ kHz, $D = 200 \pm 2\ \mu m^2/s$, $c = 2.803 \pm 0.01$.

interphoton time distribution delivers diffusion and brightness information at the same time. Thus, it combines information of FCS and PCH analysis. However, at the moment it is just implemented for an isotropic Gaussian observation volume. We will extend this to other observation volume profiles including the anisotropic Gaussian. Furthermore, we will extend this concept to include blinking effects and to deal with common artifacts like afterpulsing. Discriminating between one or two different species could be done by using Bayesian model comparison (see section 2.3). However, this will be tested in more detail in a future project. It shall be emphasised, that estimating parameters from the interphoton time distribution does not require any binning. The parameter estimation is directly performed with the raw data and correspondingly a bin-correction is not necessary (see e.g. section 2.1.4.1 for bin-correction).
So far all derivations for the interphoton-time distribution $\phi(\Delta\tau)$ were done for the burst model $M = M_{bu}$. $\phi(\Delta\tau)$ in equation 4.31 is what is called the likelihood of interphoton times for the burst model and is denoted with $p(\Delta\tau|\theta, M_{bu})$. The likelihood for background can only be obtained from equation 4.32 by setting all c's equal to zero:

$$p(\Delta\tau|\theta, M_{bg}) = n_{ng} \exp\left(-n_{bg}\Delta\tau\right) \tag{4.40}$$

Hence, interphoton times of background counts are exponentially distributed with rate n_{bg}. This is what is actually expected given that the background counts are Poissonian distributed.

4.9.3 Performance evaluation

The burst detection process can be considered as a binary classification problem. The algorithm assigns a dataset either to the burst- or the background class. Thus, in order to judge the classification performance of our algorithm we calculate the precision and recall which are commonly used to assess the performance of a classifier. From that, we calculate the so-called F-score which is simply the harmonic mean of the precision and recall. All three are calculated as follows:

$$\text{precision} = \frac{\text{num. of true positives}}{\text{num. of true positives} + \text{num. of false positives}} \tag{4.41}$$

$$\text{recall} = \frac{\text{num. of true positives}}{\text{num. of true positives} + \text{num. of false negatives}} \tag{4.42}$$

$$\text{F-score} = 2\frac{\text{precision} \cdot \text{recall}}{\text{precision} + \text{recall}} \tag{4.43}$$

Explained in terms of our burst identification problem, recall denotes the number of correctly identified bursts over the total number of bursts in the dataset. Precision denotes the number of correctly identified bursts over the total number of identified bursts (including falsely identified bursts).
To test the reliability of the new burst identification method we performed a simulation with the parameter set listed in table 4.2. These are typical parameters which were inspired by experimental data of AF488 in buffer, except for the axis ratio $k = \omega_z/\omega_{xy}$ of the laser beam (see equation 2.33). Herein T_{sim} denotes the total simulation time. N denotes the average number of particles in the observation volume. τ_F denotes the fluorescence lifetime. T is the length of the microtime window (see figure 4.10). Q and n_{bg} denote the molecular brightness and background rate, respectively. The corresponding raw data of the simulations was subsequently analysed in terms of a sliding macrotime window approach which was used to extract the portion of data to be analyzed [15].

Table 4.2: Parameter set used for the simulation of single-molecule fluorescence experiments in order to test the relibility of the Bayesian burst identification method. In this case the background solely consisted of scatter events.

Parameter	value
T_{sim}	100 s
T	25 ns
τ_F	4 ns
ω_{xy}	0.5 μm
k	1
N	0.01
Q	100 kHz
D	400 μm^2/s
n_{bg} (scatter only)	1 kHz

5

Bayesian burst identification

Contents

5.1 Reliability of the simulations 66

5.1.1 Influence of the simulation box size 66

5.1.2 Comparison of simulation and experiment 67

5.2 Performance of the Bayesian burst identification method 68

5.2.1 Analysis of simulated data 68

5.2.2 Analysis of experimental data 69

5.1 Reliability of the simulations

5.1.1 Influence of the simulation box size

In order to test the influence of the simulation box size we set the edge lengths to multiples m of the laser beam parameters ω_{xy} and ω_z (see equation 2.33), i.e. $L_x = L_y = m\omega_{xy}$ and $L_z = m\omega_z$. We ran 5 different simulations with m-values ranging from 5 to 30. From the resulting raw data we calculated the autocorrelation curves which were subsequently fitted to a one-component diffusion model (see equation 2.64) with N and τ_{diff} as variable parameters. The corresponding results are listed in table 5.1. As can be seen, both the N and τ_{diff} converge towards the true values ($N = 1$,

Table 5.1: Influence of the simulation box size on the reliability of the FCS analysis parameters N and τ_{diff}. The simulation time was 100 seconds with $\approx 10^8$ detection events and a S/N-ratio of 200:1.

m	box vol. [fl]	observation vol. [fl]	N	$\lvert\Delta N\rvert$ [%]	τ_{diff} [μs]	$\lvert\Delta\tau_{\text{diff}}\rvert$ [%]
5	56.95	2.54	1.04	3.8	223.27	11.8
10	455.63	2.54	1.02	1.82	247.46	2.24
20	3645	2.54	1.01	1.26	254.7	0.62
30	12301.88	2.54	1.01	0.97	253.11	0.01

$\tau_{\text{diff}} = 253.13\ \mu s$) with increasing box size. The correlation curve for $m = 5$ shows some unwanted correlations for higher τ values (see figure A.2). This might be due to the fact that we use periodic boundary conditions. Since molecules which are about to leave the simulation volume in the following step, appear on the opposite side of the cube and can thus be re-excited again although in a real experiment it would have left the region completely. There is no big decrease in the relative deviations in ΔN and $\Delta\tau_{\text{diff}}$ when going from $m = 20$ to $m = 30$. However, the time which is needed to run the simulation increases tremendously with m. Therefore, we decided to run all the subsequent simulations with an m-value of 20.
We also tested our procedure for its capability to reliably simulate triplet state dynamics. The FCS parameters extracted from simulated data were in excellent agreement with the parameters set for the simulation (see figure 5.1).

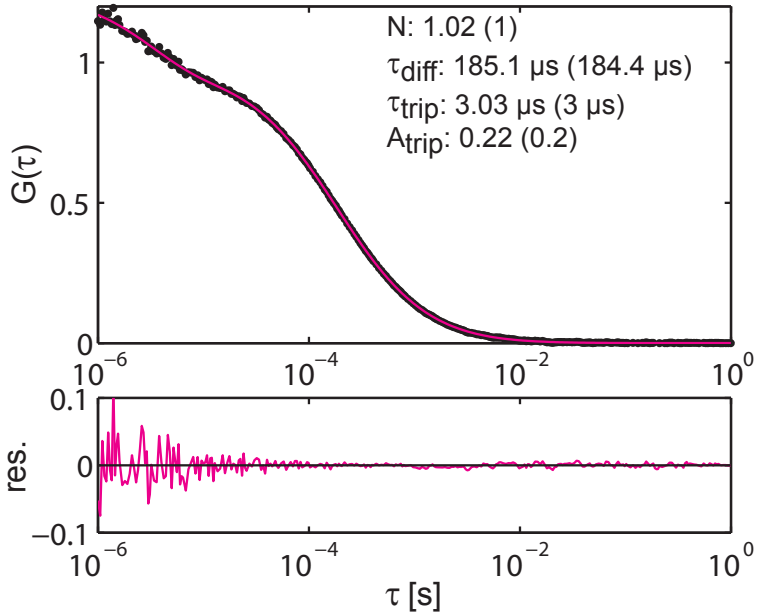

Figure 5.1: Correlation curve of simulated data including triplet state dynamics. The upper subplot depicts the correlation curve (●) with a best fit line (magenta line) to equation 2.65. The subplot at the bottom depicts the corresponding residuals. Fit parameters and the corresponding simulated values (in brackets) are given in the upper subplot.

5.1.2 Comparison of simulation and experiment

Simulations shall enable us to resimulate experimental data. In order to test if our procedure is able to reliably do so, we ran simulations with parameters extracted from experimental data (amount of background, number of molecules in the effective volume, brightness of the molecule, diffusion time, laser beam parameters, etc.). We explored the simulated data using FCS- and PCH analysis. Corresponding results are illustrated in figure 5.2. While the correlation curves do not show any big difference, the PCH show deviations at higher photon counts. This can mainly be attributed to the fact that the experimental PCH is blurred by out-of-focus emission while the simulated data does not contain any out-of-focus emission. We are going to implement the out-of-focus emission in our code in near future. However, we performed some more tests to confirm the reliability of the simulation including simulations of binary mixtures of different species, but also single-molecule data with subsequent burst analysis (data not shown). Taken together, our simulation procedure is able to reliably reproduce experimental data.

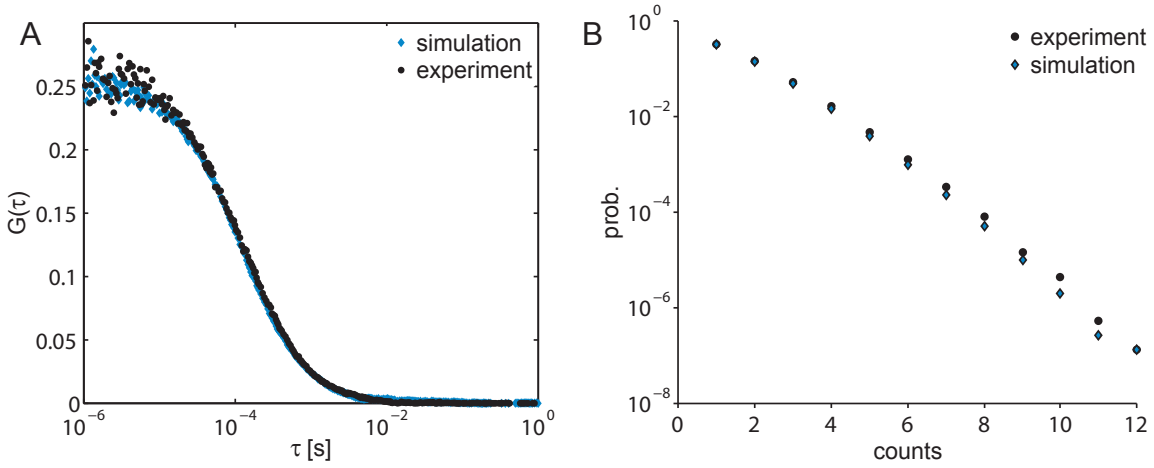

Figure 5.2: Comparison of experiment and simulation. (**A**) Correlation curve of AF488 maleimide in buffered solution (•) and the correlation of the corresponding simulation (◇). (**B**) PCH of AF488 maleimide in buffered solution (•) and the PCH of the corresponding simulation (◇). There are deviations between experimental and simulated PCH at higher photon counts which can be attributed to the out-of-focus emission in case of the experimental PCH.

5.2 Performance of the Bayesian burst identification method

Subsequently I will use the following designations: BBID($\Delta\tau$) denotes the Bayesian burst identification method solely based on interphoton times. BBID(Δt) denotes the Bayesian burst identification method solely based on microtimes. And finally BBID($\Delta\tau, \Delta t$) denotes the Bayesian burst identification method based on both types of time information.

5.2.1 Analysis of simulated data

In order to check the reliability of the BBID($\Delta\tau, \Delta t$), and to compare it to the BBID($\Delta\tau$) and BBID(Δt), respectively, we performed three independent simulations and subsequently analysed the data with these three methods. The corresponding results are summarised in figure 5.3. It is interesting to note that the BBID($\Delta\tau$) (denoted with $\Delta\tau$ in figure 5.3) has maximum precision. It means that all bursts which are identified are indeed true bursts. However on the other hand, the recall is far below 1, namely 0.65, which means that although all bursts are true burst, it only detects 65 % of all true bursts in the data set. Most of the identified bursts contain a moderate to high number of counts. This might explain the high precision

of this method. For the BBID(Δt) it is the other way around. Here, the recall is at maximum while the precision is at 86 %. This means the method not only found all true bursts, but it also found bursts which were not true bursts. The same applies to the BBID($\Delta\tau, \Delta t$). However, the precision is about 4 % higher than for the BBID(Δt). The latter two methods even identified burst which contained a low number of counts. If the importance of precision and recall for burst detection is equally weighted, the F-score (see equation 4.43) can be used to judge the three analysis methods. Correspondingly, the Bayesian method based on interphoton- and microtimes performs best, followed by the method solely based on microtimes. One question that needs to be asked, however, is whether the Laplace approximation for the evidence is an adequate approximation. This is especially of importance for potential bursts with a low number of detection events since the Laplace approximation for the evidence converges to the true evidence for many data points [65]. We recently tested a nested sampling algorithm to compute the model evidence [69]. This method applies a Monte-Carlo approach to calculate the marginalised likelihood (equation 2.74) and should give accurate estimates for the true evidence. Additionally, due to its sampling power, it did not give any hint to the presence of more than one mode of the posterior probability which is another argument in favour of the Laplace approximation. The nested sampling algorithm is very time-consuming and thus not practical for everyday use (at the moment). Nevertheless, in near future we will compare the evidence from the Laplace approximation and the nested sampler in order to check the accuracy of the former one.
Another question which may arise is to what extend the Bayesian burst analysis method depends on the width of the instrument response function (IRF), the fluorescence lifetime or on the scatter-to-dark count-ratio. A big IRF width, for example, combined with a short lifetime, will likely lower the reliability of the lifetime-based Bayesian burst identification.
Furthermore, it would be fruitful to check the influence of different priors on the classification performance. Another flat prior (besides the uniform prior which was applied here), the Jeffrey's prior [65], could be tested and compared to the uniform prior.

5.2.2 Analysis of experimental data

The Bayesian burst identification method was additionally applied to experimental single-molecule fluorescence data of AF488 (TFP-ester) in water (see figure 5.4). The raw data was analysed with the BBID($\Delta\tau, \Delta t$), BBID(Δt) and BBID($\Delta\tau$). For the sake of illustration, the intensity trace is displayed in figure 5.4 A together with the indentified bursts (diamonds). Based on the raw data, the BBID estimates parameters

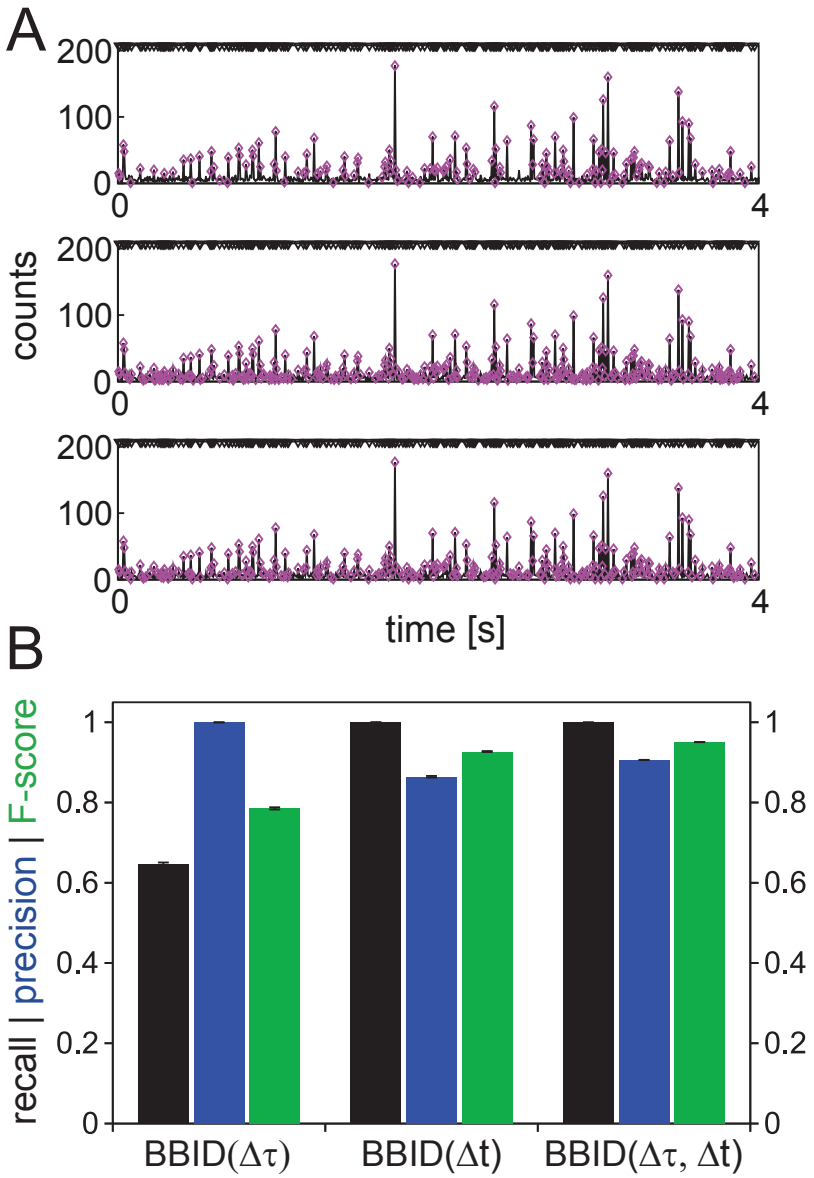

Figure 5.3: (**A**). Intensity traces of simulated data analysed with BBID($\Delta\tau$) (top), with BBID(Δt) (middle) and BBID($\Delta\tau, \Delta t$) (bottom). The corresponding identified bursts are highlighted ($\diamond$). True bursts are depicted as black triangles ($\triangledown$). (**B**) Comparison of the classification performance of the different Bayesian burst identification methods using recall, precision and F-score. Errorbars denote the standard deviation of these three parameters from three independent simulation runs.

such as brightness, number of molecules and fluorescence lifetime for every single burst. The corresponding parameter histograms are displayed in 5.4 B. Figure 5.4 A

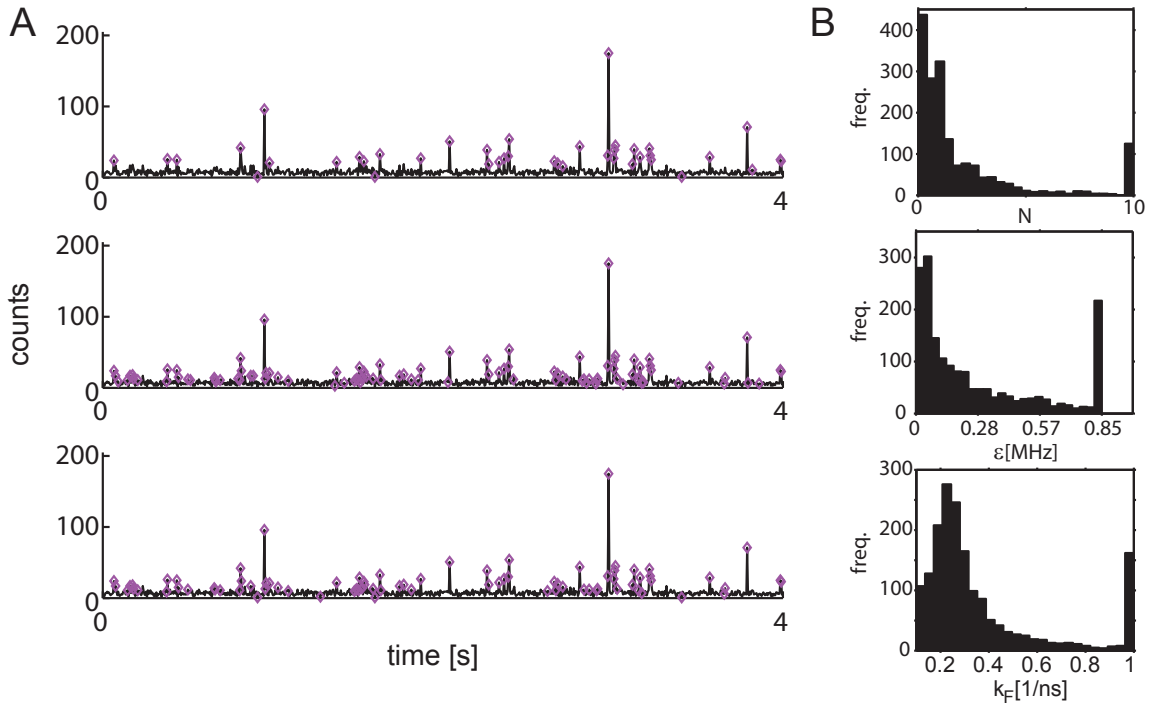

Figure 5.4: (**A**) Three identical intensity traces of AF488 in water (solid black line) with detected bursts (◇) which were identified with the Bayesian burst identification method solely based on interphoton times (top), microtimes (middle) and on both types of time information (bottom). The binning of the intensity traces was set to 5 ms. (**B**) Estimated parameters of the Bayesian burst identification based on both types of time information (see **A**, bottom). The top histogram displays the distribution of the number of molecules in the observation volume for a burst. The middle histogram displays the brightness of the molecule which traversed the observation volume. The bottom histogram displays the distribution of the fluorescence rate $k_F = 1/\tau_F$. Herein τ_F denotes the fluorescence lifetime.

is very informative since it confirms the finding that the BBID($\Delta\tau$) mostly identifies bursts of high intensity (see also section 5.2.1). However, the two other methods additionally identify low intensity bursts as was already found for the simulated data. The parameters that were estimated by the Bayesian burst identification method based both types of timing information are displayed in figure 5.4 B. It shall be noted that the outer bars in all the histograms correspond to values which did not converge in the fitting procedure (due to low counts). The principle course of the brightness is similar to the N histogram. However, neither the N-histogram nor the ε-histogram show distinct peaks in contrast to the k_F-histogram (figure 5.4 B bottom), the histogram of the fluorescence rate ($k_F = 1/\tau_F$). The k_F-histogram peaks at about 0.25 ns^{-1} which corresponds to a fluorescence lifetime of 4 ns. This is in very close agreement with the 4.1 ns of AF488 in PBS [70]. It shall be emphasised, that the histograms arose from the analysis of a 100 s experiment and that no threshold was applied on the

minimum number of events in a burst. Hence, the histogram contains a lot of low count bursts which might lead to the absence of two distinct peaks in the upper histograms. It might be worth trying to extend the measurement time and then to isolate only moderate to high count burst to check this. As can further be seen in figure 5.4, a histogram for the diffusion coefficient is missing. This is because a reliable estimate for the diffusion coefficient with low photon counts (at maximum a few hundreds) is not possible. Additionally, information on diffusion is mostly contained in the time between different bursts and this, however, is not contained within a burst.
Taken together, the Bayesian burst identification is applicable to experimental data. It gives a reasonable fluorescence lifetime estimate even for low numbers of detection events. Burst identification based on interphoton times is not as powerful as burst detection based on microtimes or both time information since it has a lower burst recognition rate.
It shall be noted, that the BBID is still in its infancy. Extending the BBID to arbitrary complex multiparameter fluorescence detection systems should be straightforward using Bayes theorem. One could, for instance, include polarisation or colour information for the BBID. Therefore the likelihood models for both, burst and background model would have to be adapted. However, this will be in the scope of future work.

6

$A\beta_{42}$ MONOMER UNFOLDING

Contents

6.1 Characterisation of AF488-C(0)Aβ_{42} 74

6.1.1 Aggregation propensity 74

6.1.2 Behaviour of the fluorescent dye bound to C(0)Aβ_{42} 75

6.2 Adsorption artifacts in FFS 81

6.3 Refractive index mismatch in 1fFCS measurements 83

6.4 Aβ_{42} is monomeric under FCS measurement conditions . 87

6.5 AF488-C(0)Aβ_{42} monomer unfolding with GdnHCl 88

6.1 Characterisation of AF488-C(0)Aβ$_{42}$

6.1.1 Aggregation propensity

The changes which are necessary to make Aβ$_{42}$ detectable by fluorescence methods might also influence its structure and behaviour. The ability to aggregate into oligomers and fibrils is one of the key features of this peptide. Hence, we tested the aggregation propensity of AF488-C(0)Aβ$_{42}$ solutions using atomic force microscopy (AFM). In addition, we tested a mixture of labeled and non-labeled Aβ$_{42}$ using fluorescence correlation spectroscopy (FCS) and fluorescence anisotropy in order to prove that labeled Aβ$_{42}$ binds to non-labeled Aβ$_{42}$. A recent study by Stine showed that Aβ forms many fibrils in 10 mM hydrochloric acid [71]. Similar conditions were applied in order to obtain fibrils of AF488-C(0)Aβ$_{42}$ (see figure 6.1). Figure 6.1 A shows a whole network of fibrils for AF488 labeled C(0)Aβ$_{42}$, indicating that the dye label and the addional cysteine at the N-terminus do not impede fibril formation.

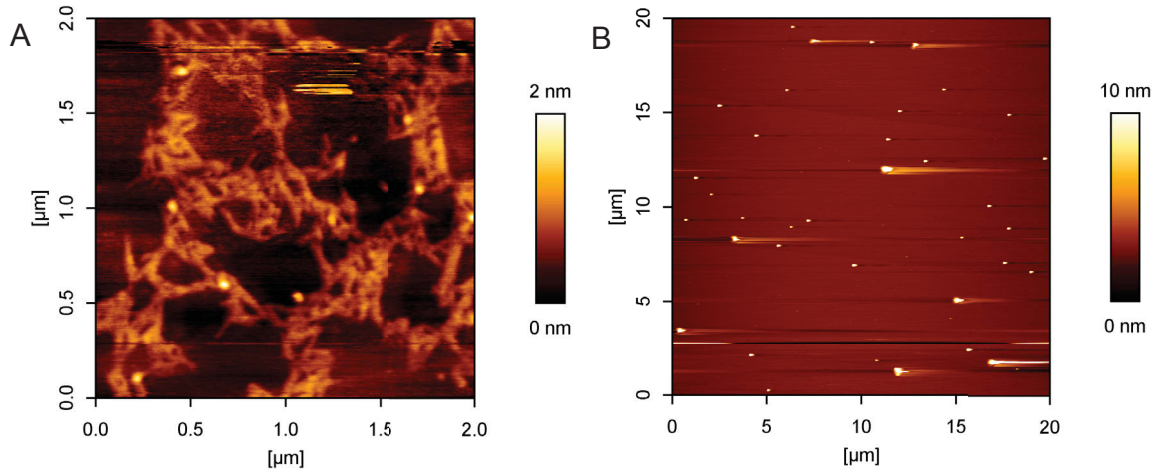

Figure 6.1: (**A**) AFM image of fibrillar clusters of AF488-C(0)Aβ$_{42}$ adsorbed on mica. (**B**) Buffer control without AF488-C(0)Aβ$_{42}$ which was treated exactly the same way as the sample. AFM measurments were performed in tapping-mode.

This suggests that AF488-C(0)Aβ$_{42}$ molecules aggregate among each other. In order to show that it does also aggregate with non-labeled Aβ$_{42}$, we followed aggregation of a mixture of labeled and non-labeled Aβ$_{42}$ (1 nM AF488-C(0)Aβ$_{42}$ mixed with 40 μM Aβ$_{42}$) with fluorescence correlation spectroscopy (FCS) and fluorescence anisotropy. Over time the correlation curves successively shifted to the right indicating an increasing amount of bigger particles. The amount of bigger particles only seemed to overwhelm

the amount of smaller particles. This is due to the fact that bigger particles have a bigger brightness and thus contribute more photons than smaller ones.

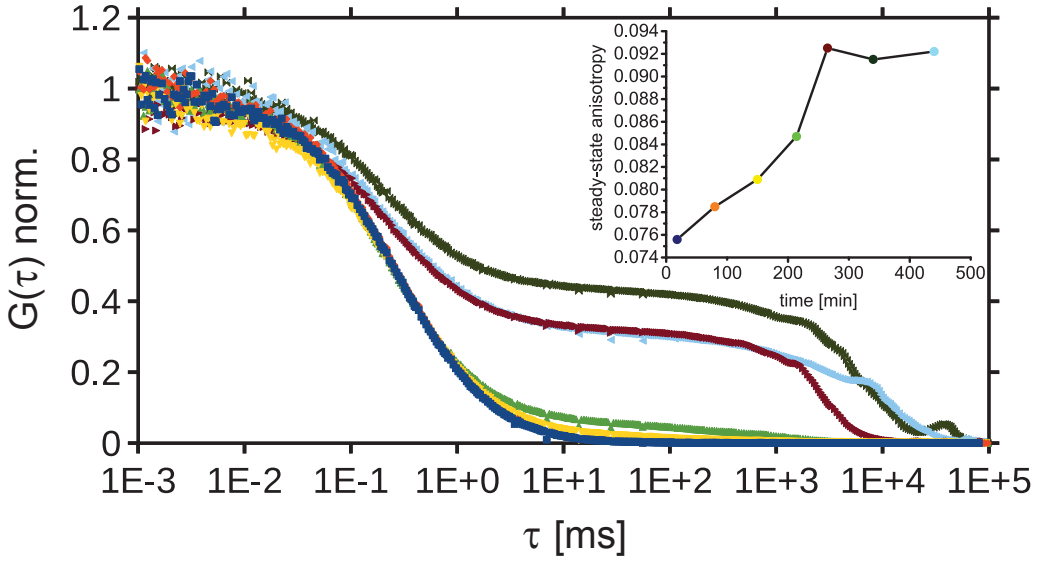

Figure 6.2: Time course measurment of the aggregation of AF488-C(0)Aβ$_{42}$ (1 nM) mixed with non-labeled Aβ$_{42}$ (40 μM) and measured by FCS and fluorescence anisotropy (inset).

Taken together, the AF488 labeled C(0)Aβ$_{42}$ is able to form fibrillar structures and also binds to non-labeled Aβ$_{42}$. It shall be noted that proving the aggregation propensity of dye labeled C(0)Aβ$_{42}$ can be regarded as a hint that the influence of the dye on the Aβ$_{42}$ monomer strucutre is small. However, even if the aggregation propensity would have been lost after coupling the dye to the peptide, it does not mean that the dye influences the C(0)Aβ$_{42}$ monomer structure. It could mean that neighbouring dyes in oligomers influence each other (e.g. repulse each other) which could subsequently lead to a dissociation of the oligomer. Thus, no stable oligomers would ever be formed. Since common structural studies (CD, NMR, etc.) are not applicable to Aβ$_{42}$, MD simulations could help to explore the influence of the dye on the monomer structure [72].

6.1.2 Behaviour of the fluorescent dye bound to C(0)Aβ$_{42}$

In order to consistenly interpret FFS measurement data, as well as to optimise FFS measurement condtions, we applied several ensemble fluorescence methods to characterise the behaviour of the fluorescent dye. E.g. knowing the fluorescence quantum yield can help to interpret brightness analysis methods (see section 2.1.4). Excitation spectra can give information about the local chemical environment of the

dye. However, time-resolved fluorescence anisotropy can give information on its local mobility.

Fluorescence lifetime and quantum yield

The basics behind fluorescence lifetime measurements were described in section 2.1.2. Here we used this method to determine the fluorescence quantum yield of the dye using the following relation:

$$\Phi_{\mathrm{F,sample}} = \frac{\Phi_{\mathrm{F,reference}} \tau_{\mathrm{F,sample}}}{\tau_{\mathrm{F,reference}}} \tag{6.1}$$

where $\Phi_{\mathrm{F,sample}}$ and $\Phi_{\mathrm{F,reference}}$ denote the fluorescence quantum yield of the sample and reference standard, respectively. Correspondingly, $\tau_{\mathrm{F,sample}}$ and $\tau_{\mathrm{F,reference}}$ denote the fluorescence lifetime of the sample and reference standard. However, relation 6.1 is only valid in case of two dyes having the same natural lifetime (see section 2.1.1). Therefore we chose AF488[1] as reference since its data in phosphate buffer at pH 7.2 is already available [70]. As shown in table 6.1, the fluorophore bound to the N-terminus of C(0)Aβ$_{42}$ displays two fluorescent lifetimes. The bigger lifetime of 4.03 ns ± 0.3 ns cannot be distinguished from the lifetime of free AF488 (4.11 ns) [70].

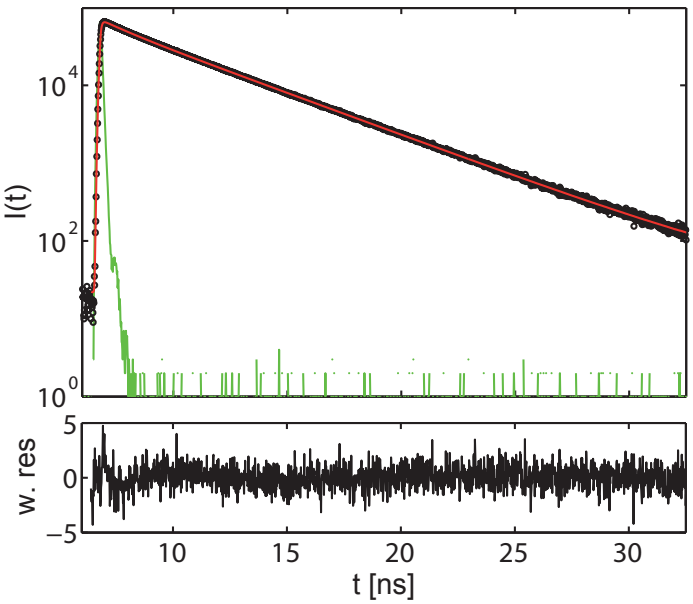

Figure 6.3: Fluorescence lifetime measurement of AF488-C(0)Aβ$_{42}$ in NaPi (pH 7.4). The corresponding fit results are listed in table 6.1.

However the second lifetime is considerably lower than that. This leads to an overall quantum yield of $\Phi_{\mathrm{F,sample}} = 0.82$. Thus, it is about 10 % lower than that of free AF488 ($\Phi_{\mathrm{F,reference}} = 0.92$). It is quite common that dyes exhibit multiexponential fluorescence

[1] Alexa Fluor succinimidyl ester

Table 6.1: Results of the fluorescence lifetime measurements of AF488-C(0)Aβ$_{42}$. The experimental lifetime decay was fitted to a biexponential function with amplitude a_1 and the two fluorescence lifetimes τ_1 and τ_2

a_1	1-a_1	τ_1 [ns]	τ_2 [ns]	$\langle\Phi_F\rangle$	χ_r^2
0.13 (± 0.015)	0.87 (± 0.1)	1.21 (± 0.2)	4.03 (± 0.03)	82 %	1.16

lifetime decays when bound to proteins [19]. Since the fluorescence lifetime is a sensor for the dyes' microenvironment the AF488 bound to C(0)Aβ$_{42}$ might experience quenching by some of the side-chains of the Aβ$_{42}$ peptide. Nevertheless, the free Alexa Fluor 488 maleimide exhibits a biexponential decay itself [72].

Time-resolved fluorescence anisotropy

Time-resolved fluorescence anisotropy data of protein bound dyes contain information about its mobility and can report on its sterical environment. A triexponential model was fitted to the experimental anisotropy decay (see figure 6.4). A biexponential model lead to unsatisfactory results with a $\chi_r^2 = 1.8$.

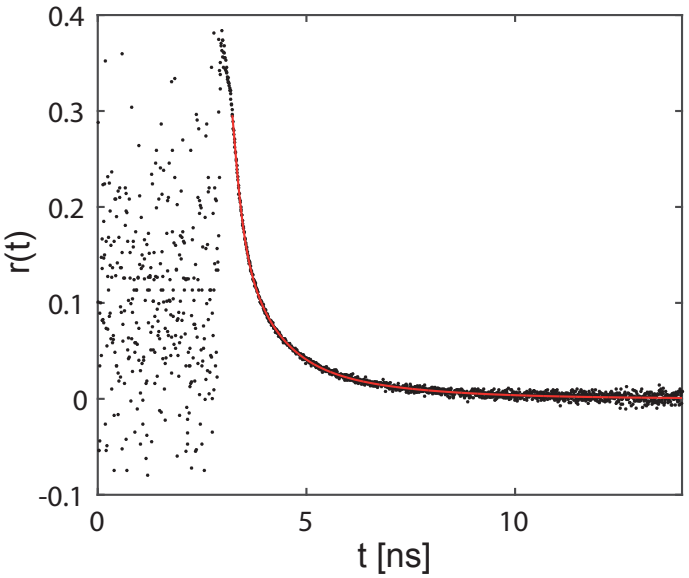

Figure 6.4: Time-resolved fluorescence anisotropy measurement of AF488-C(0)Aβ$_{42}$ in NaPi (pH 7.4). The red solid line denotes a fit to a triexponential decay model. The corresponding parameters are listed in table 6.2.

The results of the time-resolved fluorescence anisotropy masurements are listed in table 6.2 The three rotational correlation times might be interpreted as follows. The first two shorter rotational correlation times can be attributed to local dye dynamics [39]. However, the longest rotational correlation may be attributed to the overall motion of the whole protein dye complex. r_∞ is a valuable parameter to assess the dyes' flexibility. If flexibility of the linker is modelled as diffusion within a cone (*wobbling-in-a-cone*

Table 6.2: Fitting results of the time-resolved fluorescence anisotropy measurements of AF488-C(0)Aβ$_{42}$ in phosphate buffer (pH 7.4). The experimental anisotropy decay was fitted to a triexponential function with amplitudes r_1, r_2, r_3 and the three rotational correlation times ρ_1, ρ_2 and ρ_3.

r_1	r_2	r_3	ρ_1 [ns]	ρ_2 [ns]	ρ_3 [ns]	r_0	r_∞	χ_r^2
0.46	0.39	0.15	0.18	0.79	2.56	0.375 (fix)	0.05	1.05

model, [73]) with the opening half-angle θ_c, one can show that r_∞ is related to θ_c by the following equation [39]:

$$\sqrt{\frac{r_\infty}{r_0}} = 1/2 \cos^2 \theta_c \tag{6.2}$$

Equation 6.2 is valid in case the transition dipole moment is perpendicular to the linker axis. The bigger the cone angle, the more space is available to the dye in which it can freely diffuse. For our case we calculated the half-angle to be $\theta_c = 31°$, indicating that the dye is only slightly restricted in its motion but that the dye does not stick to the peptides' surface. However, a fairly free dye is what might be expected for a fluorophore bound to the N-terminus of the Aβ peptide since all available Aβ structures show a highly flexible N-teminus [3, 4]. This result can be confirmed by an accessible volume (AV) simulation. The parameters used for the AV simulation are listed in table 6.3:

Table 6.3: Dye parameters used for the accessible volume simulation (see figure 6.5).

L_{linker} [Å]	R_1 [Å]	R_2 [Å]	R_3 [Å]	w_{linker} [Å]
18.2	5.65	5.2	1.25	4.5

As the basic peptide structure used for the AV simulation we chose the pdb-file 1Z0Q published by Tomaselli *et al.* [4]. This pdb file contains an ensemble of 30 structures (Aβ$_{42}$ in 70 % H_2O : TFA). For the AV simulation we chose the most representative structure, namely ensemble structure no. 25. We added a cysteine residue to the N-terminus with Pymol and performed the AV simulation with the FRET positioning and screening software (see chapter 3).

The finding that the dye does not stick to the protein is of special importance for the unfolding measurements. A succesive release of a sticky dye from the peptide surface with increasing GdnHCl concentration could lead to an increase of the hydrodynamic radius without the peptide being actually unfolded.

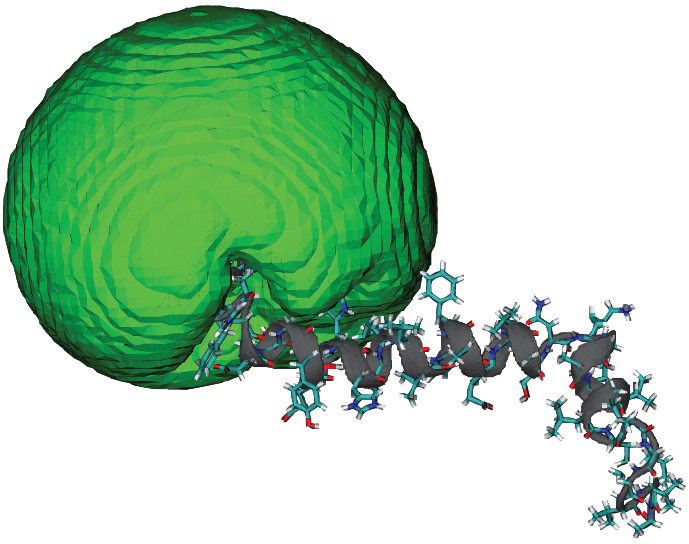

Figure 6.5: Acessible volume simulation results. The green volume represents the space which is accessible to AF488 maleimide when it is linked to the peptide at Cys(0) (dye cloud). The huge dilatation of this volume demonstrates that the dye can occupy a lot of space and suggests that it can thus freely diffuse near the peptide surface.

Excitation and emission spectra

Excitation and emission spectra do report on the chemical environment of the fluorophore [39]. The excitation- and emission spectra of C(0)Aβ_{42} conjugated AF488 and free AF488 are very similar. Thus, it can be assumed that the conjugated fluorophore is in a similar environment as the free fluorophore and that it is not buried within a hydrophobic core or similar. This is consistent with the time-resolved anisotropy data which suggests that the dye is not sticky and thus not buried somewhere. However, there is a bathochromic shift in the excitation- and emission spectra when going from buffer (outer left spectrum for excitation- and emission, figure 6.6) to highly concentrated GdnHCl solutions. Interestingly, similar shifts were also observed for the free dye (figure 6.6 B). However, the shift is more pronounced in the case of the free dye. This might indicate that the dye coupled to the peptide was more shielded against the GdnHCl ions. This would also correspond to the anisotropy results which showed that the dye was not 100 % freely rotating.

Photophysics of the fluorophore

For FFS measurements, there is always a trade-off between obtaining as many photons as possible in a given (short) time interval and reducing effects such as bleaching and triplet blinking. This is especially important when performing PCH measurements, because the basic PCH theory does not incorporate triplet effects. Additionally, avoiding triplet effects increases the reliability of FCS analysis since it reduces the number of fit parameters by two (see equation 2.65). In order to find a suitable laser

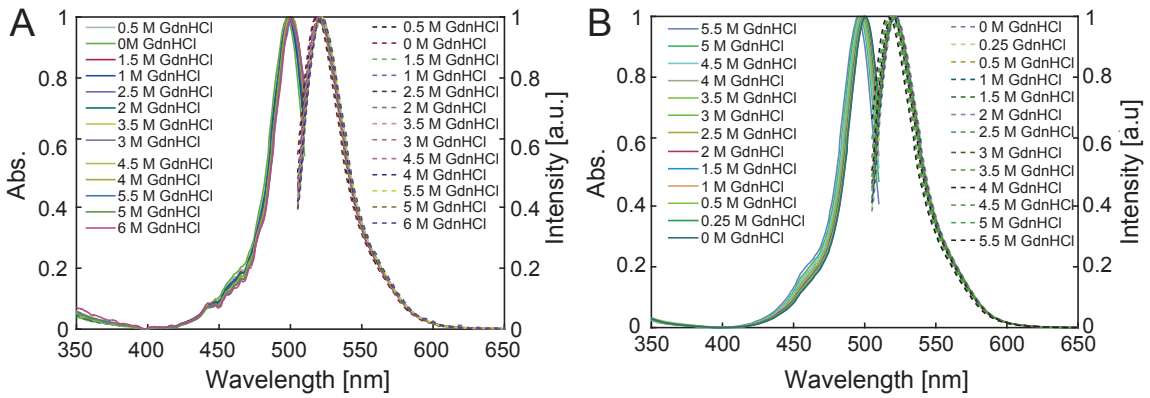

Figure 6.6: Excitation (solid lines) and emission spectra (dashed lines) of AF488-C(0)Aβ_{42} (**A**) and of AF488 (**B**).

power, at which the amount of triplet can be regarded as negligible, we performed FCS measurements of AF488 under varying laser powers. We found that a laser power below 30 μW lead to a triplet fraction below 1 % (see figure 6.7). Thus a laser power of 20 μW was subsequently chosen for all the FFS experiments (if not stated otherwise).

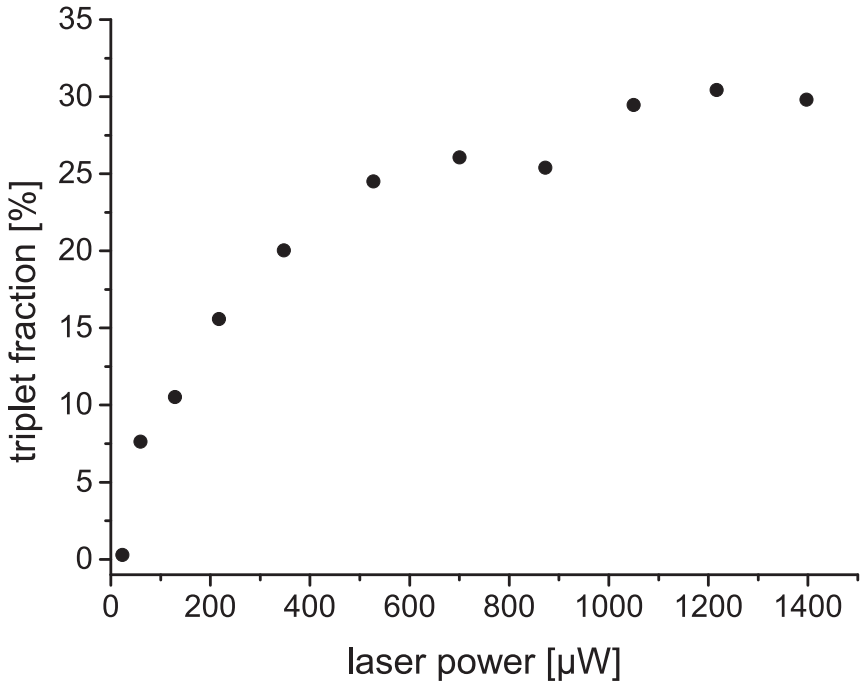

Figure 6.7: A plot of the triplet fraction versus the excitation laser power elucidates that FFS experiments performed below 30 μW show a negligible amount of triplet (< 1 %).

6.2 Adsorption artifacts in FFS

During some of our FFS experiments we observed a continous change in the intensity trace. Mostly we observed a continous decrease in the intensity. There are several reasons why this can happen. The most reasonable assumptions might be as follows:

1. unstable laser intensity.
2. bleaching of the fluorophore.
3. adsoprtion of the fluorophore to the sample holder.

Since the laser intensity was checked before and after the experiment and was observed to be very stable, the last two assumptions were explored in more detail. For that purpose, N&B analysis (see section 2.1.4.1) was performed. This method can immediately be applied to the intensity trace to extract the average number of particles in the observation volume, as well as their brightness. It is easily implemented and very fast. Figure 6.8 A gives an example of an intensity trace which slowly decreases over time. This decrease can solely be attributed to the adsorption of fluorescent molecules to the sample holder (see figure 6.8 B).

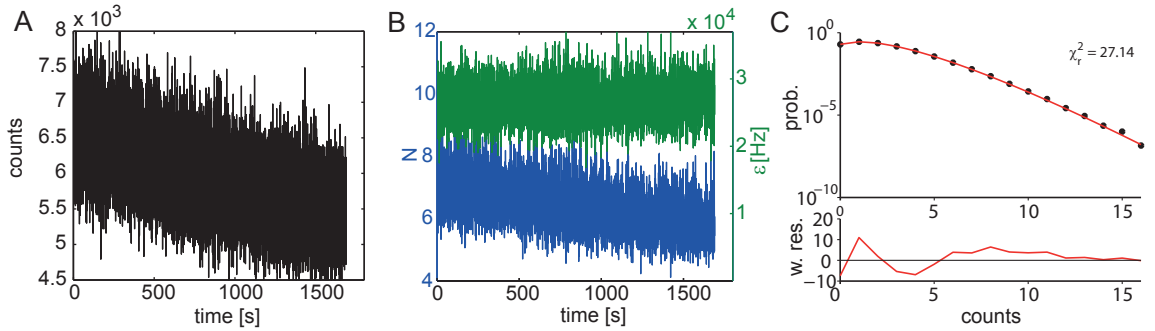

Figure 6.8: (**A**) Intensity trace of AF488-C(0)Aβ_{42} which is slowly decreasing. (**B**) N&B analysis reveals that the average number of particles (N, blue line -) in the effective volume slowly decreases during the measurement while the brightness (ε, green line -) stays constant. (**C**) Effect of adsorption onto PCH-fitting results. The red line in the upper subplot is the best-fit line to a one-component model with fixed out-of-focus emission factor.

The adsorption effect was especially prominent in case when glass slides were used instead of well plates. Adsorption had an impact on photon counting histogram fitting. A one-component fit of sample data with fixed out-of-focus emission factor F (see section 2.1.4.2) lead to a rather poor fit (see figure 6.8 C). Our first assumption was that the decreasing intensity trace skews the photon counting histogram. In order to test this hypothesis, we ran a Brownian dynamics simulation (see section 4.8) where the particles were allowed to leave the system and without being replaced

by new ones. In this way we simulated the adsorption process. The correpsonding photon counting histogram was fitted using a one-component model (figure 6.9 B). The appropriate result can be seen in figure 6.9. A χ_r^2 equal to 1.2 indicates a very good

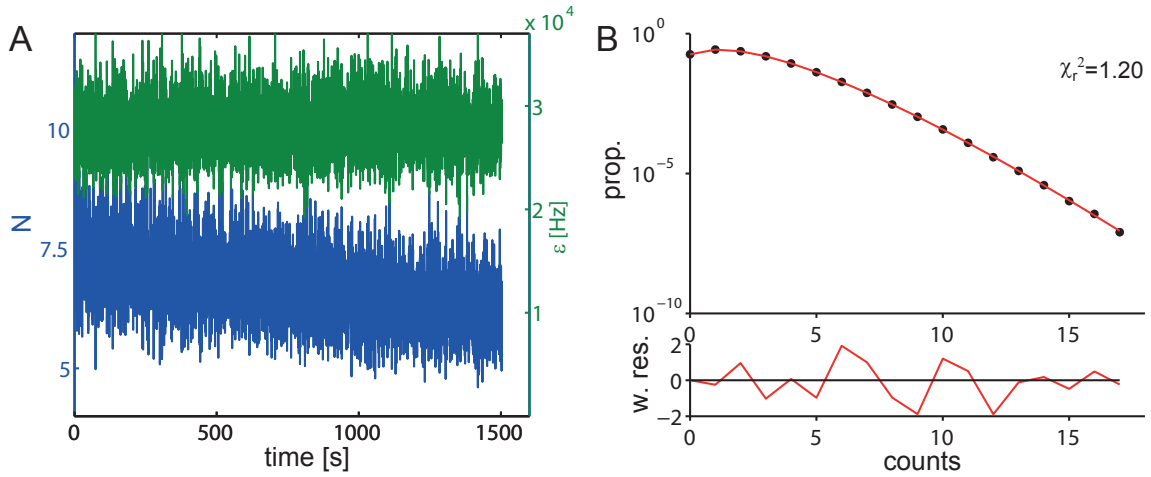

Figure 6.9: (**A**) N&B traces from simulated data. The average number of molecules in the effective volume (blue line -) decreases due to succesive removal of particles from the simulation box. This is supposed to simulate the adsorption process. However, the brightness (ε, green line -) stays constant (compare figure 6.8). (**B**) The corresponding photon counting histogram (●) with a one-component model fit (red line -) shows that the fit model is still valid despite the decreasing intensity.

fit. Correspondingly, the continious decrease of the intensity trace does not make the one-component fit fail. Our next hypothesis was that an accumulation of fluorescent molecules near the surface of the glass slide increases the fraction of out-of-focus emission. This means that the out-of-focus emission should increase over time, because more and more molecules adsorb to the glass surface and contribute to out-of-focus emission. In order to prove this, we chopped the intensity trace into 5 subsets and analysed their PCHs separately in terms of the one-component model with out-of-focus correction. However, in this case the out-of-focus emission factor F was left as a free parameter. The corresponding results are shown in figure 6.10 A. It can be seen that a decreasing number of molecules corresponds to an increasing F-value. To show that the trend in the F-Value is not random, we performed another measurement with Oregon Green 488. We had previosuly discovered that this dye has a tendency to adsorb to the glas slide surface, too. The same analysis was performed on this data set and the corresponding results are shown in figure 6.10 B. However, figure 6.10 C shows the results for AF488 which did not show any detectable adsorption. Thus, its number trace stays almost constant and its F-value only scatters equally distributed around its mean value (dashed lines). However, the scattering is remarkably higher than in the two former cases. This can likely be attributed to the much lower number of photon counts which were used to generate the PCH. It shall be noted that leaving the F-value variable in fitting the PCHs lead to very good fits in all cases (including

the AF488-C(0)Aβ_{42} data). As a result, in case there was a non-negilible sample adsoprtion, we left the F-value a variable parameter in the PCH fitting procedure.

6.3 Refractive index mismatch in 1fFCS measurements

The influence of GdnHCl concentration on FCS measurements became visible in the change of the effective volume (see figure 6.11 A). Its dimension changed about fourfold from 0 to 5.5 M GdnHCl. It is interesting to note, that especially the elongation of the PSF in the z-direction contributes to the change in the effective volume (see figure 6.11 B), whereas the elongation in x-y-direction only changes by a factor of about 18 %. Chattopadhyay *et al.* proposed a correction procedure based on changing the correction collar of the water immersion objective [74]. However this procedure seemed very time-consuming and we anyway needed the molecular brightness of AF488 in different GdnHCl solutions to compare it to the brightness of the dye-peptide complex in the PCH analysis.
Surprisingly, the correlation curves could still be properly fitted to the diffusion model derived for a three-dimensional Gaussian (see equation 2.64), despite the optical abberation. The increasing effective volume leads to an icreased apparent number of observed molecules in that volume (see figure 6.12). All these effects have been predicted by Enderlein *et al.* from model calulcations [75, 76]. The increasing apparent number of particles has a direct influence onto the correlation curve since the relative fluctuations become smaller. Therefore the amplitude of the correlation curve drops. Practically this means that the correlation curve might become very noisy for a given measurement time. However, there are various ways to circumvent this issue. Since an increasing refractive index of the sample solution leads to a very similar effect as an increasing cover-slide thickness [32], one can correct for refractive index mismatches using the objectives' correction collar [74]. Measuring near the cover-slide surface would be another (easy) option to circumvent the difficulties introduced by refractive index mismatch [76, 77]. This is illustrated in figure 6.13). In case there are no optical abberations generated by refractive index mismatch of the immersion- and sample medium, the excitation point spread function is symmetric around the axis of light propagation (figure 6.13 A). The observation volume is at its minimum value. At high refractive index mismatch the symmetric shape of the PSF is lost (figure 6.13 C) but can be recovered the closer the laser focus is moved towards the glass/sample medium interface (figure 6.13 B). However, due to the adsorption tendency of Aβ_{42} this might lead to additional artifacts. Thus, this option would need some further investigations.

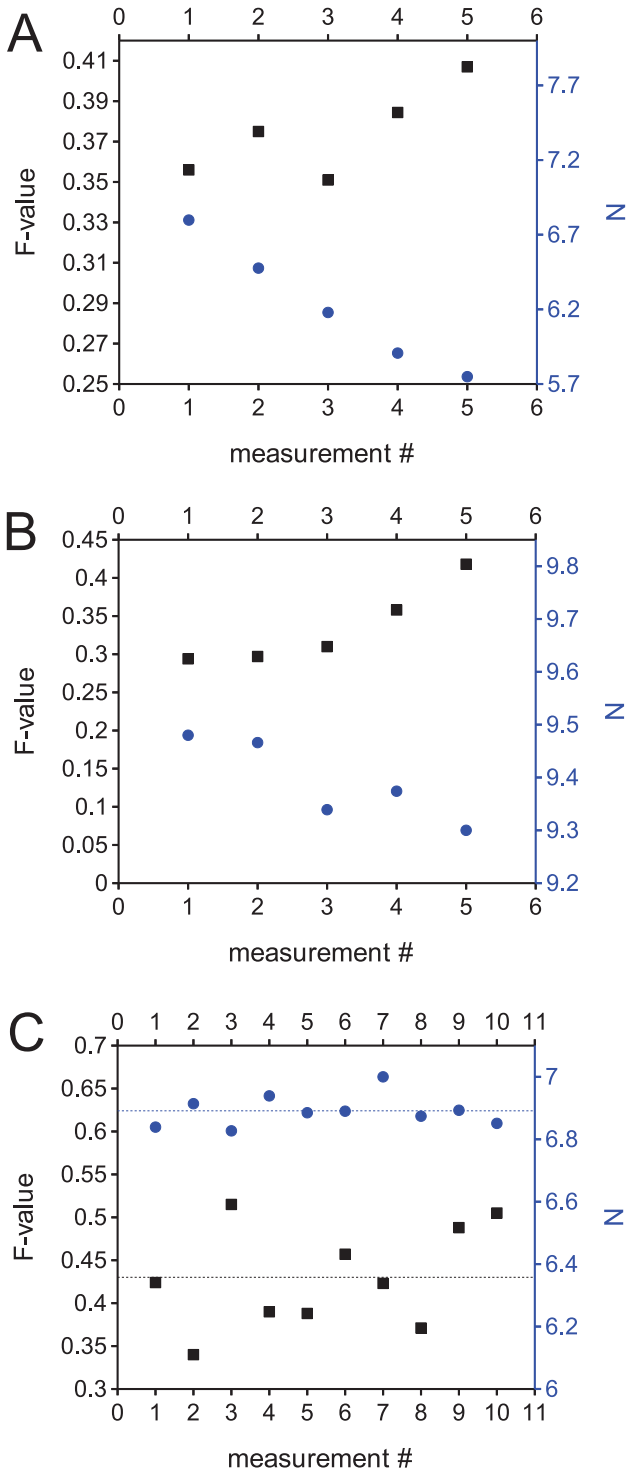

Figure 6.10: (**A**) Out-of-focus emission (F-value, ■) and number (N, ●) from PCH analysis of AF488-C(0)Aβ_{42} data. As the number of molecules in the effective volume decreases, the out-of-focus emission incrases. (**B**) Out-of-focus emission (F-value, ■) and number (N, ●) from PCH analysis of Oregon Green 488 data. This data is used as a reference since Oregon 488 had been observed to adsorb to the glass slide surface, too. **C** Out-of-focus emission (F-value, ■) and number (N, ●) from PCH analysis of AF488 data. The number of molecules stays almost constant and thus the F-value scatters around its mean value (dashed line). The scattering amplitudes in (**C**) are much bigger than for (**A**) and (**B**) because the number of detection events was much lower.

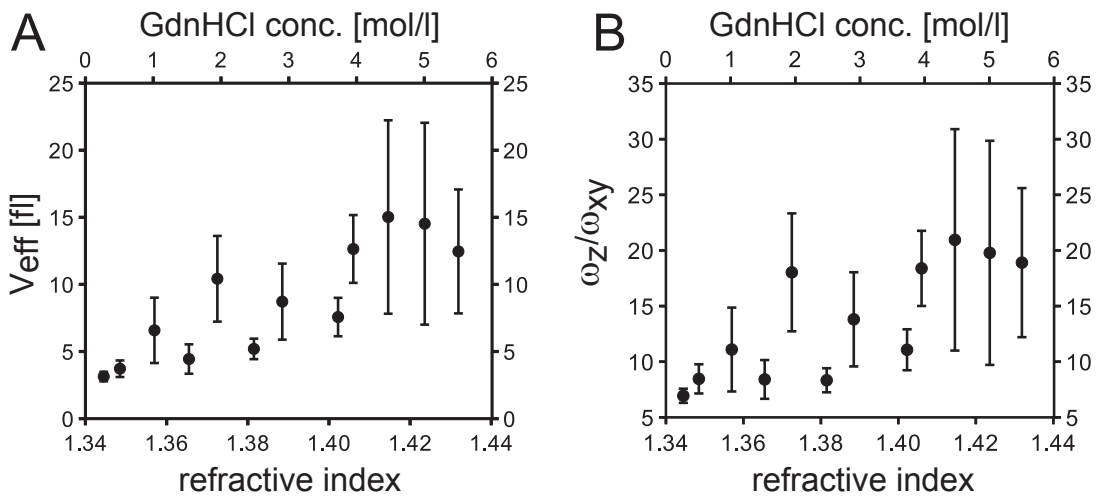

Figure 6.11: (**A**) Change in the effective observation volume with increasing GdnHCl concentration/refractive index. (**B**) The elongation of the PSF along the z-axis (herein denoted as the ratio ω_z/ω_{xy}) contributes most to the increase in the observation volume.

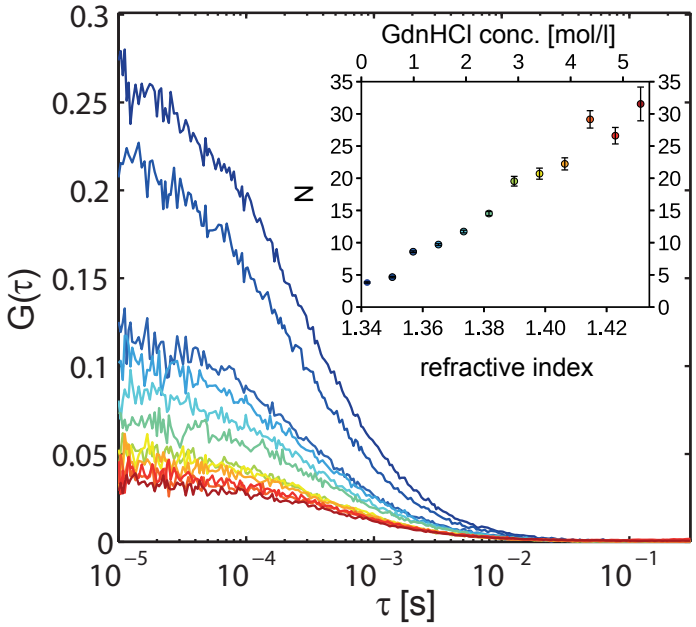

Figure 6.12: Correlation curves of AF488 in solutions of increasing GdnHCl concentration (0 → 6 M GdnHCl, dark blue → dark red) The average number of particles increases due to an increasing observation volume (see also figure 6.11).

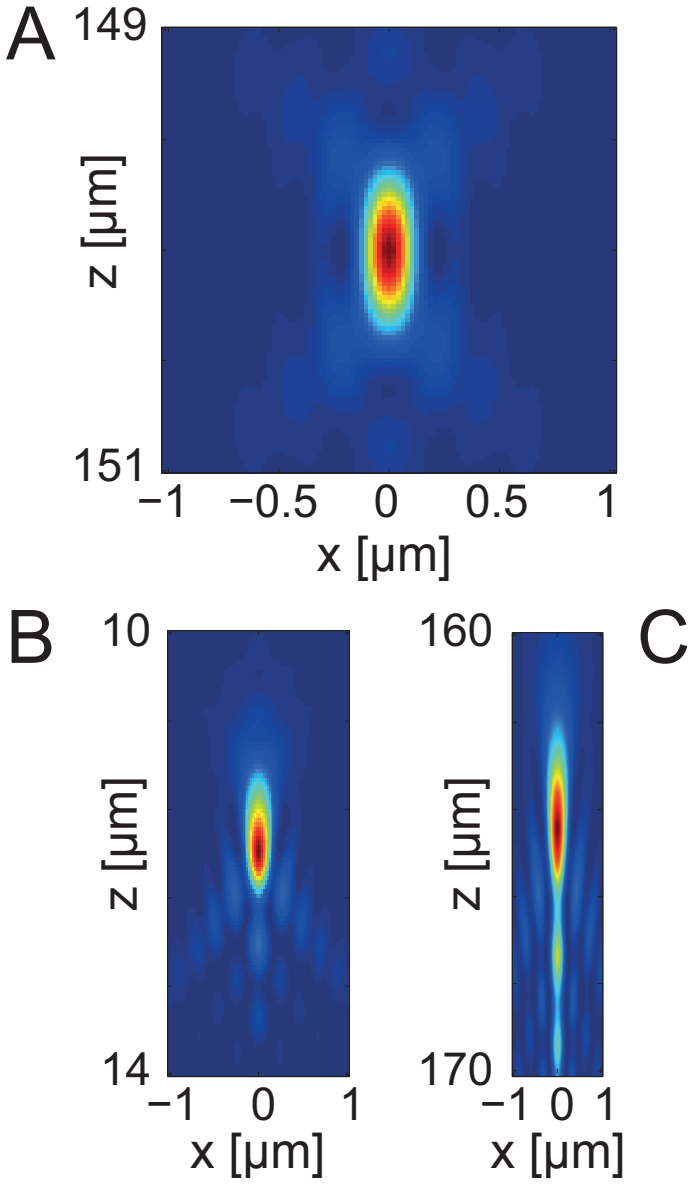

Figure 6.13: Calculated excitation point spread functions (PSF). (**A**) PSF for non-abberated conditions ($n_{\text{sample medium}} = n_{\text{immersion medium}} = 1.334$, depth=150 μm). (**B**) abberated conditions ($n_{\text{sample medium}} = 1.436 \neq n_{\text{immersion medium}} = 1.334$, depth: ≈ 12 μm). (**C**) abberated conditions ($n_{\text{sample medium}} = 1.436 \neq n_{\text{immersion medium}} = 1.334$, depth: ≈ 164 μm). The laser excitation wavelength was set to 470 nm and the beam was assumed to be polarised along the y-direction. All the figures were generated with the PSF Lab software [53].

6.4 Aβ_{42} is monomeric under FCS measurement conditions

Although the fits of the fluorescence correlation curves to a one-component diffusion model (equation 2.64) are excellent, it is well-known that the resolvability of FCS is rather limited [78]. E.g. Meseth *et al.* found that a factor of at least 2.6 in ratio of the diffusion times is necessary to distinguish two species of equal brightness (15 kHz), in which 90 % are of the first size and 10 % of the particles are of the second size. However, this means that the second (bigger) species should have a diffusion coefficient which is at least 38.5 % lower than that of the smaller species. Hence, in order to be sure that the observed unfolding transition is solely due conformational changes of monomers, we performed PCH analysis on the data set of the FCS unfolding experiments. The presence of oligomers in the solution would lead to the appearance of fluorescence bursts with higher intensity (due to the presence of multiple fluorophores) which in turn would lead to the appearance of a higher number of photon counts in the photon counting histogram. Thus, the one-component fit would fail and result in a reduced chi-squared far from one. As can be seen in figure 6.14, fitting the experimental PCH of AF488-C(0)Aβ_{42} to a one-component model gives a good fit with reduced chi-squared close to one. Additionally, the fact that the brightness values of free AF488 dye and AF488-C(0)Aβ_{42} are similar (see table 6.4), gives another hint to the sole presence of AF488-C(0)Aβ_{42} monomers. A substantial amount of oligomeric species would push the average brightness towards a higher value. The slightly lower brightness of Alexa Fluor 488 maleimide could likely be attributed to quenching of the fluorophore by its own maleimido group [79]. This assumption is also supported by taking a closer look at the fluorescence lifetime decays of free AF488 maleimide and AF488-C(0)Aβ_{42} (see figure A.1 in the Appendix). However, the presence of multiple fluorophores in

Table 6.4: Comparison of the fit parameters from PCH analysis of AF488 maleimide and AF488-C(0)Aβ_{42}. Both brightness values are similar, indicating that the AF488-C(0)Aβ_{42} exists in its monomeric form.

Sample	ε [kHz]	χ_r^2
AF488	21.29 ($\pm$ 0.54)	0.8
AF488-C(0)Aβ_{42}	22.30 ($\pm$ 0.23)	1.2

an oligomer in close proximity to each other could lead to self-quenching between neighbouring dyes [80]. This in turn would result in a more reduced brightness than expected for an oligomer of n monomeric units and this can lead to the result that certain oligomers and monomers would have a similar brightness. In this case, they could thus not be resolved with PCH analysis. Nevertheless, the combined analysis of FCS and PCH data at least hints at the absence of oligomeric species.

It shall be noted that the verification of the monomeric structural conformation is performed on the same dataset which was finally used to contruct the unfolding curve. This is in contrast to other methods like CD spectroscopy or Bis-ANS fluorescence, in which the verification is done on a separate instrument (e.g. SEC) after the actual unfolding measurements. In case there are oligomers detected afterwards, this does not necessarily mean that they had been present during the structural measurements [4].

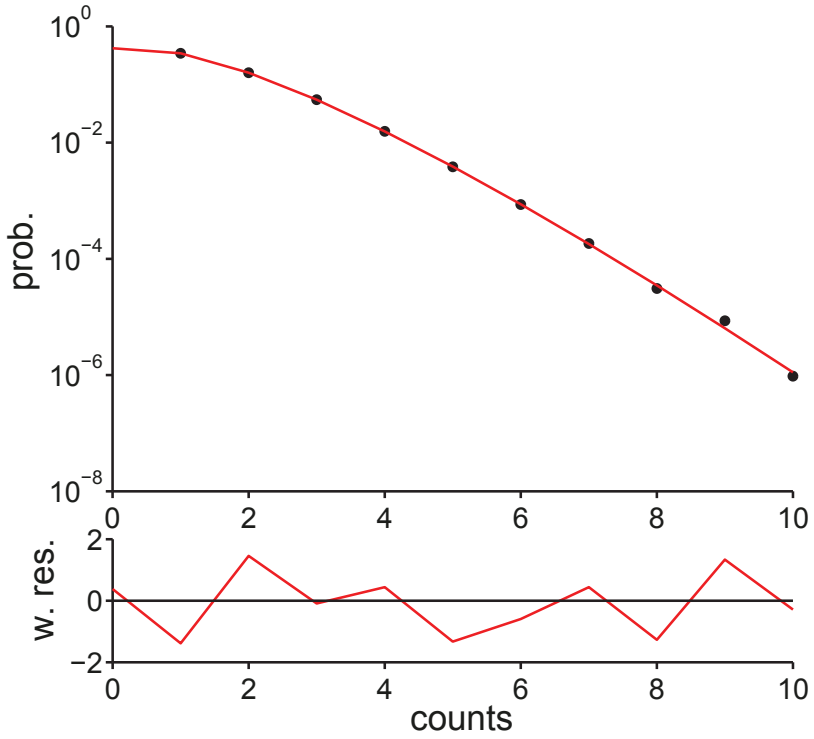

Figure 6.14: Photon counting histogram analysis of AF488-C(0)Aβ$_{42}$ in 0.5 M GdnHCl solution. The solid red line in the main plot is a fit to the one-component PCH model (see equation 2.42). A $\chi^2_r = 1.2$ denotes an excellent fit and thus indicates the absence of oligomeric species.

6.5 AF488-C(0)Aβ$_{42}$ monomer unfolding with GdnHCl

FCS was applied in several studies of protein unfolding [74, 81, 82], but in all of these cases the molecular weight of the proteins was typically >15 kDa and the corresponding change in the hydrodynamic radii from native to the denatured conformation was usually >10 Å. However, in our study, the unfolding of dye-labeled C(0)Aβ$_{42}$ (about 5 kDa) was examined which is substantially smaller. Correspondingly, the change

in the hydrodynamic radius between the native- and denatured conformation was expected to be much smaller. The hydrodynamic radii were calculated from the correlation curves which were obtained from the denaturation experiments of AF488-C(0)Aβ$_{42}$ in various GdnHCl solutions (see figure 6.15). The correlation curves shifted towards higher correlation times with increasing GdnHCl concentration. There are

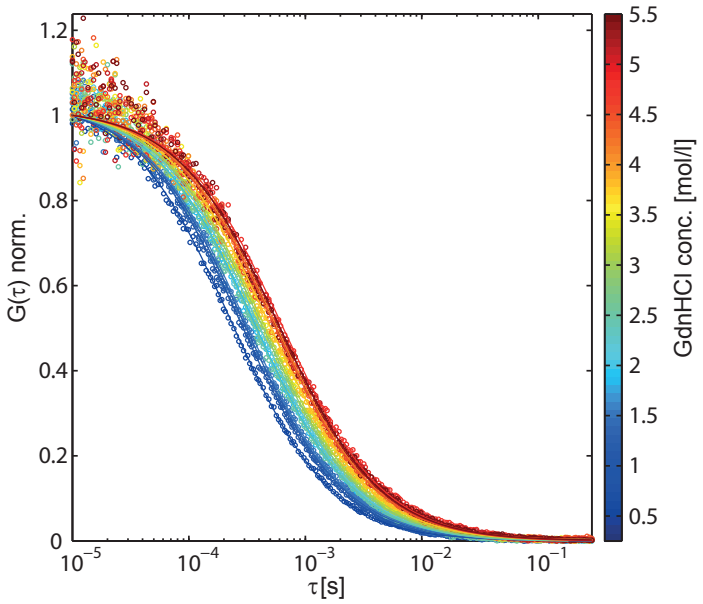

Figure 6.15: Correlation curves of AF488-C(0)Aβ$_{42}$ in various GdnHCl solutions. The shift towards higher correlation times corresponds to the increasing solution viscosity and conformational changes of the Aβ$_{42}$ peptide (see also figure 6.16).

mainly two effects which contribute to this shift. An increasing solution viscosity and conformational changes of the peptide increase the diffusion coefficient. Their corresponding contributions are depicted in figure 6.16. In the range between 0 and 0.7 M GdnHCl it is mainly the change in viscosity which contributes to the shift in the corresponding correlation curves (figure 6.15). Between 0.7 and 4 M GdnHCl changes in the peptide conformation mainly contribute to the overall change in the diffusion coefficient and thus to the shift in the correlation curves. Between 4 to 6 M GdnHCl it is again the viscosity which mainly leads to the shift in the correlation curves. Nevertheless, at least within the transition region (≈ 1-2.5 M GdnHCl) it is mainly the change of conformation which overwhelms the contribution of the viscosity. This might likely be different for thermal unfolding in which both the temperature and the change in viscosity lead to a shift in the correlation curves *per se* [32]. In this case, the conformational change of the peptide has only a minor contribution to the shifts of the correlation curves.

Calculating the hydrodynamic radii R_H from the diffusion coefficients according to the Stokes-Einstein relation (equation 2.71) and subsequently plotting R_H versus the GdnHCl concentration reveals the unfolding/denaturation curve of the AF488-C(0)Aβ$_{42}$ (figure 6.17). The hydrodynamic radius of the native conformation $R_{H,N}$

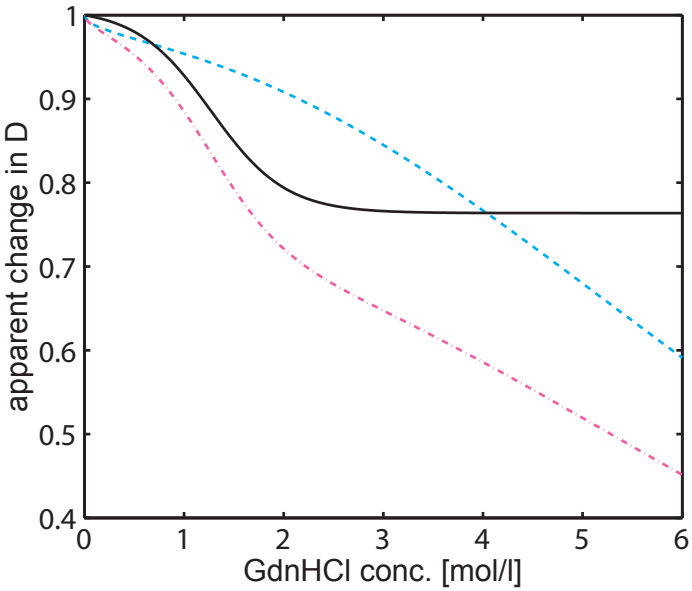

Figure 6.16: Relative change of the diffusion coefficient solely due to the change in viscosity (cyan dashed line), in conformation of the peptide (black line) and due to the concurrence of both effects.

can be assessed from the unfolding curve by extrapolation of the hydrodynamic radius to zero molar GdnHCl. Here it was estimated to be 9.6 Å. A $R_{h,N}$ value of 9.6 Å is very close to the 9 ± 1 Å reported by Nag *et al.* [83]. However, the hydrodynamic radius of the unfolded conformation $R_{h,U}$ can be assessed from the plateau in the unfolding curve at high GdnHCl concentrations. Here it was estimated to be $R_{h,U}$ of about 13.3 Å. This value is an average over the $R_{h,U}$ values from the plateaus of both unfolding in figure 6.17. The corresponding unfolding curves followed by 1fFCS and 2fFCS are shown in figure 6.17 A and 6.17 B, respectively. It is interesting to note that the error bars tend to increase with increasing GdnHCl concentration. The reasons for this may be manifold. One reason is that the effect of a change in solution viscosity overwhelms the contribution due to structural changes of the peptide (see above). Another interesting phenomenon which, to some extent, contributes to the bigger error bars at high GdnHCl concentration is that both the excitation and emission spectra show a bathochromic shift with increasing GdnHCl concentration (see figure 6.6). For a given laser wavelength (470 nm) this means that a bathochromic shift in the excitation spectrum corresponds to a lower excitation probability. The bathochromic shift in the emission spectra finally leads to a decrease in the detected intensity since the emission filter set had been chosen according to the non-shifted spectrum at zero molar GdnHCl. Nevertheless, it is important to note that FCS enabled us to follow such tiny changes in hydrodynamic radius down to the low Angstrom range. It can further be noted that both FCS methods give comparable diffusion coefficients (insets of figure 6.17) and hydrodynamic radii despite the fact that 1fFCS is very sensitive towards optical aberrations like refractive index mismatch. This indicates that our calibration

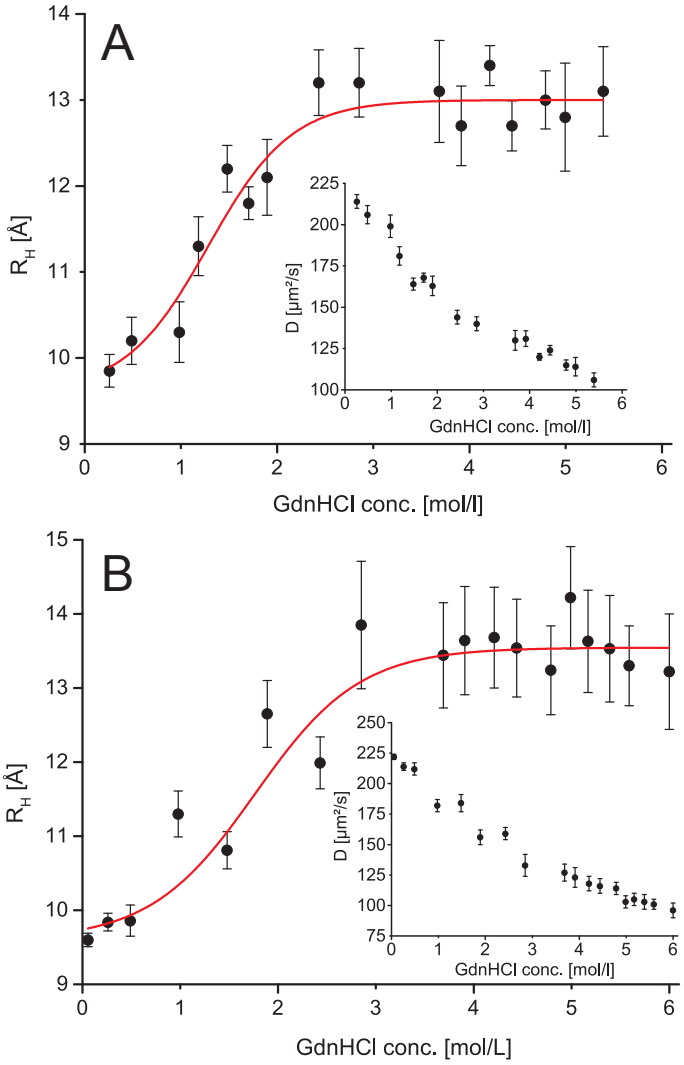

Figure 6.17: Unfolding curves obtained from 1fFCS (**A**) and 2fFCS anlysis (**B**). Red lines correspond to best-fit lines to the two-state unfolding model 2.88. The hydrodyamic radii R_H were calculated from the corresponding diffusion coefficients D (see inset). Error bars denote the standard deviation of D and R_H respectively from fitting ten individual correlation curves.

procedure for 1fFCS is valid even at high GdnHCl concentrations and that optical corrections are not needed like those described by Chattopadhyay *et al.* [74]. The unfolding curves were fitted to equation 2.88. The corresponding estimated parameters are listed in table 6.5. The most interesting parameter extracted from the unfolding

Table 6.5: Parameter estimates from fitting the AF488-C(0)Aβ_{42} unfolding curves (figure 6.17)

Method	ΔG^{H2O} [kcal/mol]	m [kcal/mol/M]	$R_{H,N}$ [Å]	$R_{H,N}$ [Å]	χ^2_r
1fFCS	1.74 (± 0.31)	1.36 (± 0.22)	9.6 (fix)	13.0 (fix) (± 0.43)	1.03
2fFCS	1.94 (± 0.26)	1.10 (± 0.17)	9.6 (fix)	13.5 (fix) (± 0.67)	1.47
Average	1.84 (± 0.29)	1.23 (± 0.20)	9.6	13.25 (± 0.55)	

curve analysis is the free energy in the absence of denaturant ΔG^{H_2O}. It reports on the stability of the native conformation [84] and is thus often used to compare the stability of protein mutants with their corresponding wild-type. This, in fact was done by Ni *et al.* for different Aβ_{40} variants [60]. They determined a slightly higher value of ΔG^{H_2O} for Aβ_{40} (2.04 kcal/mol) and a much higher m-value (-2.84 kcal/mol/M) compared to our values (table 6.5). Furthermore, in their publication they show that the stability of different Aβ_{40} mutants determined the kinetics of nucleation. However, they performed their experiments in 5 % 2,2,2-trifluorethanol (TFE) which is known to induce alpha-helical structure in Aβ. Thus, the value of ΔG^{H_2O} might be lower without TFE. Chen *et al.* reported a ΔG^{H_2O} value of 1.1 kcal/mol and a m-value of 0.7 kcal/mol/M for Aβ_{40} even though they performed their unfolding experiments in urea and not in GdnHCl [85]. In contrast to our experiments, measurements reported by the latter two references were performed at 25 °C. ΔG^{H_2O} is highly temperature dependent [48, 86] which might explain the smaller value reported by Chen et al. We also calculated the solvent accessible surface area ΔSASA from the m-value according to equation 2.89. A ΔSASA of 1204 ± 2137 Å^2 is reasonable when compared to other peptides [52] although the error is remarkably big. Nevertheless, this value might be used as a benchmark value for other studies, especially for MD simulations of Aβ_{42} since therein the calculation of ΔSASA is straightforward [51].

After all, our ΔG^{H_2O} value is quite small indicating a rather loose structure. However, the presence of a cooperative unfolding curve indicates the existence of structural elements in the Aβ_{42} sequence and is thus distinct from a completely random coiled peptide. Our value is bigger than typical values for the strength of hydrogen bonds within proteins ($\approx$ 0.5-1.5 kcal/mol, see e.g. [87]). If we neglect the possibility of the presence of β-sheet, these results might indicate the presence of a small amount of helical structure of Aβ_{42}, which would correspond to the NMR results reported by Tomaselli et al. [4]. In this case the ΔG^{H_2O} value suggests the presence of only a small amount of helical structure with at maximum 2-3 helical windings. Nonetheless,

further studies have to be performed to obtain more verified results about the presence of structural motifs of the Aβ_{42} monomer under near-physiological conditions.

7

Conclusion and outlook

Single-molecule fluorescence spectroscopy and fluorescence fluctuation spectroscopy have become invaluable tools for studying protein conformation, dynamics and interaction. These methods typically perform at very low concentrations and are thus well-suited to study highly aggregation-prone proteins. Fluorescence fluctuation-based methods were applied to explore the unfolding and stability of monomeric amyloid-β 42 ($A\beta_{42}$), a peptide which plays an important role in the progression of Alzheimer's disease. In addition, a Bayesian method for fluorescence burst identification and analysis, based on time-correlated single photon counting data, was developed to extract fluorescence detection events of single molecules within a set of raw data.
In the following two sections, I will conclude with the main results and give a concrete outlook on (possible) future works.

7.1 $A\beta_{42}$ monomer unfolding

In this work, it was demonstrated that $A\beta_{42}$ shows a cooperative unfolding curve upon unfolding with guanidine hydrochloride. The unfolding was explored by fluorescence correlation spectroscopy which allows to perform experiments under nanomolar concentrations and thus under near-physiological concentrations. As was shown, these conditions solely favour the monomeric conformation of $A\beta_{42}$. Careful analysis of the unfolding curves revealed a rather loose structure of the peptide with only a low amount of structural elements. The low free energy of the native conformation ($\approx$ 1.8 kcal/mol) correlates with the high aggregation propensity of the $A\beta_{42}$ [60]. We assume that the structural elements are due to a residual amount of alpha-helical content. However, this assumption has to be underpinned by more experiments. One could, for example, induce certain (known) $A\beta_{42}$ structures and perform the unfolding on these structures. This might enable to elucidate which kind of structural elements are present in the native conformation. Nevertheless, the unfolding method presented here could also be used to test the influence of different drug candidates on Aβ monomers under near-physiological concentrations. Two-colour FCS or PCH analysis could be applied in order to prove that interaction of both molecules takes place and to

do the unfolding measurements in one run. The same applies to investigations on the interaction between $A\beta_{42}$ with other amyloid-β peptides (e.g. $A\beta_{40}$). However, future trials should assess the impact of temperature on the unfolding. Since all experiments were performed at about 23°C it would be important to check if structural elements are still present at 37°C. Additionally, it would be interesting to relate the changes in hydrodynamic radius to absolute distance changes as measured by FRET. We already initiated a corresponding project in which we try to incorporate an unnatural amino acid into the $C(0)A\beta_{42}$ sequence in order to specifically attach two fluorescent dyes to the peptide.

7.2 Bayesian burst identification

Besides exploring $A\beta_{42}$ unfolding, a new method of fluorescence burst identification based on Bayesian model comparison was implemented. This method uses all available information, namely micro- and interphoton times, from a single-molecule fluorescence experiment with TCSPC detection system in order to discriminate between fluorescence bursts and background. This is in contrast to other burst identification methods which only make use of a subset of data to perform the burst identification task, either microtimes or interphoton times. Based on the F-score our method shows an improved burst recognition compared to the other methods. Interestingly, our analysis reveals, that a burst identification based on interphoton times shows a lower burst recognition rate than using fluorescence lifetime information or both types of information at the same time. Our method was successfully applied to experimental data of AF488 in water. Since this method is based on Bayesian model comparison, future analysis will reveal the influence of different priors on the burst recognition. In addition, we are going to explore the influence of the fluorescence lifetime and especially of the signal-to-noise ratio on the burst recognition. In principle, this method can be adapted to include information of more complex data like fluorescence polarisation or data from FRET experiments. However, this will be the scope of a future project.

8

Summary

Alzheimer's disease (AD) is predominantly a disease of elderly people. Due to demographic changes, AD will become even more dominant in future. The exact molecular mechanisms for the development of AD are mainly unknown. However, there exists substantial evidence that the amyloid-β (Aβ) peptide plays an important role [88]. Although Aβ also occurs in healthy brains, it usually degrades very quickly [89]. Nevertheless, it can also aggregate and from oligomers. While a lot of research has focused on these oligomers In recent years, there is no experimental evidence about the monomer structure in pure aqueous solution. This can mainly be attributed to its high aggregation propensity. Aβ aggregation occurs down to the low-micromolar range which makes conventional techniques such as NMR or X-ray diffraction infeasible.
In this work, fluorescence fluctuation-based methods are applied to explore the structural stability of the $A\beta_{42}$ monomer, a 42 amino acids long Aβ isoform. Therefore, a cysteine variant of $A\beta_{42}$ is expressed in *E. coli* and coupled with a fluorescent dye. A purification procedure will be described which guarantees pure monomers with no detectable traces of oligomers. Fluorescence-based methods are well-suited to study highly aggregation-prone proteins and peptides since this kind of measurements are usually performed with pico- to nanomolar concentration of sample. This is especially important in the case of Aβ since it occurs in the nanomolar range *in vivo*. Aβ monomer unfolding is performed in guanidine hydrochloride solutions and detected by fluorescence correlation spectroscopy (FCS). However, conventional FCS is sensitive towards optical aberrations which are caused by an increasing refractive index. As a result, dual-focus FCS is additionally applied which is insensitive towards these aberrations. The unfolding curves reveal a two-state cooperative unfolding of the $A\beta_{42}$ monomer which indicates the presence of stable structural elements. However, the low free energy of the native conformation ($\approx$ 1.8 kcal/mol) indicates a rather low amount of structural elements. However, this low free energy correlates with the high aggregation propensity of $A\beta_{42}$ [60]. The established method could further be used to test the influence of different substances on the structural stability of the $A\beta_{42}$ monomer, including the interaction of the $A\beta_{42}$ monomer with other Aβ species.

Another project included in this thesis deals with the development of a new method to identify fluorescence bursts in single-molecule fluorescence measurements. Fluorescence bursts arise when single fluorescent molecules traverse a small observation volume of

high laser power and subsequently emit bunches of photons (called bursts). Single-molecule fluorescence spectroscopy has become an invaluable tool in the framework of protein dynamics [9] and structure determination [37]. A fluorescence burst identification is mandatory in order to discriminate background counts from single-molecule transits of fluorescent molecules through the laser beam. Most often, fluorescence burst identification is based on intensity information [10–14]. Here we present a burst identification method which makes use of all information inherent in time-correlated single photon counting (TCSPC) data, namely micro- and interphoton time information. The method is solely based on probabilities and is called Bayesian burst identification throughout this work. Based on the F-score, Bayesian burst identification solely based on interphoton time information shows the worst burst recognition rate compared to burst identification solely based on microtime- and on both types of information. The latter one shows a slightly increased burst recognition rate compared to the second last one. Additionally, the Bayesian burst identification is successfully applied to experimental data.

9

Zusammenfassung

Die Alzheimersche Demenz ist eine Erkrankung, deren Auftrittswahrscheinlichkeit mit zunehmenden Alter ansteigt. Im Zuge einer immer älter werdenden Gesellschaft werden dementsprechend immer mehr Menschen mit den Folgen von Alzheimerscher Demenz zu kämpfen haben. Die genauen Mechanismen, die zum Entstehen von Alzheimerscher Demenz führen sind bis heute weitgehend unbekannt. Es zeichnet sich jedoch immer mehr ab, daß das Amyloid-β (Aβ) Peptid eine entscheidende Rolle in diesem Zusammenhang spielt [88]. Aβ wird natürlicherweise in kleinen Mengen im Gehirn gebildet. Die entstehenden Aβ Monomere werden in der Regel wieder abgebaut [89]. Jedoch können sie auch aggregieren und Oligomere und Fibrillen bilden. Während in den letzten Jahren vornehmlich an Aβ Oligomeren geforscht wurde, ist über Aβ Monomere relativ wenig bekannt. Vor allem ist noch keine Struktur in rein wässriger Lösung bekannt. Das ist vor allem auf die starke Aggregationsneigung des Monomers zurückzuführen. Aβ-Aggregation findet bis in den unteren Mikromolarbereich statt, was wiederum dazu führt, daß konventionelle Strukturmethoden wie NMR oder Röntgenbeugung nicht zur Strukturbestimmung anwendbar sind.
In der vorliegenden Arbeit werden verschiedene fluoreszenzfluktuations-basierte Methoden implementiert, um das $A\beta_{42}$ Monomer, eine 42-Aminosäuren-lange Variante des Aβ Peptids, im Hinblick auf seine strukturelle Beschaffenheit und Stabilität hin zu untersuchen. Hierzu wird eine Cystein-Variante des $A\beta_{42}$ Peptids in *E. coli* rekombinant exprimiert und kovalent an einen Fluoreszenzfarbstoff gebunden. Eine in dieser Arbeit beschriebene Aufreinigungsstrategie garantiert das ausschließliche Vorhandensein von $A\beta_{42}$ Monomeren, was mittels 'photon counting histogram' (PCH)-Analyse nachgewiesen wird. Fluoreszenzbasierte Methoden (FCS, PCH, etc.) sind sehr gut geeignet, um stark aggregierende Proteine und Peptide zu untersuchen, da diese Methoden typischerweise mit pico- bis nanomolaren Konzentrationen auskommen. Dies gilt für das $A\beta_{42}$ in besonderem Maße, da es *in vivo* in nanomolaren Konzentrationen vorkommt. Die Entfaltung von $A\beta_{42}$ Monomeren mittels steigenden Guanidinium hydrochlorid Konzentrationen, wird mittels Fluoreszenzkorrelationsspektroskpie (FCS) beobachtet. Hierbei ändern sich die Laserparameter mit höheren Brechungsindizes der Lösungen, was auf optische Aberrationen zurückzuführen ist. Als Referenzmethode wird daher zusätzlich 2-Fokus-FCS eingesetzt, da diese fortgeschrittene FCS Technik sehr unempfindlich gegenüber optischen Aberrationen ist. Die aus den Messungen erhaltenen kooperativen Entfaltungskurven deuten auf das Vorhandensein von stabilen

strukturellen Elementen beim $A\beta_{42}$ hin. Die ermittelte freie Enthalpie ΔG^{H_2O} des nativen Zustands ist jedoch relativ gering, was wiederum auf einen kleinen Anteil struktureller Elemente hindeutet. Die in dieser Arbeit etablierte Methode könnte unter anderem dazu genutzt werden um den Einfluß verschiedener Substanzen auf die strukturelle Stabilität von Aβ Monomeren zu untersuchen. Das schließt nicht nur potentielle Aggregationshemmer mit ein, sondern auch die Wechselwirkung von verschiedenen Aβ-Isoformen untereinander.

Im Rahmen dieser Arbeit wird auch eine wahrscheinlichkeitsbasierten Methode zur Identifizierung von Fluoreszenzbursts (im Folgenden einfach bursts genannt) entwickelt. Bursts entstehen beim Durchtritt von einzelnen fluoreszierenden Molekülen, durch ein kleines Laservolumen, wodurch sie zur Fluoreszenz angeregt werden. Die dabei emittierten Photonen treten gebündelt auf was dann als burst bezeichnet wird. Die Fluoreszenzphotonen werden von einem Detektionssystem detektiert und analysiert. Zur Analyse müssen diese bursts jedoch von Hintergrundereignissen unterschieden werden. Die hier beschriebene Methode soll ein Maximum an Information aus Einzelmoleküldaten der zeitkorrelierten Einzelphotonenzählung zur Identifizierung von bursts verwenden. Hierbei wir mit Hilfe einer entsprechenden Hardware (Photonenzählkarte) jedem Detektionsevent eine Interphotonzeit und eine Mikrozeit zugeordnet. In aller Regel werden bursts basierend auf der Interphotonzeitinformation identifiziert [10–14]. Bei der hier vorgestellten Methode werden jedoch beide Zeitinformationen genutzt. Anhand von simulierten Daten kann gezeigt werden, daß eine Burstidentifizierung basierend auf der Mikrozeiten bzw. auf beiden, Mikro- und Interphotonzeiten, zu einer besseren Burstidentifizierung führt, wobei sich letztere Methode nochmals von den zuvor genannten abhebt. Wie auch gezeigt wird, ist diese Methode leicht auf experimentelle Daten übertragbar. In Zukunft wird diese Methode auf andere komplexere Datenstrukturen erweitert. So sollen beispielsweise Informationen über Polarisation und Farbe mit in die Burstidentifizierung eingearbeitet werden.

10

Danksagung

An dieser Stelle möchte ich mich bei einigen Leuten bedanken. Allen voran möchte ich mich bei Professor Dieter Willbold bedanken. Für die Übernahme der Betreuung, für die Freiheit beim Umsetzen meiner Ideen und nicht zuletzt für die Finanzierung. Weiterhin möchte ich Professor Jörg Fitter für die Übernahme des Koreferats danken. Ferner möchte ich Anna Bronder für ihre Unterstützung bei den AFM-Messungen danken. Bei Lothar Gremer bedanke ich mich für die Einweisung in verschiedene Aufreinigungsmethoden und für seine guten Ratschläge. Stefan Klinker danke ich für seine Unterstützung bei der Expression des Aβ. Bei Chris Cadek bedanke ich mich, für die Expression verschiedener $A\beta_{42}$-Varianten. Bei Filipp Oesterhelt bedanke ich mich für seine Unterstützung beim Aufbau des Einzelmolekül-setups, dessen Bereitstellung für meine Messungen und für seine rege Diskussionsbereitschaft. Meinen ganz besonderen Dank möchte ich Stefan Walta aussprechen, für die Zeit die er mir für die 2fFCS-Messungen und die Viskositäts-/Dichtemessungen geopfert hat. Danke dafür Stefan. Ich hoffe ich kann mich mal irgendwann dafür revanchieren. Katherina Hemmen danke ich für ihre Hilfe bei den zeitaufgelösten Fluoreszenzmessungen. Bei Cordula Kruse bedanke ich mich v.a. für die Unterstützung bei verwaltungstechnischen Angelegenheiten. Mein ganz besonderer Dank gilt Irina Gopich, die sich die Zeit genommen hat mir in ausführlichen Mails all meine Fragen bzgl. der Interphotonzeit-Verteilung zu beantworten. Außerdem danke ich ihr dafür, daß sie mir ihren Diskretisierungscode zur Verfügung gestellt hat. Ich danke außerdem Sabine Metzger für das Durchführen der MS-Messungen. Ferner gilt mein Dank ganz besonders Stefan Walbeck, der sich die Zeit genommen hat die komplette Arbeit durchzulesen und zu korrigieren. Ebenso sei SØren Preus für die Bereitstellung der LaTeX-Vorlage auf fluortools.com gedankt. Außerdem möchte ich meinen Bandkollegen Olli, Manuel und Wördi für die super Bandproben und Auftritte danken, die mich vor allem in der Phase des Zusammenschreibens dann auch mal vom Schreibtisch weggeholt haben. Ein ganz besonderer Dank gilt auch meinen Schwiegereltern Andrea und Wilfried Longerich. Ohne eure Unterstützung wäre mir und meiner Familie einiges deutlich schwerer gefallen. Danke dafür. Meinen Eltern Ruth und Helmut Schneider danke ich dafür, daß sie mich bei meinem Studium kräftig unterstützt haben. Zu guter Letzt möchte ich mich bei demjenigen Menschen bedanken, der mich all die Jahre unterstützt und auf dem Boden der Tatsachen gehalten hat. Dem Menschen, der unter all meinen Verwirrtheiten am meisten zu leiden hatte und den ich zum Teil sehr vernachlässigt habe, meiner Frau

Sarah. Danke für deine Unterstützung und die schönen Jahre mit dir. Ich möchte aber auch nicht meinen Sohn Felix unerwähnt lassen, der es, vor allem in der Phase des Zusammenschreibens, natürlich nicht verstehen konnte, warum Dada nicht mit ihm gespielt hat, obwohl er doch zu Hause war. Ich werde mir wieder mehr Zeit für dich nehmen.

Bibliography

[1] Martin Prince, Wimo Anders, Maëlenn Guerchet, Ali Gemma-Claire, Yu-Tzu Wu, and Prina Matthew. World alzheimer report 2015: The global impact of dementia: An analysis of prevalence, incidence, cost and trends, 2015.

[2] Horst Bickel. Die häufigkeit von demenzerkrankungen, 2014.

[3] Orlando Crescenzi, Simona Tomaselli, Remo Guerrini, Severo Salvadori, Anna M. D'Ursi, Piero Andrea Temussi, and Delia Picone. Solution structure of the alzheimer amyloid beta-peptide (1-42) in an apolar microenvironment. similarity with a virus fusion domain. *European journal of biochemistry / FEBS*, 269(22):5642–5648, 2002.

[4] Simona Tomaselli, Veronica Esposito, Paolo Vangone, van Nuland, Nico A J, Bonvin, Alexandre M J J, Remo Guerrini, Teodorico Tancredi, Piero A. Temussi, and Delia Picone. The alpha-to-beta conformational transition of alzheimer's abeta-(1-42) peptide in aqueous media is reversible: a step by step conformational analysis suggests the location of beta conformation seeding. *Chembiochem : a European journal of chemical biology*, 7(2):257–267, 2006.

[5] H. Sticht, P. Bayer, D. Willbold, S. Dames, C. Hilbich, K. Beyreuther, R. W. Frank, and P. Rösch. Structure of amyloid a4-(1-40)-peptide of alzheimer's disease. *European journal of biochemistry / FEBS*, 233(1):293–298, 1995.

[6] Verena H. Finder and Rudi Glockshuber. Amyloid-beta aggregation. *Neuro-degenerative diseases*, 4(1):13–27, 2007.

[7] Noel D. Lazo, Marianne A. Grant, Margaret C. Condron, Alan C. Rigby, and David B. Teplow. On the nucleation of amyloid beta-protein monomer folding. *Protein science : a publication of the Protein Society*, 14(6):1581–1596, 2005.

[8] P. Seubert, C. Vigo-Pelfrey, F. Esch, M. Lee, H. Dovey, D. Davis, S. Sinha, M. Schlossmacher, J. Whaley, and C. Swindlehurst. Isolation and quantification of soluble alzheimer's beta-peptide from biological fluids. *Nature*, 359(6393):325–327, 1992.

[9] Evangelos Sisamakis, Alessandro Valeri, Stanislav Kalinin, Paul J. Rothwell, and Claus A. M. Seidel. Accurate single-molecule fret studies using multiparameter fluorescence detection. *Methods in enzymology*, 475:455–514, 2010.

[10] C. Eggeling, J. R. Fries, L. Brand, R. Günther, and C. A. Seidel. Monitoring conformational dynamics of a single molecule by selective fluorescence spectroscopy. *Proceedings of the National Academy of Sciences of the United States of America*, 95(4):1556–1561, 1998.

[11] C. Eggeling, S. Berger, L. Brand, J.R Fries, J. Schaffer, A. Volkmer, and C.A.M. Seidel. Data registration and selective single-molecule analysis using multi-parameter fluorescence detection. *Journal of Biotechnology*, 86(3):163–180, 2001.

[12] Wilfried Grange, Philippe Haas, Andreas Wild, Michael Andreas Lieb, Michel Calame, Martin Hegner, and Bert Hecht. Detection of transient events in the presence of background noise. *The Journal of Physical Chemistry B*, 112(23):7140–7144, 2008.

[13] Richard W. Clarke, Angel Orte, and David Klenerman. Optimized threshold selection for single-molecule two-color fluorescence coincidence spectroscopy. *Analytical Chemistry*, 79(7):2771–2777, 2007.

[14] Lucas P. Watkins and Haw Yang. Detection of intensity change points in time-resolved single-molecule measurements: The journal of physical chemistry b. *J. Phys. Chem. B*, 109(1):617–628, 2005.

[15] P. R. Barber, S. M. Ameer-Beg, S. Pathmananthan, M. Rowley, and A. C. C. Coolen. A bayesian method for single molecule, fluorescence burst analysis. *Biomedical optics express*, 1(4):1148–1158, 2010.

[16] Mark I. Rowley, Paul R. Barber, Anthony C. C. Coolen, and Borivoj Vojnovic. Bayesian analysis of fluorescence lifetime imaging data. *Proc. SPIE*, 7903, 2011.

[17] Bernard Valeur. *Molecular fluorescence: Principles and applications*. Wiley-VCH, Weinheim and New York, 2002.

[18] Malte Köllner and Jürgen Wolfrum. How many photons are necessary for fluorescence-lifetime measurements? *Chemical Physics Letters*, 200(1–2):199–204, 1992.

[19] Joseph R. Lakowicz. *Principles of fluorescence spectroscopy*. Springer, New York, NY, 3. ed., corr. 4. print edition, 2010.

[20] Matthias Höller. *Advanced Fluorescence Fluctuation Spectroscopy with Pulsed Interleaved Excitation: Development and Applications*. Dissertation, Ludwig-Maximilians-Universität München, München, 07.01.2011.

[21] Michelle A. Digman, Rooshin Dalal, Alan F. Horwitz, and Enrico Gratton. Mapping the number of molecules and brightness in the laser scanning microscope. *Biophysical journal*, 94(6):2320–2332, 2008.

[22] Jay R. Unruh and Enrico Gratton. Analysis of molecular concentration and brightness from fluorescence fluctuation data with an electron multiplied ccd camera. *Biophysical journal*, 95(11):5385–5398, 2008.

[23] Leonard Mandel. Fluctuations of photon beams and their correlations. *Proceeding of the Physical Society*, (72(6)):1037–1048, 1958.

[24] B. H. Sri Hari and Venugopalakrishna Y. R. On the use of dirac delta distribution in transformation of random variables.

[25] Y. Chen, J. D. Müller, P. T. So, and E. Gratton. The photon counting histogram in fluorescence fluctuation spectroscopy. *Biophysical journal*, 77(1):553–567, 1999.

[26] Thomas D. Perroud, Bo Huang, Mark I. Wallace, and Richard N. Zare. Photon counting histogram for one-photon excitation. *Chemphyschem : a European journal of chemical physics and physical chemistry*, 4(10):1121–1123, 2003.

[27] Bo Huang, Thomas D. Perroud, and Richard N. Zare. Photon counting histogram: one-photon excitation. *Chemphyschem : a European journal of chemical physics and physical chemistry*, 5(10):1523–1531, 2004.

[28] H. Qian. On the statistics of fluorescence correlation spectroscopy. *Biophysical chemistry*, 38(1-2):49–57, 1990.

[29] Rudolf Rigler and Elliot Elson. *Fluorescence correlation spectroscopy: Theory and applications*, volume 65 of *Springer series in chemical physics*. Springer, Berlin and New York, 2001.

[30] Elliot L. Elson and Douglas Magde. Fluorescence correlation spectroscopy. i. conceptual basis and theory. *Biopolymers*, 13(1):1–27, 1974.

[31] Michael Wahl, Ingo Gregor, Mattias Patting, and Jörg Enderlein. Fast calculation of fluorescence correlation data with asynchronous time-correlated single-photon counting. *Optics express*, 11(26):3583–3591, 2003.

[32] Thomas Dertinger. *Two-Focus Fluorescence Correlation Spectroscopy*. Dissertation, Universität zu Köln, Köln, 05.02.2007.

[33] Thomas Dertinger, Victor Pacheco, von der Hocht, Iris, Rudolf Hartmann, Ingo Gregor, and Jörg Enderlein. Two-focus fluorescence correlation spectroscopy: a new tool for accurate and absolute diffusion measurements. *Chemphyschem : a European journal of chemical physics and physical chemistry*, 8(3):433–443, 2007.

[34] H. Qian and E. L. Elson. Analysis of confocal laser-microscope optics for 3-d fluorescence correlation spectroscopy. *Applied optics*, 30(10):1185–1195, 1991.

[35] J. Ross Colvin. The size and shape of lysozyme. *Canadian Journal of Chemistry*, 30(11):831–834, 1952.

[36] V. A. Bloomfield. *Survey of Biomolecular Hydrodynamics: On-Line Biophysics Textbook: (ed. by T.M. Schuster)*. 2000.

[37] Stanislav Kalinin, Thomas Peulen, Simon Sindbert, Paul J. Rothwell, Sylvia Berger, Tobias Restle, Roger S. Goody, Holger Gohlke, and Claus A. M. Seidel. A toolkit and benchmark study for fret-restrained high-precision structural modeling. *Nature methods*, 9(12):1218–1225, 2012.

[38] Adam Muschielok, Joanna Andrecka, Anass Jawhari, Florian Brückner, Patrick Cramer, and Jens Michaelis. A nano-positioning system for macromolecular structural analysis. *Nature methods*, 5(11):965–971, 2008.

[39] Simon Sindbert, Stanislav Kalinin, Hien Nguyen, Andrea Kienzler, Lilia Clima, Willi Bannwarth, Bettina Appel, Sabine Müller, and Claus A. M. Seidel. Accurate distance determination of nucleic acids via förster resonance energy transfer: implications of dye linker length and rigidity. *Journal of the American Chemical Society*, 133(8):2463–2480, 2011.

[40] David J. C. MacKay. *Information theory, inference, and learning algorithms*. Cambridge University Press, Cambridge, UK and New York, 2003.

[41] Devinder S. Sivia. *Data analysis: A bayesian tutorial*. Oxford science publications. Clarendon, Oxford [u.a.], 1. publ., reprint edition, 2005.

[42] A. Alzheimer, R. A. Stelzmann, H. N. Schnitzlein, and F. R. Murtagh. An english translation of alzheimer's 1907 paper, Über eine eigenartige erkankung der hirnrinde. *Clinical anatomy (New York, N.Y.)*, 8(6):429–431, 1995.

[43] Kasper P. Kepp. Bioinorganic chemistry of alzheimer's disease. *Chemical reviews*, 112(10):5193–5239, 2012.

[44] G. G. Glenner and C. W. Wong. Alzheimer's disease: initial report of the purification and characterization of a novel cerebrovascular amyloid protein. *Biochemical and biophysical research communications*, 120(3):885–890, 1984.

[45] J. Kang, H. G. Lemaire, A. Unterbeck, J. M. Salbaum, C. L. Masters, K. H. Grzeschik, G. Multhaup, K. Beyreuther, and B. Müller-Hill. The precursor of alzheimer's disease amyloid a4 protein resembles a cell-surface receptor. *Nature*, 325(6106):733–736, 1987.

[46] Colin J. Barrow and David H. Small. *Abeta peptide and Alzheimer's disease: Celebrating a century of research*. Springer, London, 2007.

[47] J. A. Hardy and G. A. Higgins. Alzheimer's disease: the amyloid cascade hypothesis. *Science (New York, N.Y.)*, 256(5054):184–185, 1992.

[48] Charles Tanford. *Protein denaturation. In Advances in protein chemistry. Vol. 23*, volume 23 of *Advances in protein chemistry*. Academic press, New York, 1968.

[49] C.N. Pace, B.A. Shirley, and J.A. and Thomson. Measuring the conformational stability of a protein. In *Protein structure: A practical approach*, volume IRL Press, Oxford, UK, pages 311–330.

[50] C. N. Pace and K. L. Shaw. Linear extrapolation method of analyzing solvent denaturation curves. *Proteins*, Suppl 4:1–7, 2000.

[51] B. Lee and F. M. Richards. The interpretation of protein structures: estimation of static accessibility. *Journal of molecular biology*, 55(3):379–400, 1971.

[52] J. K. Myers, C. N. Pace, and J. M. Scholtz. Denaturant m values and heat capacity changes: relation to changes in accessible surface areas of protein unfolding. *Protein science : a publication of the Protein Society*, 4(10):2138–2148, 1995.

[53] Michael J. Nasse and Jörg C. Woehl. Realistic modeling of the illumination point spread function in confocal scanning optical microscopy. *Journal of the Optical Society of America. A, Optics, image science, and vision*, 27(2):295–302, 2010.

[54] Bertil Macao, Wolfgang Hoyer, Anders Sandberg, Ann-Christin Brorsson, Christopher M. Dobson, and Torleif Härd. Recombinant amyloid beta-peptide production by coexpression with an affibody ligand. *BMC biotechnology*, 8:82, 2008.

[55] Magnus Palmblad, Anita Westlind-Danielsson, and Jonas Bergquist. Oxidation of methionine 35 attenuates formation of amyloid β-peptide 1–40 oligomers. *Journal of Biological Chemistry*, 277(22):19506–19510, 2002.

[56] Verena H. Finder, Ivana Vodopivec, Roger M. Nitsch, and Rudi Glockshuber. The recombinant amyloid-beta peptide abeta1-42 aggregates faster and is more neurotoxic than synthetic abeta1-42. *Journal of molecular biology*, 396(1):9–18, 2010.

[57] L. M. Jungbauer, C. Yu, K. J. Laxton, and M. J. LaDu. Preparation of fluorescently-labeled amyloid-beta peptide assemblies: the effect of fluorophore conjugation on structure and function. *Journal of molecular recognition : JMR*, 22(5):403–413, 2009.

[58] Harold P. Erickson. Size and shape of protein molecules at the nanometer level determined by sedimentation, gel filtration, and electron microscopy. *Biological procedures online*, 11:32–51, 2009.

[59] D. M. Walsh, A. Lomakin, G. B. Benedek, M. M. Condron, and D. B. Teplow. Amyloid beta-protein fibrillogenesis. detection of a protofibrillar intermediate. *The Journal of biological chemistry*, 272(35):22364–22372, 1997.

[60] Chun-Lun Ni, Hoi-Ping Shi, Hui-Ming Yu, Yun-Chorng Chang, and Yun-Ru Chen. Folding stability of amyloid-beta 40 monomer is an important determinant of the nucleation kinetics in fibrillization. *FASEB journal : official publication of the Federation of American Societies for Experimental Biology*, 25(4):1390–1401, 2011.

[61] Alex Wied and Thomas M. Laue. *Extending the functionality of Sednterp*. University of New Hampshire, [Durham, New Hampshire], 2014.

[62] Claus Bernhard Müller. *Applications of Two Focus Fluorescence Correlation Spectroscopy in Colloid and Polymer Science*. Dissertation, RWTH Aachen, Aachen, 22.08.2008.

[63] ClausB. Müller and Walter Richtering. Sealed and temperature-controlled sample cell for inverted and confocal microscopes and fluorescence correlation spectroscopy. *Colloid and Polymer Science*, 286(11):1215–1222, 2008.

[64] Wolfgang Becker. *The bh TCSPC Handbook*. 2010.

[65] Robert E. Kass and Adrian E. Raftery. Bayes factors. *Journal of the american statistical association*, 90(430):773–795, 1995.

[66] Irina V. Gopich and Attila Szabo. Theory of the statistics of kinetic transitions with application to single-molecule enzyme catalysis. *The Journal of chemical physics*, 124(15):154712, 2006.

[67] Eli Barkai, Frank. L. H. Brown, Michel Orrit, and Haw Yang, editors. *Theory and evaluation of single-molecule signals*. World Scientific, New Jersey, 2008.

[68] Irina V. Gopich and Attila Szabo. Photon counting histograms for diffusing fluorophores. *The journal of physical chemistry. B*, 109(37):17683–17688, 2005.

[69] John Skilling. Nested sampling for general bayesian computation. *Bayesian Analysis*, 2006(4):833–860, 2006.

[70] Daryan Kempe, Antonie Schöne, Jörg Fitter, and Matteo Gabba. Accurate fluorescence quantum yield determination by fluorescence correlation spectroscopy. *The journal of physical chemistry. B*, 119(13):4668–4672, 2015.

[71] W. Blaine Stine, Karie N. Dahlgren, Grant A. Krafft, and Mary Jo LaDu. In vitro characterization of conditions for amyloid-beta peptide oligomerization and fibrillogenesis. *The Journal of biological chemistry*, 278(13):11612–11622, 2003.

[72] Gunnar F. Schröder, Ulrike Alexiev, and Helmut Grubmüller. Simulation of fluorescence anisotropy experiments: probing protein dynamics. *Biophysical journal*, 89(6):3757–3770, 2005.

[73] K Kinosita Jr. Kazuhiko, Suguru Kawato, and Ikegami Akira. A theory of fluorescence polarization decay in membranes. *Biophysical Journal*, 20:289–305, 1977.

[74] Krishnananda Chattopadhyay, Saveez Saffarian, Elliot L. Elson, and Carl Frieden. Measuring unfolding of proteins in the presence of denaturant using fluorescence correlation spectroscopy. *Biophysical journal*, 88(2):1413–1422, 2005.

[75] Jörg Enderlein, Ingo Gregor, Digambara Patra, and Jörg Fitter. Art and artefacts of fluorescence correlation spectroscopy. *Current Pharmaceutical Biotechnology*, 5:155–161, 2004.

[76] Jörg Enderlein, Ingo Gregor, Digambara Patra, Thomas Dertinger, and U. Benjamin Kaupp. Performance of fluorescence correlation spectroscopy for measuring diffusion and concentration. *ChemPhysChem*, 2005.

[77] Daryan Kempe. personal communication, 2015.

[78] U. Meseth, T. Wohland, R. Rigler, and H. Vogel. Resolution of fluorescence correlation measurements. *Biophysical journal*, 76(3):1619–1631, 1999.

[79] Julia Guy, Karine Caron, Stéphane Dufresne, Stephen W. Michnick, W. G. Skene, and Jeffrey W. Keillor. Convergent preparation and photophysical characterization of dimaleimide dansyl fluorogens: elucidation of the maleimide fluorescence quenching mechanism. *Journal of the American Chemical Society*, 129(39):11969–11977, 2007.

[80] Steven D. Quinn, Paul A. Dalgarno, Ryan T. Cameron, Gordon J. Hedley, Christian Hacker, John M. Lucocq, George S. Baillie, Ifor D. W. Samuel, and J. Carlos Penedo. Real-time probing of β-amyloid self-assembly and inhibition using fluorescence self-quenching between neighbouring dyes. *Molecular bioSystems*, 10(1):34–44, 2014.

[81] Eilon Sherman, Anna Itkin, Yosef Yehuda Kuttner, Elizabeth Rhoades, Dan Amir, Elisha Haas, and Gilad Haran. Using fluorescence correlation spectroscopy to study conformational changes in denatured proteins. *Biophysical journal*, 94(12):4819–4827, 2008.

[82] Dibyendu Kumar Sasmal, Tridib Mondal, Supratik Sen Mojumdar, Aparajita Choudhury, Rajat Banerjee, and Kankan Bhattacharyya. An fcs study of unfolding and refolding of cpm-labeled human serum albumin: role of ionic liquid. *The journal of physical chemistry. B*, 115(44):13075–13083, 2011.

[83] Suman Nag, Bidyut Sarkar, Arkarup Bandyopadhyay, Bankanidhi Sahoo, Sreenivasan, Varun K A, Mamata Kombrabail, Chandrakesan Muralidharan, and Sudipta Maiti. Nature of the amyloid-beta monomer and the monomer-oligomer equilibrium. *The Journal of biological chemistry*, 286(16):13827–13833, 2011.

[84] C. N. Pace. The stability of globular proteins. *CRC critical reviews in biochemistry*, 3(1):1–43, 1975.

[85] Yun-Ru Chen and Charles G. Glabe. Distinct early folding and aggregation properties of alzheimer amyloid-β peptides aβ40 and aβ42: Stable trimer or tetramer formation by aβ42. *Journal of Biological Chemistry*, 281(34):24414–24422, 2006.

[86] W. J. Becktel and J. A. Schellman. Protein stability curves. *Biopolymers*, 26(11):1859–1877, 1987.

[87] Sheh-Yi Sheu, Dah-Yen Yang, H. L. Selzle, and E. W. Schlag. Energetics of hydrogen bonds in peptides. *Proceedings of the National Academy of Sciences of the United States of America*, 100(22):12683–12687, 2003.

[88] Dennis J. Selkoe and Dale Schenk. Alzheimer's disease: molecular understanding predicts amyloid-based therapeutics. *Annual review of pharmacology and toxicology*, 43:545–584, 2003.

[89] Hugh A. Pearson and Chris Peers. Physiological roles for amyloid beta peptides. *The Journal of physiology*, 575(Pt 1):5–10, 2006.

A

Appendix

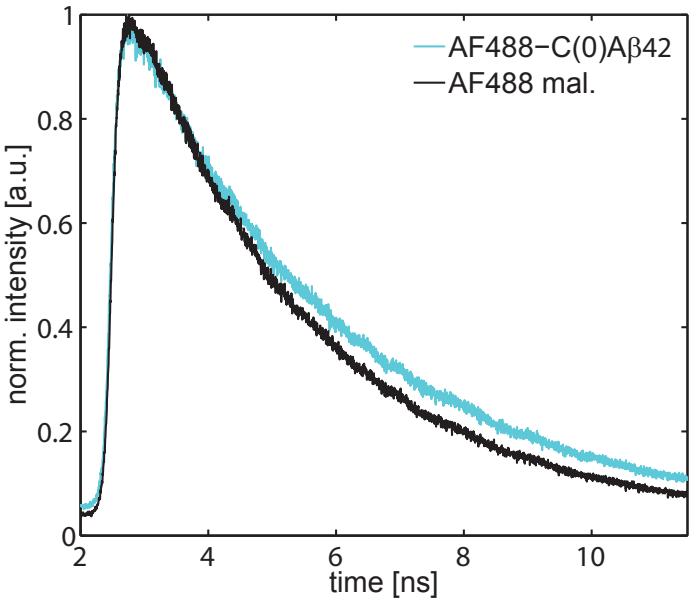

Figure A.1: Comparison of the fluorescence lifetime decays of AF488 maleimide and AF488-C(0)Aβ_{42} in 0.5 M GdnHCl. Free AF488 clearly shows a slightly lower fluorescence lifetime which can likely be attributed to self-quenching by the maleimido group [79].

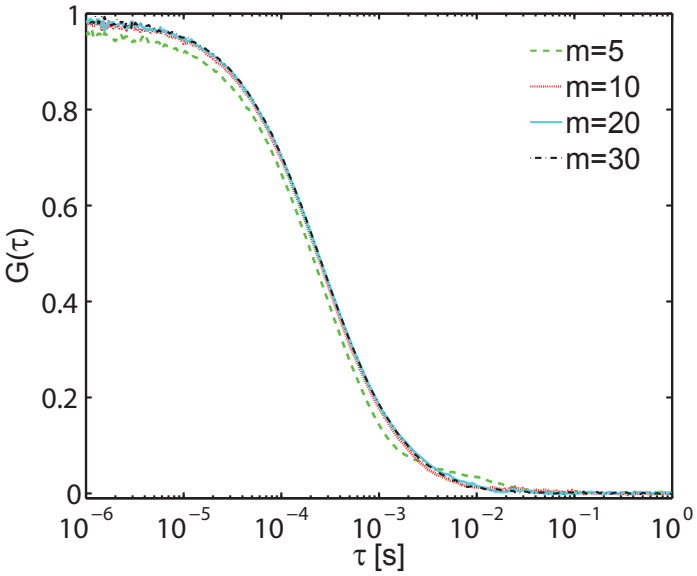

Figure A.2: Influence of the simulation box size (m-value) on the correlation curves obtained from Brownian dynamics simulation of FFS experiments. See section 5.1 for more details.

Selbstständigkeitserklärung

Ich versichere an Eides statt, dass die Dissertation von mir selbstständig und ohne unzulässige fremde Hilfe unter Beachtung der "Grundsätze zur Sicherung guter wissenschaftlicher Praxis an der Heinrich-Heine-Universität Düsseldorf" erstellt worden ist.